TECHNISCHE UNIVERSITÄT WIEN

INSTITUTE FOR MICROELECTRONICS

MASTER THESIS

Atomistic Description of 4H-SiC using Molecular Dynamics with Quantum Mechanical Accuracy

in partial fulfillment
Diplom-Ingenieur (Dipl.-Ing.)

supervised by
Associate Prof. Dr. techn. Lado Filipovic
Univ. Ass. Dipl. Ing. Dr. techn. Dominic Waldhör

at the
Technical University of Vienna
Faculty for Electrical Engineering and Information Technology
Institute for Microelectronics

submitted by
Robert Stella
Matrikelnummer: 12009691
Wenhartgasse 12/9
1210 Vienna, Austria

Vienna, March 2026

INSTITUTE FOR MICROELECTRONICS
Gußhausstraße 27-29, A-1040 Wien, Internet: https://www.iue.tuwien.ac.at/

Abstract

In modern power electronic devices, Silicon Carbide (SiC) is widely used due to its larger bandgap compared to silicon. Aluminium is typically employed as a p-type dopant because of its relatively small ionization energy. Due to the low thermal diffusion of Al in SiC, ion implantation followed by a high-temperature annealing is commonly used as a doping technique. However, even after annealing, various point defects and defect clusters remain in the material, which can prevent Al atoms from becoming electrically active. To gain a deeper understanding of the underlying activation mechanisms, atomistic simulations provide valuable insights.

Recent studies suggest that carbon interstitials and vacancies can form thermally stable complexes with Al, thereby preventing its electrical activation. Additionally, silicon interstitials may deactivate already active Al atoms through a kick-out mechanism. In contrast, carbon and di-carbon antisites can be displaced from the lattice by Al interstitials, potentially leading to dopant activation. The presence of larger defect clusters created during the implantation process further complicates the activation process, indicating that incomplete Al activation cannot be explained by a single defect mechanism alone.

Molecular Dynamics (MD) simulations provide a powerful approach to study the evolution of such defects and clusters during and after the implantation process. Since these MD simulations require a large number of energy and force evaluations, Density Functional Theory (DFT) would, in principle, provide a very accurate description of the system, but it is impractical due to its high computational cost. In this work, DFT calculations were first used to establish the relevant defect energetics and migration barriers in 4H-SiC, and different machine-learning interatomic potentials were then developed and compared with these DFT reference data to obtain both accurate and computationally efficient evaluations of the forces.

The results show that neutral Al interstitial diffusion in the basal plane proceeds through a metastable Al-Si split configuration and exhibits a migration barrier of 0.71 eV, which is substantially lower than the corresponding +3 barrier of 2.87 eV. Among the investigated machine-learning interatomic potentials, the GPU-accelerated DPA2 model provides the most consistent overall agreement with DFT for elastic, vibrational, amorphous, and defect properties, and it is the only tested model that also reproduces the low neutral-state Al migration barrier with good accuracy. Moment Tensor Potentials (MTPs), on the other hand, reproduce general structural and dynamical properties

reasonably well and remain attractive because of their high efficiency on CPU hardware, but they struggle to accurately describe point defects. These results establish DPA2 as the strongest candidate for future implantation-and-annealing simulations, while also showing that a broader sampling of amorphous and segregated structures will be necessary to further improve transferability.

Zusammenfassung

In modernen Leistungselektronikbauelementen findet Siliziumkarbid (SiC) aufgrund seiner größeren Bandlücke und der damit einhergehenden höheren Durchbruchsfeldstärke im Vergleich zu Silizium, einen breiten Anwendungsbereich. Aluminium wird typischerweise wegen seiner relativ niedrigen Ionisierungsenergie als p-Dotierstoff verwendet. Aufgrund der geringen thermischen Diffusion von Al in SiC werden die Fremdatome mittels Ionenimplantation eingebracht und anschließend wird der Kristall unter der Anwendung von hohen Temperaturen ausgeheilt. Selbst nach dem Ausheilprozess existieren verschiedene Punktdefekte und Defektcluster im Material, die die elektrischen Eigenschaften des Systems durch die nicht vollständig aktivierten Al Atome beeinflussen. Um die zugrundeliegenden Aktivierungsmechanismen besser zu verstehen, liefern atomistische Simulationen wertvolle Erkenntnisse.

Neuere Studien legen nahe, dass Kohlenstoff-Zwischengitteratome und -Leerstellen thermisch stabile Komplexe mit Al bilden und dadurch dessen elektrische Aktivierung verhindern können. Zusätzlich können Silizium-Zwischengitteratome bereits aktive Al-Atome durch einen Kick-out-Mechanismus deaktivieren. Im Gegensatz dazu können Kohlenstoff-Antisite-Defekte durch Al-Zwischengitteratome aus dem Siliziumgitter verdrängt werden, was potenziell zur Aktivierung des Dotierstoffes führt. Das Auftreten größerer Defektcluster während des Implantationsprozesses verkompliziert die Defektlandschaft zusätzlich.

Molekulardynamik-Simulationen (MD) bieten einen Ansatz zur Untersuchung der Entwicklung solcher Defekte und Cluster während und nach dem Implantationsprozess. Da solche MD-Simulationen eine große Anzahl von Energie- und Kraftberechnungen erfordern, würde die Dichtefunktionaltheorie (DFT) zwar grundsätzlich eine sehr genaue Beschreibung des Systems liefern, ist jedoch aufgrund ihres hohen Rechenaufwands nicht praktikabel. In dieser Arbeit werden verschiedene interatomare Potenziale auf Basis des maschinellen Lernens entwickelt und mit DFT-Referenzdaten verglichen, um sowohl eine hohe Genauigkeit als auch eine rechnerisch effiziente Bestimmung der Kräfte zu erreichen.

Die Ergebnisse zeigen, dass das Gaußsche Approximationspotential (GAP) sowohl realistisches dynamisches Verhalten als auch präzise Punktdefekteigenschaften reproduzieren kann, sofern die Hyperparameter sorgfältig angepasst wurden. Moment Tensor Potentiale (MTP) hingegen reproduzieren allgemeine Struktur- und Dynamikeigenschaften recht gut, haben aber Schwierigkeiten, Punktdefekte präzise zu beschreiben.

MTP-Modelle sind jedoch um Größenordnungen schneller als das GAP. Kürzlich entwickelte GPU-beschleunigte Multi-Task-Modelle zeigen eine gute Genauigkeit für alle untersuchten Eigenschaften bei gleichzeitig vergleichbarer Geschwindigkeit wie das MTP.

Foreword

First, I would like to thank my supervisor, Lado Filipovic, who encouraged me to take on the topic of atomistic simulations. His supportive mindset, especially when I struggled, and his ability to create a welcoming and at the same time helpful environment within his research group brought out the best in me, both academically and personally.

I would also like to thank my second supervisor, Dominic Waldhör, for his guidance and the many insightful discussions. Your knowledge in almost all topics impressed me a lot. These conversations helped me also to develop new ideas and kept me motivated throughout the course of my thesis.

I am especially grateful to Sabine Leroch, who took the time to introduce me to the field of molecular dynamics, despite my lack of prior experience. Without her patience and support, I would not have reached the level of understanding I have today.

I would also like to thank my colleagues in the office—Anna, Tobias, Martin, Angus, Yuki et al. for always being willing to listen and for the enjoyable time we shared during this work.

Last but not least, I want to thank my family for supporting me throughout my entire studies, not only during the time of writing this thesis.

Acknowledgement: The financial support by the Austrian Federal Ministry for Digital and Economic Affairs, the National Foundation for Research, Technology and Development, and the Christian Doppler Research Association are gratefully acknowledged

Parts of this thesis were improved using generative AI tools (e.g., ChatGPT) to refine language clarity and expression. All ideas and conclusions remain the original work of the author.

Eidesstattliche Erklärung

Ich erkläre an Eides statt, dass ich die vorliegende Diplomarbeit selbstständig und ohne fremde Hilfe verfasst, andere als die angegebenen Quellen und Hilfsmittel nicht benutzt bzw. die wörtlich oder sinngemäß entnommenen Stellen als solche kenntlich gemacht habe.

Wien, am 30. März 2026

Robert Stella

Robert Stella

Contents

List of Figures

List of Tables

List of Abbreviations

AIMD	Ab-Initio Molecular Dynamics
ASE	Atomic Simulation Environment
BFGS	Broyden-Fletcher-Goldfarb-Shanno
CI-NEB	Climbing Image Nudged Elastic Band
DFT	Density Functional Theory
DP	Deep Potential
FNV	Freysoldt-Neugebauer-van de Walle
GaN	Gallium Nitride
GAP	Gaussian Approximation Potential
GGA	Generalized Gradient Approximation
GW	Gao-Weber
HF	Hartree-Fock
HOMO	Highest Occupied Molecular Orbital
HSE	Heyd–Scuseria–Ernzerhof
IAP	Interatomic Potential
kMC	kinetic Monte Carlo
LAMMPS	Large-scale Atomic/Molecular Massively Parallel Simulator
LDA	Local Density Approximation
LUMO	Lowest Unoccupied Molecular Orbital
MD	Molecular Dynamics
ML-IAP	Machine Learning Interatomic Potential
MTP	Moment Tensor Potential
NEB	Nudged Elastic Band
NPT	Isothermal-Isobaric Ensemble
NVE	Microcanonical Ensemble
NVT	Canonical Ensemble
PBE	Perdew-Burke-Ernzerhof
PES	Potential Energy Surface
RDF	Radial Distribution Function
SCF	Self-Consistent Field
SiC	silicon carbide
SOAP	Smooth Overlap of Atomic Positions
WBG	Wide-bandgap
ZBL	Ziegler-Biersack-Littmark

CHAPTER 1

Introduction

The global annual energy consumption exceeds 170,000 TWh, of which more than 20% is electrical energy. An efficient electrical grid is a fundamental requirement for all power systems, regardless of the energy source. However, efficient distribution is particularly critical for integrating renewable energy sources, as these are often spatially distributed. In this context, efficient transmission and distribution of electrical energy are key enablers of the transition towards renewable electricity. Especially in high-voltage applications, such as the automotive sector, low-resistance switches are required to minimize power losses. It is well known that classical silicon-based metal oxide semiconductor field effect transistors (MOSFETs) are fundamentally limited in this regime because the on-resistance R_{on} scales quadratically with the breakdown voltage [1]. Device concepts such as double-diffused metal oxide semiconductor (DMOS), superjunctions, and insulated-gate bipolar transistors (IGBT) particularly mitigate this limitation, but the material properties of silicon itself remain a restriction, especially its comparatively small bandgap of 1.12 eV and the resulting limited breakdown field. Wide-bandgaps (WBGs) semiconductors such as SiC and Gallium Nitride (GaN) therefore offer a more attractive platform for efficient power electronics.

This chapter first compares SiC and GaN as candidate materials for power applications. It then focuses on p-type doping in 4H-SiC, the challenge of incomplete Al activation, and the role of atomistic simulations in understanding the relevant defect processes. A broader overview of power-device architectures and their typical voltage classes is given elsewhere.[2].

1.1 Wide-Bandgap Semiconductors

Figure 1.1 compares key bulk material properties relevant for power applications. SiC combines a high breakdown field with high thermal conductivity, which makes it attractive for high-power devices that must dissipate large amounts of heat. GaN, on the other hand, is particularly promising for high-frequency and high-voltage applications because heterostructures such as AlGaN/GaN can host a two-dimensional electron gas (2DEG) with electron mobilities far exceeding those of bulk GaN [2]. Overall, both

materials are leading WBG semiconductors for low-loss power conversion. In practice, however, the availability of high-quality bulk substrates currently makes SiC the more mature solution for many commercial power-electronics applications.

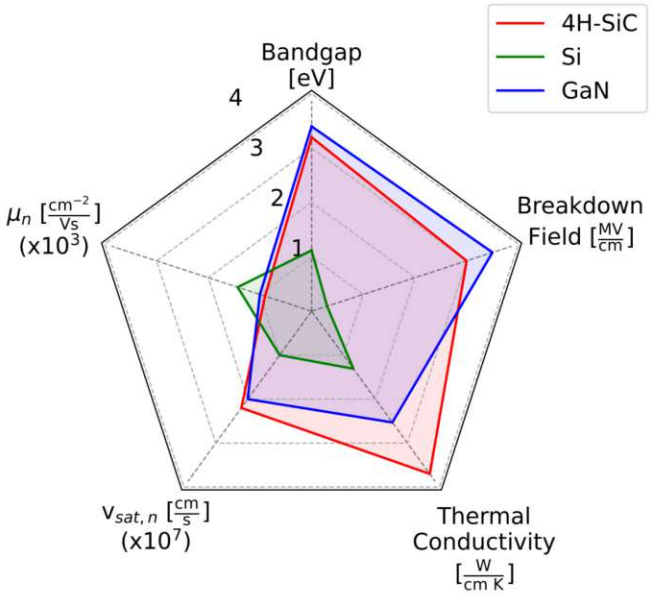

Figure 1.1: Summary of relevant semiconductor material properties for power applications. Data taken from [3], [4], [5].

1.1.1 4H-SiC

SiC exists in several polytypes, meaning that the various crystal structures have an identical stoichiometric while differing in the stacking sequence of hexagonal bilayers. These bilayers are commonly denoted A, B, and C and are stacked along the [0001] direction, the crystallographic c-axis. The Miller-Bravais indices for the three in-plane hexagonal axes a_1, a_2, and a_3 are $[\bar{1}\bar{1}20]$, $[2\bar{1}\bar{1}0]$, and $[\bar{1}2\bar{1}0]$, respectively. Among the technologically relevant polytypes, 4H-SiC, with a stacking sequence of ABCB, is particularly important for high-voltage power devices because of its wide bandgap of 3.26 eV and its mature device technology. This thesis therefore focuses on 4H-SiC. The three bilayer positions are illustrated in Figure 1.2, while Figure 1.3 compares the stacking sequences of selected SiC polytypes.

For p-type doping, aluminum (Al) is generally preferred over boron (B) because of its lower ionization energy, as schematically illustrated in Figure 1.4. An electrically active Al occupies a silicon lattice site in either the cubic (c) or hexagonal (h) plane. Because the thermal diffusivity of Al in SiC is very low, p-type doping is typically achieved by ion implantation followed by high-temperature annealing. Ion implantation is, however a highly non-equilibrium process that introduces a broad spectrum of damage, ranging from isolated point defects to extended defect clusters and, at high damage levels, amorphous regions. Annealing partially restores the crystal, but residual defects can

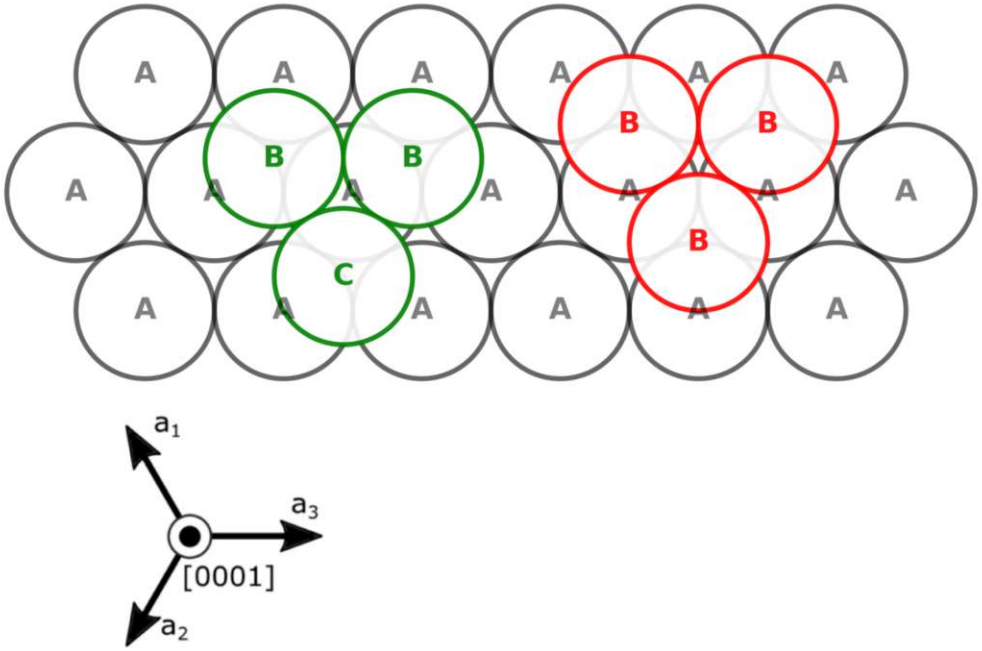

Figure 1.2: Top view of the three bilayer positions A, B, and C.

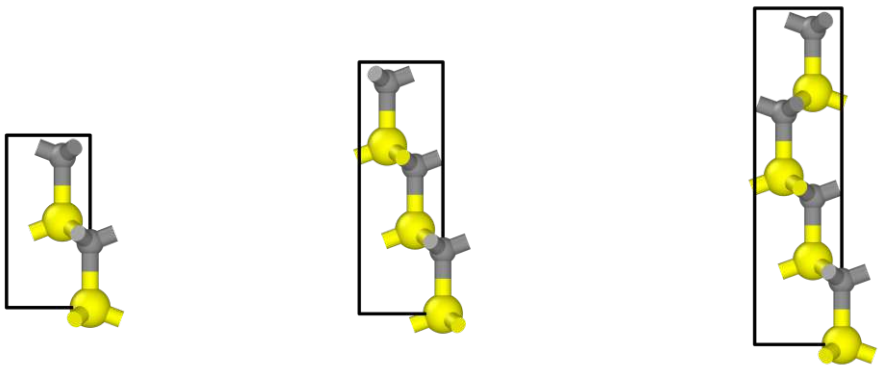

(a) (b) (c)

Figure 1.3: (a) 2H-SiC with a stacking sequence of AB, (b) 3C-SiC with a stacking sequence of ABC, and (c) 4H-SiC with a stacking sequence of ABCB.

still trap, compensate, or deactivate dopants. As a result, the fraction of electrically active Al frequently remains below the implanted dose.

From a microscopic point of view, several defect reactions can contribute to this incomplete activation. DFT studies suggest that Al can form thermally stable complexes with carbon interstitials ($Al_I C_I$) and carbon vacancies ($Al_{Si} V_C$), thereby preventing the dopants from becoming electrically active [6]. After Al implantation with 150 keV and subsequent annealing at 2000 K, Kumar et al. reported persistent defect signatures associated with carbon-related damage, indicating that implantation-induced defects remain relevant even after high-temperature recovery [7].

The activation problem is, however, not limited to the formation of static trapping complexes. Later in the thesis it is shown that silicon interstitials can also deactivate already substitutional Al through kick-out-like processes, whereas antisite-related reactions may, under suitable conditions, contribute to activation instead. In other words, the final electrically active dopant fraction is determined by a competition between multiple defect reactions rather than by a single dominant trapping mechanism.

An additional complication is the role of charge state. Many Al-related defects are most stable in positive charge states under p-type conditions, but neutral charge states become relevant close to the conduction band and are the states typically addressed in standard classical Molecular Dynamics (MD) simulations. As a result, quantitatively meaningful multiscale modeling requires a consistent comparison between charge-dependent Density Functional Theory (DFT) results and neutral-state diffusion mechanisms that can later be represented within atomistic force-field-based simulations.

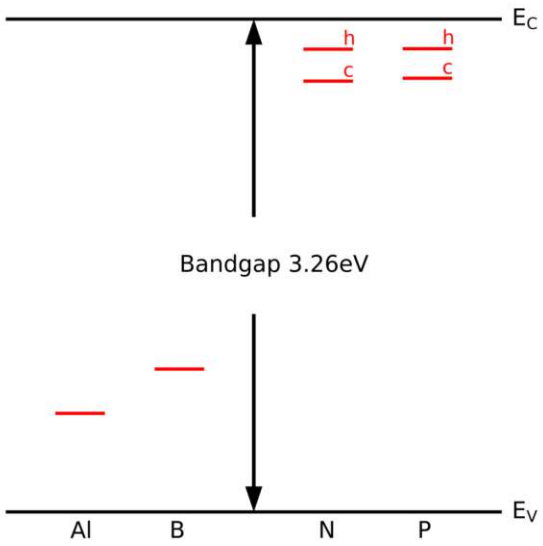

Figure 1.4: Ionization levels for various dopants in 4H-SiC. Here, (h) and (c) denote hexagonal and cubic lattice sites, respectively. Data taken from Ref. [3].

1.2 Multiscale Modeling

The exact formation mechanisms of implantation-induced defects and the conditions under which they form remain only partially understood. Atomistic simulations provide

a route to resolve both the defect structures and their evolution in time. Common approaches in atomistic modeling are DFT, MD, and kinetic Monte Carlo (kMC). Each operates on a different length and time scale and therefore offers a different compromise between physical accuracy and computational cost. DFT, by solving the Kohn-Sham equations, treats the system quantum mechanically and can accurately describe the electronic structure of systems containing up to a few hundred atoms. For bigger systems, the next step in the ladder is MD, which treats the atoms classically and requires an Interatomic Potential (IAP) to describe the atomic interactions. Therefore, bigger systems of up to 10^6 atoms can be dynamically simulated over time spans of several nanoseconds, depending on the type of IAP used [8]. At the largest scale, kMC replaces explicit atomic trajectories with transition probabilities between descreet states, making it possible to simulate experimenta time scales and device-relevant dimensions.

No single method is sufficient on its own: DFT is accurate but too expensive for implantation and long-time annealing, whereas MD and kMC require physically meaningful input models and rate parameters. Methods that bridge these scales are therefore of particular interest and are commonly referred to as multiscale approaches. Figure 1.5 summarizes the relevant scales considered in this work.

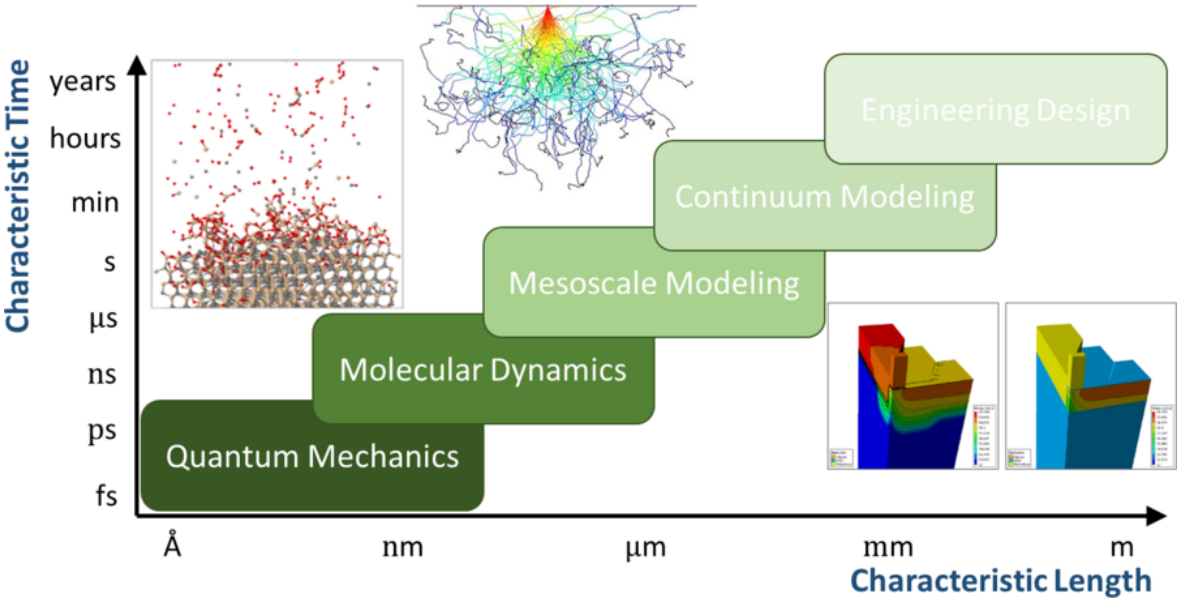

Figure 1.5: Time and length scales for different atomistic simulation approaches.

For SiC, classical MD studies often rely on the Brenner-type potential parameterized by Gao-Weber (GW), typically combined with a short-range Ziegler-Biersack-Littmark (ZBL) correction [9]. This potential has been widely used to study point defects and amorphous structures. Shortly after its introduction, the dominant migration mechanisms in 3C-SiC were investigated with this potential [10]. For silicon interstitials, the main diffusion path predicted by GW was found to be a jump between two tetrahedral positions Si_{TC} via a kick-out process involving a second Si atom. For carbon, two different mechanisms were observed, both starting and ending with a C-C dumbbell configuration.

Using DFT, it was found that carbon interstitials most likely diffuse along the same path predicted by GW calculations, independent of charge state. In contrast, the migration of silicon interstitials is more charge-dependent [11]. Neutral silicon

interstitials exist in the n-type region, whereas in the p-type region, they typically adopt a positive charge state. Under n-type and intrinsic conditions, the most stable configuration is $Si_{sp,h\langle 110\rangle}$. Consequently, the primary diffusion path in the hexagonal basal plane involves jumps from $Si_{sp,h\langle 110\rangle}$ to $Si_{sp,h\langle 110\rangle}$ with a migration barrier of 1.54 eV [12]. In 3C-SiC, a lower barrier is reported when the $Si_{sp,c\langle 110\rangle}$ interstitial diffuses via the meta-stable Si_{TC} configuration, which resembles the GW pathway but yields a significantly lower DFT barrier of about 0.7 eV [13]. Since silicon interstitials in cubic layers have a formation energy more than 1 eV higher than those in hexagonal layers, basal diffusion in 4H-SiC is expected to proceed predominantly through split hopping in the hexagonal layers [12], [14].

Under p-type conditions, most silicon interstitials are positively charged, and tetrahedral configurations such as Si_{TC} become energetically favorable. Diffusion then proceeds by direct cage jumps or kick-out processes involving Si-Si dumbbells. Immediately after implantation, however, the material is typically closer to intrinsic conditions because the implanted Al atoms are not yet fully activated and the defect density is very high. Consequently, the diffusion behavior relevant directly after implantation can differ substantially from that expected in the fully annealed p-type regime. This mismatch is one of the reasons why empirical force fields based on a simplified bonding picture struggle to capture the relevant defect physics over the full process window.

To model Al-SiC interactions, Dandekar et al. proposed a Morse-type extension that is still frequently used [15]. Owing to its pairwise formulation, however, it cannot adequately describe the many-body bonding changes associated with Al activation and defect reactions. This creates a gap between the accuracy of DFT and the length and time scales accessible to MD.

This thesis addresses that gap by developing and evaluating ML-IAPs for the ternary Al-Si-C system. These models replace fixed empirical energy expressions with flexible representations learned from first-principles reference data. Previous attempts to develop ML-IAPs for SiC have been reported; however, to the best of our knowledge, no dedicated potential has yet been trained for the ternary Al-Si-C system relevant for Al activation in SiC [16], [17], [18], [19]. The objectives of this work are therefore twofold: first, to investigate Al-related defect energetics and migration mechanisms with DFT; and second, to train and benchmark ML-IAPs against DFT reference data for elastic properties, phonon spectra, amorphous structures, relative defect formation energies, and selected migration barriers. In this multiscale picture, DFT provides the atomistic reference for defect energetics and reaction pathways, ML-IAP-based MD extends the accessible length and time scales toward implantation damage and annealing, and the extracted energies and reaction rates can ultimately serve as input for kMC simulations. In this way, the thesis contributes both new atomistic insight and a practical modeling framework for studying incomplete Al activation in 4H-SiC.

The remainder of the thesis is organized as follows. Chapter 2 introduces the theoretical methods used throughout this work. Chapter 3 presents the DFT calculations for Al-related defects as well as the training and validation of the developed ML-IAPs. The appendices collect supplementary details on tensor notation, additional DFT barriers, training procedures, and extended benchmark results.

CHAPTER 2

Theory

In recent years, MD simulations have been conducted to investigate the activation process of implanted aluminum in 4H-SiC under different implantation and annealing conditions [20], [21]. These studies highlighted the previously noted discrepancy between activation energies predicted by MD and DFT, especially for Al-related defects. In this chapter, the computational methods used to study defects and their dynamics are discussed.

2.1 Quantum Mechanical Methods

DFT is a widely used approach in the computational material science community, since it allows us to study systems quantum mechanically and provides access to their electronic structure. The theoretical foundation of DFT was established by Hohenberg and Kohn, whose theorems state that all ground-state properties of a many-electron system are uniquely determined by its electron density. Subsequently, the theory was extended by Kohn and Sham, who formulated the Kohn-Sham equations, an effective single-particle formulation of the many-body Schrödinger equation that can be solved numerically [22], [23].

2.1.1 Many-body Schrödinger Equation

For a system of N electrons with coordinates $\boldsymbol{r}_1,\ldots,\boldsymbol{r}_N$ and M nuclei with coordinates $\boldsymbol{R}_1,\ldots,\boldsymbol{R}_M$, the system is fully described by the time-independent many-body Schrödinger equation:

$$\Bigg[\underbrace{-\sum_i \frac{\hbar^2}{2m_\mathrm{e}}\nabla_i^2}_{\text{kinetic energy } e^-} \underbrace{-\sum_I \frac{\hbar^2}{2M_I}\nabla_I^2}_{\text{kinetic energy nuclei}} \underbrace{+\frac{1}{2}\sum_{i\neq j}\frac{e^2}{4\pi\varepsilon_0}\frac{1}{|\boldsymbol{r}_i-\boldsymbol{r}_j|}}_{\text{potential energy } e^-e^-} + \underbrace{\frac{1}{2}\sum_{I\neq J}\frac{e^2}{4\pi\varepsilon_0}\frac{Z_I Z_J}{|\boldsymbol{R}_I-\boldsymbol{R}_J|}}_{\text{potential energy nuclei nuclei}} \underbrace{-\sum_{i,J}\frac{e^2}{4\pi\varepsilon_0}\frac{Z_J}{|\boldsymbol{r}_i-\boldsymbol{R}_J|}}_{\text{potential energy } e^- \text{ nuclei}} \Bigg] \Psi = E_\mathrm{tot}\Psi. \quad (2.1)$$

where the charges of the nuclei are represented by their atomic number Z_i, the nuclei masses are represented by M_i, and the electron masses by m_e. The solution of the many-body Schrödinger equation is the wavefunction $\Psi\left(\boldsymbol{r}_1,\ldots,\boldsymbol{r}_N,\boldsymbol{R}_1,\ldots,\boldsymbol{R}_M\right)$, where the square of its absolute value, $|\Psi|^2$, represents the probability density for finding the particles at the specified coordinates. Evidently, the problem scales dramatically with the number of nuclei and electrons, since each particle introduces three additional degrees of freedom, making it impossible to solve the full Schrödinger equation for large systems. In the following, some approximations are presented that greatly simplify the problem.

2.1.2 Born-Oppenheimer Approximation

Since electrons have a much lower mass than nuclei ($m_e \ll M_I$), they move significantly faster and can respond almost instantaneously to the motion of the nuclei. From the perspective of the electrons, the nuclei appear effectively fixed, meaning that the kinetic-energy term from the nuclei can be neglected. Furthermore, the nucleus–nucleus interactions primarily contribute an energy offset, which can be separated out. Under these assumptions, the many-body Schrödinger equation for the electronic subsystem can be written as:

$$\Bigg[\underbrace{-\sum_i \frac{\hbar^2}{2m_\mathrm{e}}\nabla_i^2}_{\text{kinetic energy } e^-} + \underbrace{\frac{1}{2}\sum_{i\neq j}\frac{e^2}{4\pi\varepsilon_0}\frac{1}{|\boldsymbol{r}_i-\boldsymbol{r}_j|}}_{\text{potential energy } e^-e^-} \underbrace{-\sum_{i,J}\frac{e^2}{4\pi\varepsilon_0}\frac{Z_J}{|\boldsymbol{r}_i-\boldsymbol{R}_J|}}_{\text{potential energy } e^- \text{ nuclei}} \Bigg] \Psi = E_\mathrm{tot,elec}\Psi. \quad (2.2)$$

In the literature, this assumption is known as the Born-Oppenheimer approximation. With the nuclei treated as effectively clamped, the wavefunction becomes a function of the electron coordinates only, $E_\mathrm{tot,elec}$, $\Psi\left(\boldsymbol{r}_1,\ldots,\boldsymbol{r}_N\right)$, while the nuclei coordinates enter Equation (2.2) only as parameters and define the total electronic energy $E_\mathrm{tot,elec}$.

2.1.2.1 Hartree-Fock Equations

The first simplification of the electronic Schrödinger equation is to express the total wavefunction $\Psi\left(\boldsymbol{r}_1,\ldots,\boldsymbol{r}_N\right)$ as a product of single-particle wavefunctions $\phi_i(\boldsymbol{r}_i)$:

$$\Psi\left(\boldsymbol{r}_1,\ldots,\boldsymbol{r}_N\right) = \phi_1(\boldsymbol{r}_1)\cdot\phi_2(\boldsymbol{r}_2)\cdot\ldots\cdot\phi_N(\boldsymbol{r}_N) \quad (2.3)$$

$$n(\boldsymbol{r}) = \sum_i |\phi_i|^2 \quad (2.4)$$

which is known as the Hartree product [24]. This formulation implies that the electrons are treated as independent particles, each contributing to the total electron density n through their respective $|\phi_i(\boldsymbol{r}_i)|^2$ terms, as seen in Equation (2.4). This heuristic approach neglects the Pauli exclusion principle and therefore leads to an incorrect description of the electron–electron interaction, as the electrons are not treated as Fermions. When these effects are properly accounted for, one arrives at the Hartree-Fock (HF) equation:

$$\left[-\frac{\hbar^2}{2m_e}\nabla_i^2 - \sum_I \frac{e^2 Z_I}{|\boldsymbol{r}_i - \boldsymbol{R}_I|} + V_{\mathrm{H}}\right]\phi_i + \overbrace{\sum_j \phi_j(\boldsymbol{r}) \int \frac{\phi_i(\boldsymbol{r}')\phi_j^*(\boldsymbol{r}')}{|\boldsymbol{r} - \boldsymbol{r}'|} d\boldsymbol{r}'}^{\text{Exchange energy } E_X} = \varepsilon_i \phi_i(\boldsymbol{r}) \tag{2.5}$$

where $V_{\mathrm{H}}(\boldsymbol{r})$ is the Hartree potential given by:

$$V_{\mathrm{H}}(\boldsymbol{r}) = \frac{e^2}{4\pi\varepsilon_0} \int \sum_i \frac{|\phi_i(\boldsymbol{r}')|^2}{|\boldsymbol{r} - \boldsymbol{r}'|} d\boldsymbol{r}'. \tag{2.6}$$

Rather than solving the Schrödinger equation for the full many-body wavefunction Ψ, the HF equations are a set of single-particle Schrödinger equations in which the particles move in an effective potential produced by all other particles. An important contribution to this effective potential is the exchange energy E_X, which introduces a non-local term. In the HF method, this exchange contribution is exact by construction, while electron correlation is still neglected.

2.1.2.2 Kohn-Sham Equations

The Hartree-Fock theory is not exact because electron-correlation effects are missing. Although these can be included by post-HF methods, such calculations are extremely expensive. The Hohenberg-Kohn theorem states that for a system of interacting electrons in an external potential, all ground-state properties are uniquely determined by the electron density n($\boldsymbol{r}$)[22]. In Kohn-Sham theory, the exchange potential is approximated by a (semi) local form and complemented by a correlation term resulting in the Kohn-Sham (KS) equations [23]:

$$\left[-\frac{\hbar^2}{2m_e}\nabla_i^2 - \sum_I \frac{e^2 Z_I}{|\boldsymbol{r}_i - \boldsymbol{R}_I|} + V_{\mathrm{H}}(\boldsymbol{r}) + V_{\mathrm{XC}}(\boldsymbol{r}, n(\boldsymbol{r}))\right]\phi_i = \varepsilon_i \phi_i(\boldsymbol{r}) \tag{2.7}$$

$$V_{\mathrm{XC}}(\boldsymbol{r}, n(\boldsymbol{r})) = V_{\mathrm{X}}(\boldsymbol{r}, n(\boldsymbol{r})) + V_{\mathrm{C}}(\boldsymbol{r}, n(\boldsymbol{r})). \tag{2.8}$$

As for the HF equations, the KS equations are a set of single particle Schrödinger equations that differ only in how the effective potential is constructed. Since the exact analytical forms of the exchange and correlation terms are unknown, various approximations have been developed to map the electron density to the corresponding energy and potential. These approximations are often categorized according to their complexity:

- **Local Density Approximation (LDA):** Uses only the local electron density $n(\boldsymbol{r})$.

- **Generalized Gradient Approximation (GGA):** Accounts for the gradient of the electron density $\nabla n(\boldsymbol{r})$.
- **Hybrid functional:** Incorporates a fraction of the exact exchange potential from HF theory.

A well-known GGA functional was derived by Perdew-Burke-Ernzerhof (PBE) [25] and a widely used hybrid functionals is Heyd–Scuseria–Ernzerhof (HSE) [26].

2.1.3 Density Functional Theory

Since the Kohn-Sham equations cannot, in general, be solved in closed form, they are treated iteratively through a Self-Consistent Field (SCF) cycle. First, an initial electron density $n(\boldsymbol{r})$ is specified. With this density, an effective potential is constructed, where V_{ext} is the external potential arising from the charged nuclei and V_{xc} is defined by the chosen functional. This effective potential is then used to solve for the single-particle wavefunctions $\phi_i(\boldsymbol{r})$. From these, a new electron density is calculated. If the difference between the old and new densities is smaller than a specified convergence threshold ε, the SCF cycle is considered converged. This workflow is illustrated in Figure 2.1.

Throughout this work, DFT simulations were performed using the CP2K package [27] within the Gaussian plane-wave (GPW) formalism [28] and Goedecker-Teter-Hutter (GTH) pseudopotentials [29]. Double-ζ Gaussian basis sets were employed together with a plane-wave energy cutoff of 800 Ry. Exchange-correlation effects were treated using the semilocal PBE functional [25]. For generating training data for the ML-IAP, the orbital-transormation (OT) method with Γ point sampling was applied for larger structures, while Broyden mixing with k-point sampling was used for smaller structures such as strained unit cells. For the defect calculations presented in section 3.1, an orthogonal supercell containing 480 atoms with dimensions $15.44\,\text{Å} \times 16.03\,\text{Å} \times 20.22\,\text{Å}$was prepared. Due to the relatively large system size only the Γ point was sampled for those defect structures. Structural optimizations were performed using the Broyden-Fletcher-Goldfarb-Shanno (BFGS) algorithm, and a force convergence criterion of $20\,\text{meV}/\text{Å}$ was applied for those calculations. For SCF convergence, a threshold ε of 10^{-6} was applied throughout this thesis.

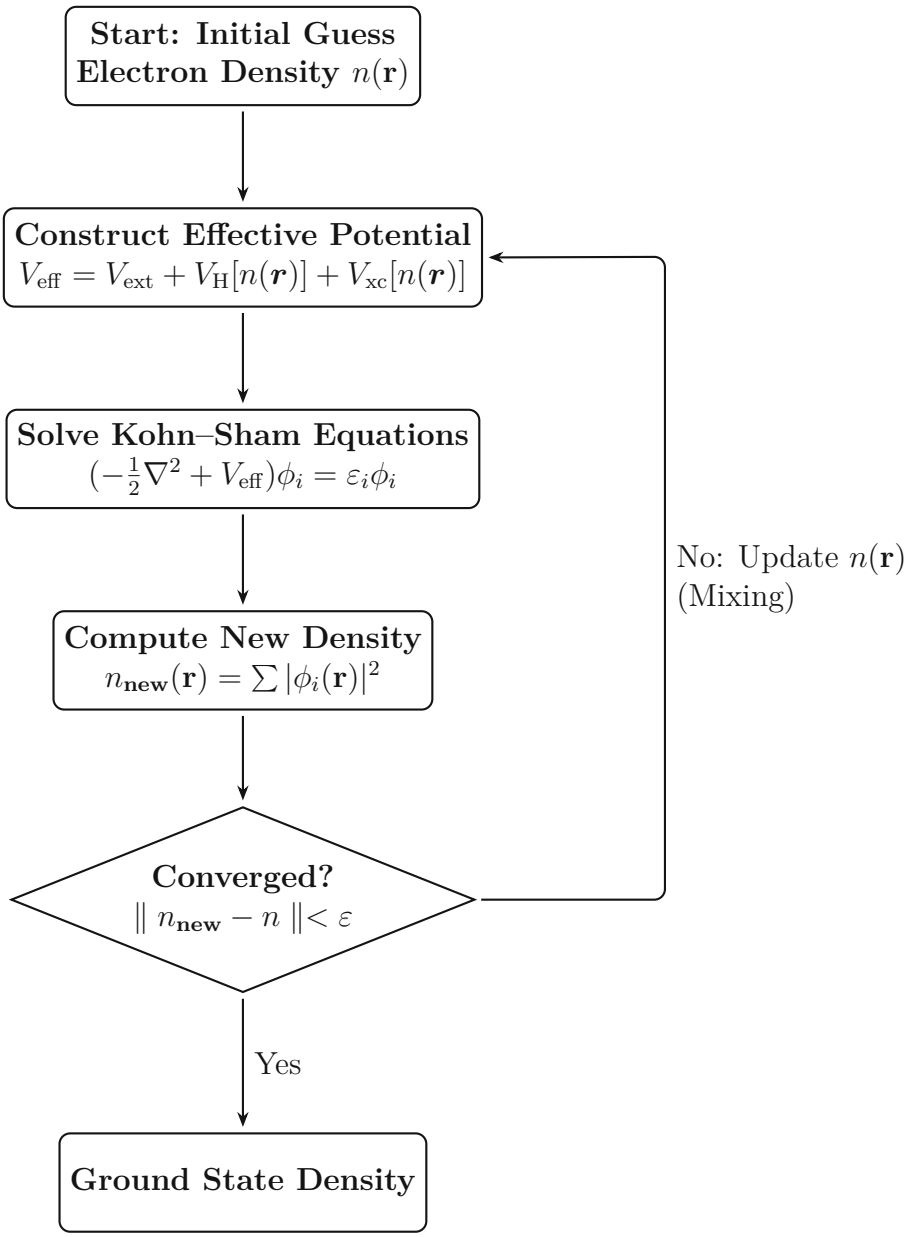

Figure 2.1: Self-consistent field cycles used in standard DFT workflows.

2.2 Molecular Dynamics

Molecular dynamics (MD) investigates the motion of nuclei in space and time on a Potential Energy Surface (PES) $U(\boldsymbol{R}_1, \ldots, \boldsymbol{R}_N)$, which arises from the separation of electronic and nuclei dynamics within the Born-Oppenheimer approximation. The dynamics are governed by Newton's equations of motion:

$$\boldsymbol{F}_i\left(\boldsymbol{R}_1,\ldots,\boldsymbol{R}_N\right) = -\nabla_i U\left(\boldsymbol{R}_1,\ldots,\boldsymbol{R}_N\right) \tag{2.9}$$

$$m_i\boldsymbol{a}_i = \boldsymbol{F}_i\left(\boldsymbol{R}_1,\ldots,\boldsymbol{R}_N\right) \tag{2.10}$$

$$\frac{\partial^2\boldsymbol{R}_i}{\partial t^2} = -\frac{1}{m_i}\nabla_i U\left(\boldsymbol{R}_1,\ldots,\boldsymbol{R}_N\right) \tag{2.11}$$

$$\frac{\partial\boldsymbol{v}_i}{\partial t} = -\frac{1}{m_i}\nabla_i U\left(\boldsymbol{R}_1,\ldots,\boldsymbol{R}_N\right) \tag{2.12}$$

$$\tag{2.13}$$

where $\boldsymbol{R}_i$ and $\boldsymbol{v}_i$ are the coordinates and velocities of atom i. Classically, the PES is represented by an IAP. Examples of IAPs are ReaxFF [30], Tersoff [31], the Modified Embedded Atom Method (MEAM) [32], and Stillinger-Weber [33]. It is important to note that each potential has its own strengths. ReaxFF, for example, is able to describe chemical reactions on surfaces but struggles with mechanical properties.

The evolution in time of the positions and velocities can be calculated using the Verlet algorithm [34]:

$$\boldsymbol{v}_i(t+\frac{1}{2}\Delta t) = \boldsymbol{v}_i(t) + \frac{\boldsymbol{F}_i(t)}{2m_i}\Delta t \tag{2.14}$$

$$\boldsymbol{R}_i(t+\Delta t) = \boldsymbol{R}_i(t) + \boldsymbol{v}_i(t+\frac{1}{2}\Delta t)\Delta t \tag{2.15}$$

$$\boldsymbol{v}_i(t+\Delta t) = \boldsymbol{v}_i(t+\frac{1}{2}\Delta t) + \frac{\boldsymbol{F}_i(t+\Delta t)}{2m_i}\Delta t. \tag{2.16}$$

The Verlet algorithm is a numerical method for integrating Newton's equations of motion in time. Due to its stability and low computational cost, it is often preferred over the forward Euler method.

2.2.1 Thermostats and Barostats

Since results obtained from MD simulations are often compared to experimental data, ambient conditions such as the temperature and pressure of the system must be properly mimicked. If Newton's equations are solved without any additional modifications, there is no guarantee that the time-averaged temperature matches the target temperature. For a conservative force field, the total energy of the system remains constant, corresponding to a Microcanonical Ensemble (NVE), where the number of particles N, the volume V, and the total energy E are fixed.

To maintain a fixed average temperature, the equations of motion are extended, enabling sampling of the Canonical Ensemble (NVT) ensemble. Furthermore, if the pressure should be kept constant, a barostat is employed. Typically, when pressure is controlled, the temperature is regulated as well, leading to the Isothermal-Isobaric Ensemble (NPT) ensemble, which represents a very general case for experimental comparison.

It is important to note that different mathematical formulations of these ensembles can lead to different dynamical behaviors, even when attempting to reproduce the same macroscopic properties. Accordingly, a wide range of thermostats exists, including

the Nosé–Hoover, Berendsen, Langevin, and Andersen thermostats. For instance, the Berendsen thermostat suppresses thermal fluctuations but does not produce correct NVT sampling, so the choice of thermostat must be made carefully depending on the simulation goals. The same considerations apply to barostats. In the following, Nosé–Hoover thermostats and barostats are presented, which allow correct NVT and NPT sampling and are therefore state-of-the-art in production runs. A detailed description of thermostats and barostats can be found elsewhere [35].

2.2.1.1 Nosé–Hoover Thermostat

To maintain the target temperature, the system of ordinary differential equations (ODEs) is extended as:

$$\boldsymbol{a}_i = \frac{\partial^2 \boldsymbol{R}_i}{\partial^2 t} = \frac{\boldsymbol{F}_i}{m_i} - \frac{p_\xi}{Q}\frac{\partial \boldsymbol{R}_i}{\partial t} = \frac{\boldsymbol{F}_i}{m_i} - \frac{p_\xi}{Q}\boldsymbol{v}_i \tag{2.17}$$

$$\frac{\mathrm{d}p_\xi}{\mathrm{d}t} = T - T_0 \tag{2.18}$$

for the Nosé–Hoover thermostat [36], [37]. The additional term depends on the difference between the current temperature T and the target T_0, as well as on the constant Q, commonly referred to as the mass of the thermal reservoir.

If the temperature T exceeds the target T_0, p_ξ becomes positive, resulting in a reduction of the current velocities. For systems far from equilibrium, this type of thermostat may be less suitable, as it can introduce oscillations. In such cases, alternative thermostats, such as the Berendsen thermostat, may provide better stability [38].

The application of thermostats requires knowledge of the current temperature T. For a system with periodic boundary conditions containing N atoms, the temperature is calculated according to Equation (2.19). The center-of-mass velocity $\boldsymbol{v}_{\mathrm{CM}}$ is removed since the temperature is independent of the chosen inertial frame and therefore requires relative velocities.

$$T = \frac{\sum_i^N m_i(\boldsymbol{v}_i - \boldsymbol{v}_{\mathrm{CM}})^2}{3(N-1)k_{\mathrm{B}}} \tag{2.19}$$

$$\boldsymbol{v}_{\mathrm{CM}} = \frac{\sum_i^N m_i \boldsymbol{v}_i}{\sum_i^N m_i} \tag{2.20}$$

2.2.1.2 Nosé–Hoover NPT

In the NPT ensemble, temperature and pressure are coupled, such that changes in one quantity affect the other. For isotropic pressure, the system dynamics are described by the equations [39]:

$$\boldsymbol{v}_i = \boldsymbol{v}_i + \frac{p_\epsilon}{W}\boldsymbol{R}_i \tag{2.21}$$

$$\boldsymbol{a}_i = \frac{\boldsymbol{F}_i}{m_i} - \frac{p_\epsilon}{W}\boldsymbol{v}_i - \frac{p_\xi}{Q}\boldsymbol{v}_i \tag{2.22}$$

$$\dot{p}_\epsilon = 3V(P_{\text{int}} - P_{\text{ext}}) - \frac{p_\epsilon p_\xi}{Q} \tag{2.23}$$

$$\dot{p}_\xi = \sum_i^N m_i(\boldsymbol{v}_i - \boldsymbol{v}_{\text{CM}})^2 + \frac{p_\epsilon^2}{W} - N_{\text{f}} k_{\text{B}} T_0. \tag{2.24}$$

Under periodic boundary conditions, the total number of internal degrees of freedom becomes $N_{\text{f}} = 3N - 2$, since the non-fixed simulation cell introduces an additional degree of freedom.

In Equation (2.23) and Equation (2.24), the barostat momentum p_ϵ and the thermostat momentum p_ξ are coupled, meaning that a change in one directly influences the other. The scaling of atomic coordinates is given by the last term of Equation (2.21), where a positive barostat momentum results in an expansion of the simulation cell. In contrast to the NVT ensemble, the velocity scaling does not depend solely on the thermostat momentum, but instead on both momenta as described in Equation (2.22). Consequently, an expansion of the simulation cell implicitly reduces the overall atomic velocities. One can think of an ideal gas, where an expansion also leads to a decrease in the temperature.

For the isotropic case, the pressure is calculated according to:

$$P = \frac{N k_{\text{B}} T}{V} + \frac{1}{3V}\sum_i^N \boldsymbol{R}_i \boldsymbol{F}_i. \tag{2.25}$$

The first term accounts for the kinetic-energy contribution, calculated using Equation (2.19), while the second term represents the virial contribution [39]. In general, these equations can also be extended to more general pressure tensors, which are discussed elsewhere [40].

In this work, MD simulations were carried out within the Large-scale Atomic/Molecular Massively Parallel Simulator (LAMMPS) framework, as it provides interfaces for most IAP types [41].

2.3 Machine Learning Interatomic Potentials

In recent years, ML-IAPs have emerged as a powerful approach for representing PES and are increasingly replacing classical force fields. Unlike classical potentials, they do not rely on a fixed functional form but instead learn the interactions from large amounts of DFT reference data. This makes the development of a general-purpose potential challenging because of the amount of required training data. Consequently, ML-IAPs are typically designed for specific applications.

In the following, the general concepts of ML-IAPs are first introduced. Subsequently, three representative approaches are presented, namely the Moment Tensor Potential (MTP) [42], Gaussian Approximation Potential (GAP) [43], and Deep Potential (DP) [44], [45], [46]. Another well-known ML-IAP is MACE, which is not covered in greater detail [47].

2.3.1 ML-IAP Theory

For a system consisting of N atoms with coordinates $\boldsymbol{R} = \{\boldsymbol{R}_1, \ldots, \boldsymbol{R}_N\}$, the total energy E of the system is a global quantity, whereas the local energy E_i depends only on the neighboring atoms within a cutoff radius r_c. A common assumption in many ML-IAP frameworks is that the total energy E can be expressed as a sum of the local atomic energies, as described in Equation (2.26).

$$E = \sum_{i=1}^{N} E_i \tag{2.26}$$

Since the Cartesian coordinates of neighboring atoms form a high-dimensional space in which fundamental properties such as translational and rotational invariance are not encoded explicitly, a more suitable representation of the atomic environment is required. Therefore, the local environment of atom i is mapped onto a descriptor $\boldsymbol{D}_i$, which is invariant to rotations, translations, and permutations, as these transformations do not change the local energy.

The descriptor $\boldsymbol{D}_i$ is represented as a vector and serves as the input to a function f, whose parameters are fitted to energies and forces obtained from DFT calculations:

$$E_i = f\left(\boldsymbol{D}_i\right) = f\left(\boldsymbol{D}_i(\boldsymbol{R}_i, \{\boldsymbol{R}_j | r_{ij} < r_c\})\right). \tag{2.27}$$

Here, r_c denotes the cutoff radius, beyond which a typically smooth cutoff function is applied to determine which atoms are considered neighbors, and r_{ij} represents the distance between atoms i and j.

The first ML-IAP model was proposed by Behler and Parrinello in 2007. In their approach, a neural network (NN) is used to represent the function f, while the descriptors are constructed using two- and three-body symmetry functions [48]. In the following years, various approaches were introduced to improve the accuracy and computational efficiency of these models, as well as to reduce the amount of required training data. Some of these methods are physically motivated, whereas others rely primarily on the ability of machine-learning models to approximate arbitrary functions f. A comprehensive overview of the different types of potentials and their corresponding software implementations can be found elsewhere [49].

Systematic investigations of different potential types across various material systems were carried out by Zuo et al. [50]. Their study showed that the GAP is able to predict materials properties with high accuracy even when trained on relatively small datasets due to its physically motivated formulation, although this comes at the cost of computational speed. The MTP, on the other hand, is a fast CPU-based potential that still captures most of the material properties. Still, all of these potentials require a non-negligible amount of training data.

In contrast, foundation models have become well established in fields such as computer vision, where only a relatively small amount of data is required to fine-tune a pre-trained model. A state-of-the-art foundation model in the context of interatomic potentials is DPA2, which has been shown to achieve comparable accuracy while requiring fewer training data points [51].

Active learning of ML-IAPs is beyond the scope of this work, although it can significantly reduce the time spent on training-data generation. Depending on the type of potential, different active learning strategies have been proposed. A common feature

of these approaches is that candidate configurations requiring recalculation with DFT are identified through uncertainty estimation. For neural networks, the uncertainty can be predicted by an ensemble of potentials, for example by evaluating the maximum deviation of the energy and forces [52], [53], [54]. For Gaussian-type potentials, this uncertainty is directly available from the kernel functions [55].

To fit a set of parameters $\boldsymbol{\theta}$, a loss function is used to quantify how accurately an ML-IAP reproduces the reference DFT data. Considering a total of K configurations, where each configuration k contains N_k atoms with coordinates $\boldsymbol{R}_k$, a possible loss function can be defined as:

$$\begin{aligned}\text{loss} = \sum_{k=1}^{K} \Big\{ & w_\text{E}[E^{ML}(\boldsymbol{R}_k, \boldsymbol{\theta}) - E^{DFT}(\boldsymbol{R}_k)]^2 + w_\text{F} \sum_{i=1}^{N_k} \|\boldsymbol{F}_i^{ML}(\boldsymbol{R}_k, \boldsymbol{\theta}) - \boldsymbol{F}_i^{DFT}(\boldsymbol{R}_k)\|^2 \\ & + w_\text{S} \|\boldsymbol{\sigma}^{ML}(\boldsymbol{R}_k, \boldsymbol{\theta}) - \boldsymbol{\sigma}^{DFT}(\boldsymbol{R}_k)\|^2 \Big\}.\end{aligned} \tag{2.28}$$

Here w_E, w_F, and w_S denote the weights of the energy, force, and stress contributions, respectively.

This loss function works well if the number of atoms in the configurations is similar. For training datasets containing systems of different sizes, however, the training error for the energy per atom can vary significantly. In such cases, Equation (2.29) provides a normalized form that reduces the effect of system-size variations by averaging the error appropriately.

$$\begin{aligned}\text{loss} = \sum_{k=1}^{K} \Big\{ & \frac{w_\text{E}}{N_k^2}[E^{ML}(\boldsymbol{R}_k, \boldsymbol{\theta}) - E^{DFT}(\boldsymbol{R}_k)]^2 + \frac{w_\text{F}}{N_k} \sum_{i=1}^{N_k} \|\boldsymbol{F}_i^{ML}(\boldsymbol{R}_k, \boldsymbol{\theta}) - \boldsymbol{F}_i^{DFT}(\boldsymbol{R}_k)\|^2 \\ & + \frac{w_\text{S}}{N_k^2} \|\boldsymbol{\sigma}^{ML}(\boldsymbol{R}_k, \boldsymbol{\theta}) - \boldsymbol{\sigma}^{DFT}(\boldsymbol{R}_k)\|^2 \Big\}.\end{aligned} \tag{2.29}$$

2.3.2 Moment Tensor Potential

The MTP was developed by Shapeev [42] and computes the local energy E_i as a linear combination of basis functions $B_\alpha(\boldsymbol{q}_i)$. For a central atom i, all relative distance vectors of the neighboring atoms within a cutoff radius r_c are defined as $\boldsymbol{q}_i := \{\boldsymbol{R}_j - \boldsymbol{R}_i | r_{ij} < r_c\}$. For simplicity, the atom types are already included in the coordinates $\boldsymbol{R}_i$.

$$E_i = \sum_\alpha \xi_\alpha B_\alpha(\boldsymbol{R}_i, \boldsymbol{q}_i) \tag{2.30}$$

In the equation above, $\{\xi_\alpha\}$ are fitting parameters, while the basis functions $\{B_\alpha\}$ serve as descriptors of the local atomic environment. These basis functions obtained by contracting of one or more moment tensors $M_{\mu,\nu}$, which are defined as:

$$M_{\mu,\nu}(\boldsymbol{q}_i) = \sum_j f_\mu(|\boldsymbol{r}_{ij}|, z_i, z_j) \underbrace{\boldsymbol{r}_{ij} \otimes \ldots \otimes \boldsymbol{r}_{ij}}_{\nu \text{ times}} \tag{2.31}$$

A brief introduction to tensor calculations and possible contractions is provided in Appendix A. The moment tensors $M_{\mu,\nu}$ consist of a radial term f_μ and a tensor product

of the distance vectors $\boldsymbol{r}_{ij}$, representing the angular dependence. The scalar basis functions are then obtained by contracting products of these tensors. The radial term is expressed as a sum of Chebyshev polynomials φ^{β}

$$f_{\mu}(|\boldsymbol{r}_{ij}|, z_i, z_j) = \sum_{\beta}^{N_{\text{poly}}} c^{\beta}_{\mu,z_i,z_j} \varphi^{\beta}(|\boldsymbol{r}_{ij}|)(r_{\text{c}} - |\boldsymbol{r}_{ij}|)^2 \tag{2.32}$$

where $\boldsymbol{c} = \{c^{\beta}_{\mu,z_i,z_j}\}$ denotes the radial fitting parameters, z_i the atom type, and N_{poly} the number of polynomials used in the potential.
The level of a moment tensor descriptor is defined by

$$\text{lev}(M_{\mu,\nu}) = 2 + 4\mu + \nu, \tag{2.33}$$

which was determined empirically. A basis function is constructed as a product of moment tensors, and its level is defined as the sum of the levels of all moment tensors from which it is built:

$$\text{lev}(B_{\alpha}) = \prod_{p=1} M_{\mu_p,\nu_p} = \sum_{p} \text{lev}(M_{\mu_p,\nu_p}). \tag{2.34}$$

By introducing a maximum level, all basis functions used in the model must have a level lower than this maximum value. The number of radial fitting parameters $\boldsymbol{c}$ is given by $N_{\text{poly}} \times N_{\text{rad}} \times N^2_{\text{types}}$, where N_{rad} denotes the number of radial functions f_{μ}. The number N_{rad} scales linearly with the maximum level of the potential lev_{max}, whereas the number of basis functions $\{B_{\alpha}\}$ scales exponentially. The interatomic potential was developed and fitted using the MLIP-3 package, which also provided the interface for the LAMMPS molecular dynamics simulations [56].

2.3.3 Gaussian Approximation Potential

The GAP models the behavior of materials by measuring the similarity of two structures. The local energy E_i is decomposed into several components ε_d attributed to a specific descriptor d, taking the local environment $\boldsymbol{q}_i$ as input. In general, two-body, three-body, and many-body descriptors can be used.

$$E_i = \sum_{d}^{\text{descriptors}} \varepsilon_d(\boldsymbol{q}_i) \tag{2.35}$$

For the descriptor d, a kernel k_d is defined to measure the similarity between a given atomic environment $\boldsymbol{q}_i$ and a reference environment $\boldsymbol{q}^{\text{ref}}_m$:

$$\varepsilon_d(\boldsymbol{q}_i) = \sum_{m=1}^{M_d} c^d_m k_d(\boldsymbol{q}_i, \boldsymbol{q}^{\text{ref}}_m) \tag{2.36}$$

The corresponding fitting coefficients are denoted by c^d_m, and M_d specifies the number of reference environments used for fitting the descriptor d. A review of the different kernel variants and descriptors can be found elsewhere [57].

It has previously been shown that the accuracy of ML-IAPs can be significantly improved by using the Smooth Overlap of Atomic Positions (SOAP) descriptor [58]. For each central atom, a separate descriptor is constructed. The neighbor density $\rho^{\alpha}_i(\boldsymbol{r})$ for a central atom i and a neighbor type α is defined as

$$\rho_i^\alpha(\boldsymbol{r}) = \sum_j \delta_{\alpha z_j} \exp\left(-\frac{|\boldsymbol{r} - \boldsymbol{r}_{ij}|^2}{2\sigma^2}\right) f_{\text{cut}}(|\boldsymbol{r}_{ij}|), \tag{2.37}$$

where the sum runs over all neighboring atoms j with atomic type z_j. In Equation (2.38), the neighbor density is expanded as a sum of products of radial basis functions g_n with Y_{lm}, as illustrated in Figure 2.2.

$$\rho_i^\alpha(\boldsymbol{r}) = \sum_{nlm} c_{nlm}^\alpha Y_{lm}(\hat{\boldsymbol{r}}) g_n(|r|) \tag{2.38}$$

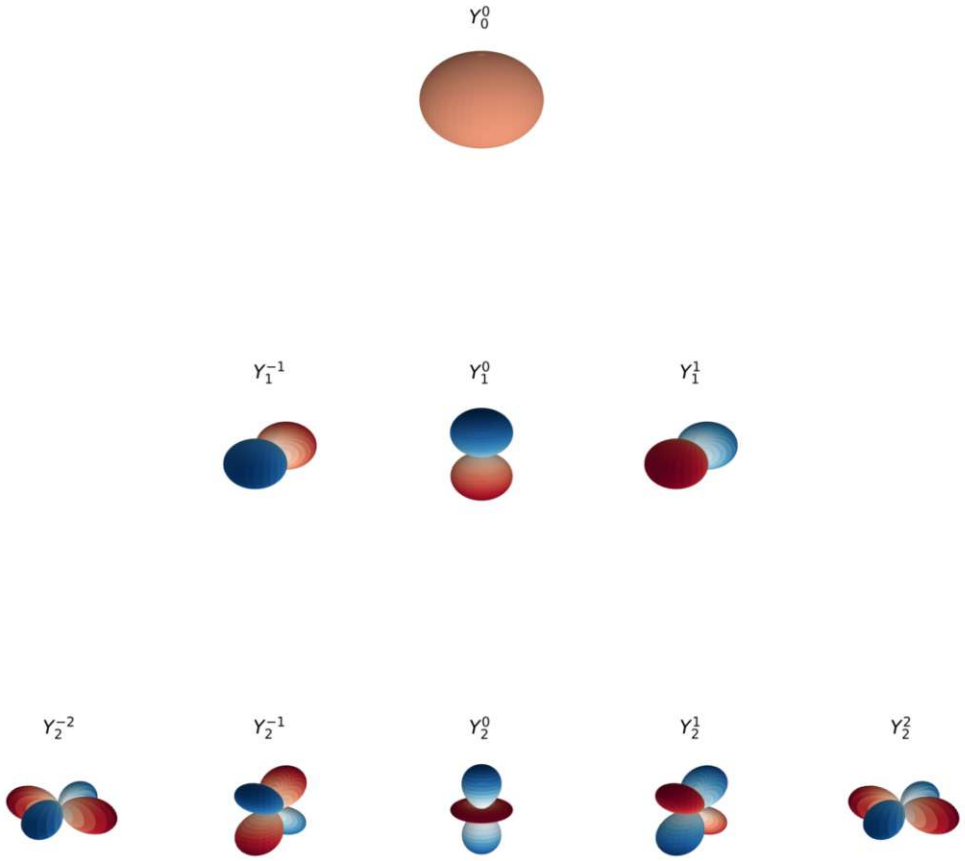

Figure 2.2: Spherical harmonics for $l = 0, 1, 2$ depicted by their isosurfaces.

By comparing the densities $\rho_i^\alpha(\boldsymbol{r})$ and $\rho_{\text{ref}}^\alpha(\boldsymbol{r})$ for all atomic types $\mathcal{Z}$, the similarity between atomic environments can be quantified. To ensure rotational invariance, this comparison must be performed over all possible rotations $\hat{R}$:

$$k(\boldsymbol{q}_i, \boldsymbol{q}_{\text{ref}}) = \int \mathrm{d}\hat{R} \left| \sum_\alpha^{\mathcal{Z}} \int \mathrm{d}\boldsymbol{r} \rho_i^\alpha(\boldsymbol{r}) \rho_{\text{ref}}^\alpha(\hat{R}\boldsymbol{r}) \right|^\nu \tag{2.39}$$

Since the radial basis functions are rotationally invariant, only the spherical harmonics are affected by the rotation. The rotation of spherical harmonics can be performed using:

$$Y'_{lm}(\hat{R}\boldsymbol{r}) = \hat{R}(\alpha, \beta, \gamma) Y_{lm}(\boldsymbol{r}) = \sum_{m'} D^{l}_{m'm} Y_{lm'}(\boldsymbol{r}), \tag{2.40}$$

where $D^{j}_{m'm}$ denotes the Wigner D-matrix element and α, β, and γ are the Euler angles. This transformation also affects the coefficients c^{α}_{nlm}. Setting $\nu = 2$ yields the dot-product kernel, which can be evaluated analytically. Further details can be found elsewhere [59].

During the training process of the GAP, storing the covariance matrices can require a large amount of RAM. This issue can be mitigated by distributing the training process across several computational nodes [60]. Recently, the SOAP_turbo descriptor, an adaptation of the classical SOAP, was introduced, which enhances the computational speed while reducing the required memory [61]. It has been shown that both SOAP variants yield similar results and that a certain level of compression can be applied to further reduce memory requirements without significantly compromising accuracy [59]. The GAP was fitted using the gap_fit method within the QUIP package [62].

2.3.4 Deep Potential Model

For the MTP and GAP, the descriptor is fully determined by a set of hyperparameters, while during the fitting process only the predicted energies, forces, and virials are optimized. In contrast, for the Deep Potential (DP) model, the hyperparameters define only the general form of the descriptor, while the descriptor itself can also be learned during training.

This enables multi-task training, as illustrated in Figure 2.3, where each color represents a different type of dataset. Each dataset has its own fitting layer, which fits properties such as energies and forces, while all datasets share the same descriptor. As a result, the model can cover a wider range of configurations and becomes more robust with respect to extrapolation. Since the descriptor depends only on the atomic geometry, the datasets do not need to be generated using the same DFT setup, for example the same exchange–correlation functional. This reduces the amount of task-specific training data required while maintaining the same level of accuracy. Well-known foundation models are MACE-MP-0 [47], DPA2 [51], and DPA3 [63]. These models are at least partially trained on the Materials Project trajectory dataset (MPTrj) [64]. Due to the increasing number of foundation models, systematic benchmarking and quantification of their performance have been carried out by Peng et al. [65].

In this work, the DPA2 model within the DeepMD [46] package is used because of its faster computation compared to DPA3. The DeepMD package allows the training of several different DP models and introduces an additional ZBL term directly in LAMMPS, which is required for the high-energy impacts occurring during ion implantation. It was therefore chosen over MACE.

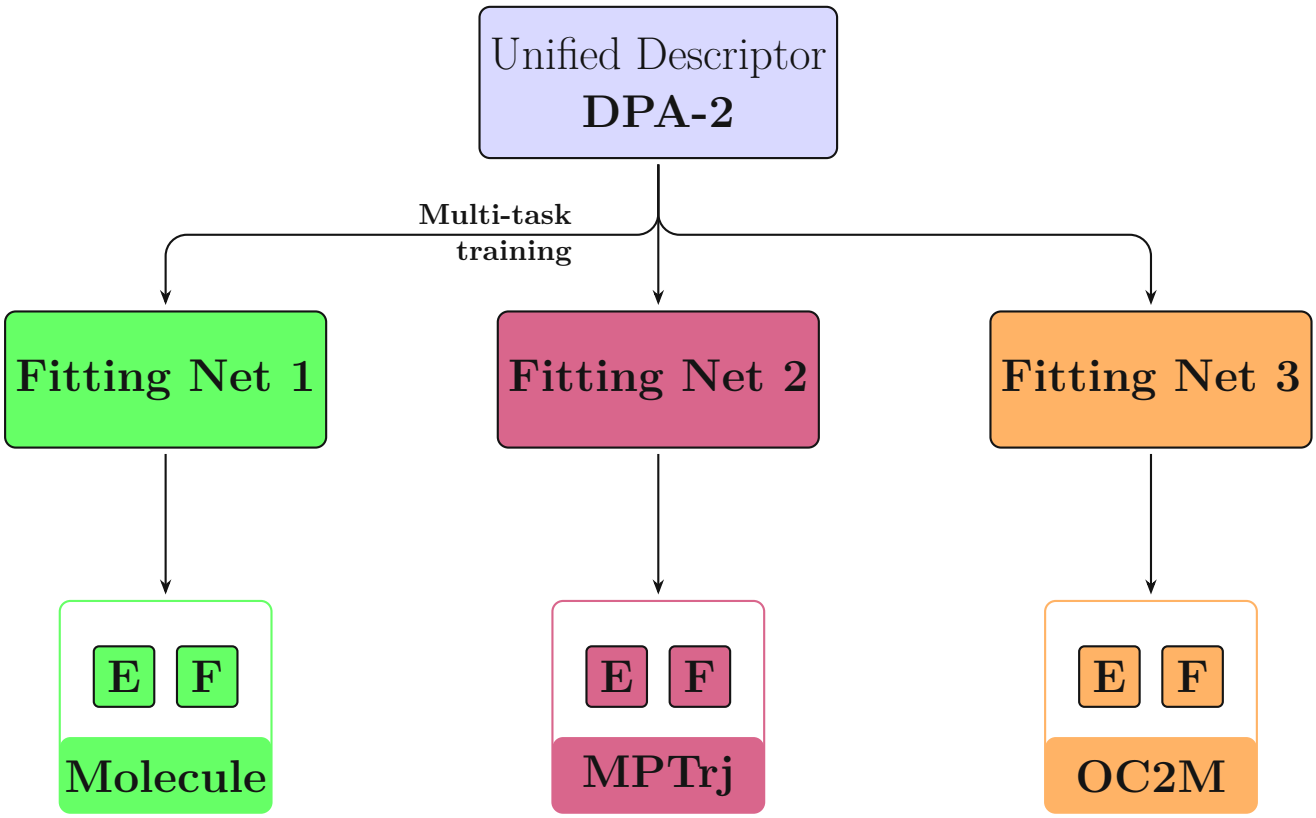

Figure 2.3: Multi-task training with a unified descriptor.

2.4 Applications

Prior to performing large-scale MD simulations, the trained ML-IAPs are evaluated against DFT reference properties, such as phonon spectra, point-defect formation energies, and migration barriers. These comparisons provide a reliable indication of the expected accuracy in subsequent large-scale MD simulations.

2.4.1 Phonon Spectrum

Many material properties, such as thermal conductivity, thermal expansion, optical absorption, and phase transitions, are influenced by lattice vibrations. Furthermore, vibrational spectroscopy is often used to identify structures experimentally.

The following derivation is taken from [66]. First, the displacement vector $\boldsymbol{u}_I$ is defined as

$$\boldsymbol{u}_I = \boldsymbol{R}_I - \boldsymbol{R}_I^0, \tag{2.41}$$

where $\boldsymbol{R}_I^0$ denotes the equilibrium position of atom I. The total energy of the system is expanded in a Taylor series. Since the PES of the system is expanded around the equilibrium positions, the first-order term in this expansion is zero, yielding:

$$E = E_0 + \frac{1}{2}\sum_{I,J} \boldsymbol{u}_I^T \frac{\partial^2 E(\boldsymbol{R})}{\partial \boldsymbol{R}_I \partial \boldsymbol{R}_J}|_{\boldsymbol{R}=\boldsymbol{R}^0} \boldsymbol{u}_J \tag{2.42}$$

with the force matrix:

$$\boldsymbol{\phi}_{I,J} = \frac{\partial^2 E(\boldsymbol{R})}{\partial \boldsymbol{R}_I \partial \boldsymbol{R}_J}|_{\boldsymbol{R}=\boldsymbol{R}^0}. \tag{2.43}$$

The equation of motion for the nuclei reads as

$$M_I \ddot{\boldsymbol{u}}_I = -\sum_J \boldsymbol{\phi}_{I,J} \boldsymbol{u}_J. \tag{2.44}$$

To obtain a solution for propagating waves in the direction of a wavevector $\boldsymbol{q}$, we use a plane-wave ansatz yielding:

$$\boldsymbol{u}_I = \frac{1}{2\sqrt{M_I}}\{A^\nu(\boldsymbol{q})\varepsilon_{I,\nu}(\boldsymbol{q})\mathrm{e}^{i[\boldsymbol{q}\cdot\boldsymbol{R}_I - \omega_\nu(\boldsymbol{q})t]} + A^{\nu *}(\boldsymbol{q})\varepsilon^*_{I,\nu}(\boldsymbol{q})\mathrm{e}^{-i[\boldsymbol{q}\cdot\boldsymbol{R}_I - \omega_\nu(\boldsymbol{q})t]}\}. \tag{2.45}$$

$\varepsilon_{I,\nu}$ is the phonon eigenvector corresponding to mode ν, and A^ν is the amplitude. Inserting the wave propagating in the $+\boldsymbol{q}$ direction from Equation (2.45) into Equation (2.44) results in the following eigenvalue problem:

$$\omega_\nu(\boldsymbol{q})^2 \varepsilon_{I,\nu}(\boldsymbol{q}) = \sum_J \frac{1}{\sqrt{M_J M_I}} \boldsymbol{\phi}_{I,J}\ \mathrm{e}^{i(\boldsymbol{R}_J - \boldsymbol{R}_I)\cdot\boldsymbol{q}} \varepsilon_{I,\nu}(\boldsymbol{q}) \tag{2.46}$$

To account for the fact that each supercell contains multiple unit cells, the nuclei position is written as $\boldsymbol{R}_I = \boldsymbol{r}_i + \boldsymbol{l}$, where $\boldsymbol{r}_i$ is the position within the unit cell and $\boldsymbol{l}$ is a lattice translation vector. The force constants then become $\boldsymbol{\phi}_{I,J} \rightarrow \boldsymbol{\phi}_{li,l'j}$. Therefore, the eigenvalue problem can be written as:

$$\omega_\nu(\boldsymbol{q})^2 \varepsilon_{i,\nu}(\boldsymbol{q}) = \sum_{j,l} \frac{1}{\sqrt{M_j M_i}} \boldsymbol{\phi}_{li,0j}\ \mathrm{e}^{-i\boldsymbol{q}\cdot(\boldsymbol{l}+\boldsymbol{r}_i-\boldsymbol{r}_j)} \varepsilon_{j,\nu}(\boldsymbol{q}) \tag{2.47}$$

In this work, the python library phonopy [67], [68] was used to calculate phonon properties. Additionally, spglib [69] was used to extract the unit cells from supercells.

2.4.2 Defect Modeling

Different defect types are created during the implantation step. The simplest class are point defects, which are localized to a single lattice site or interstitial position:

- **Vacancy:** A missing lattice atom.
- **Interstitial:** An atom that occupies an interstitial site.
- **Substitutional defect:** An atom occupying a lattice site that is normally not occupied by that species. A special case of a substitutional defect is an antisite defect, in which a host atom occupies a substitutional site of a different species.

Before looking at how specific defects diffuse, it is advantageous to examine the thermodynamic stability of different defects. A measure of thermodynamic stability is the formation energy E_{F}, calculated by

$$E_{\mathrm{F}}\left(\boldsymbol{X}^{q}\right)=E\left(\boldsymbol{X}^{q}\right)-E\left(\mathrm{bulk}\right)+\sum_{i}n_{i}\mu_{i}+qE_{\mathrm{Fermi}}+E_{\mathrm{corr}}, \tag{2.48}$$

where $E\left(\boldsymbol{X}^{q}\right)$ is the total energy of the system containing the defect with charge state q, $E\left(\mathrm{bulk}\right)$ is the energy of the perfect cell, μ_i is the chemical potential of the added ($n_i < 0$) or removed ($n_i > 0$) atoms, and E_{Fermi} is the position of the Fermi level. The valence-band edge of the perfect crystal, which corresponds to the Highest Occupied Molecular Orbital (HOMO) of the perfect bulk crystal, is often used as the reference for the Fermi level. Consequently, the defect formation energy depends on both the charge state and the position of the Fermi level. For charged defects, a background charge has to be introduced in the DFT simulation to avoid a diverging total energy. To remove this effect on the formation energy, a correction term E_{corr} as presented in Chapter 2.4.2.1 is introduced. These formation energies are typically visualized in a defect stability diagram, which plots the configuration with the lowest formation energy as a function of the Fermi level.

To evaluate the stability and likelihood of the formation or dissociation of defect complexes, the binding energy E_{b} of a complex consisting of defects A + B, is defined as:

$$E_{b}(\boldsymbol{A}+\boldsymbol{B})=E_{\mathrm{F}}(\boldsymbol{A})+E_{\mathrm{F}}(\boldsymbol{B})-E_{\mathrm{F}}(\boldsymbol{A}+\boldsymbol{B}). \tag{2.49}$$

A larger binding energy $E_b(\boldsymbol{A}+\boldsymbol{B}) > 0$ results in a more stable complex A + B. Evidently, the stability of these complexes shifts depending on the position of the Fermi level.

2.4.2.1 Finite-Size Charge Corrections

Several correction schemes have been proposed to account for a charge correction E_{corr}. For cubic supercells with a length of L, the correction can be calculated with the Makov-Payne (MP) method [70] resulting in

$$E_{\mathrm{corr}}=\frac{q^{2}\alpha}{2L\varepsilon}+\frac{2\pi qQ}{3L^{3}\varepsilon}+O(L^{-5})\approx\frac{q^{2}\alpha}{2L\varepsilon}+O(L^{-3}). \tag{2.50}$$

Here α is the crystal-dependent Madelung constant, ε the dielectric constant, and Q the quadrupole moment. Assuming a sufficiently large supercell, one can neglect the second term, and therefore, the correction energy depends only on the cell size for a given material.

A more sophisticated approach is the Freysoldt-Neugebauer-van de Walle (FNV) [71] correction, which is also applicable to non-cubic cells. The FNV scheme separates the correction into a lattice term and an alignment term. The latter depends on the exact position of the defect. In this work, only the lattice correction is considered, as it is typically larger than the alignment term. The FNV method is implemented in the sxdefectalign software package and was employed because 4H-SiC is a non-cubic crystal.

2.4.2.2 Diffusion of Defects

Formation and binding energies provide a measure of the thermodynamic stability of defects. In non-equilibrium systems, however, they are not sufficient to determine whether the system will actually reach an equilibrium state, because this requires finite-temperature activation. Common atomistic diffusion mechanisms are:

- **Vacancy diffusion:** A vacancy diffuses over the lattice positions.
- **Interstitial diffusion:** An interstitial atom moves through interstitial sites.
- **Recombination:** An interstitial atom and a vacancy recombine. The result can be a perfect lattice site, an antisite, or an activated dopant.
- **Kick-in/out:** An interstitial atom displaces an atom from its lattice site.

Diffusion is generally a stochastic process that can be modeled statistically. For many problems, it is sufficient to employ the phenomenological Fick's first and second laws, which describe diffusion on a macroscopic level.

$$\boldsymbol{J} = -D\nabla n \tag{2.51}$$

$$\frac{\partial n}{\partial t} = D\Delta n \tag{2.52}$$

$$\tag{2.53}$$

Here $\boldsymbol{J}$ is the particle flux, D is the temperature-dependent diffusion constant, which is in general a second-rank tensor, and n is the particle density. The diffusion constant follows an Arrhenius law and is given by:

$$D(T) = D_0 \mathrm{e}^{-\frac{E_A}{k_B T}}. \tag{2.54}$$

Experimentally, the activation energy E_A can be obtained by measuring the diffusion coefficient at different temperatures and fitting an Arrhenius-type function to the data. Theoretically, the diffusion coefficient is proportional to the jump rate of defects between different configurations. This jump rate is described by Transition State Theory (TST) [72]

$$k_{\mathrm{jump}} = \frac{k_{\mathrm{B}} T}{h} \frac{Q^{\dagger}}{Q} \mathrm{e}^{-\frac{E_{\mathrm{m}}}{k_{\mathrm{B}} T}}, \tag{2.55}$$

where $Q^{\dagger}$ and Q are the partition functions of the transition state and the reactants, respectively, and the migration barrier E_{m} is defined as the energy difference on the PES between these states. It can be observed that the activation energy can be approximated by the migration barrier. Using atomistic simulations, the difference in PES need for the migration barrier can be obtained by either the dimer method [73] or the Nudged Elastic Band (NEB) [74]. In this work the latter is used.

2.4.2.3 Nudged Elastic Band Method

An elastic band with $N+1$ images, can be described by the atomic coordinates $[\boldsymbol{R}_0, \boldsymbol{R}_1, \ldots, \boldsymbol{R}_N]$. These images, commonly referred to as replicas, provide a discrete representation of the diffusion path. The band is optimized such that the maximum energy among the replicas is minimized. The image with the highest energy corresponds to the transition state. For each intermediate image, excluding the starting and end replica, a force acts as described in Equation (2.56). The acting force is split into a component of the true energy gradient perpendicular to the tangent and a spring force parallel to the band, as described in Equation (2.56) and Equation (2.57). Here, k is the spring constant, preventing the images from clustering near the minima, which would lead to an inaccurate migration barrier.

$$\boldsymbol{F}_i = \boldsymbol{F}_i^{\parallel} - \nabla E(\boldsymbol{R}_i)_{\perp} \tag{2.56}$$

$$\boldsymbol{F}_i^{\parallel} = k\left(||\boldsymbol{R}_{i+1} - \boldsymbol{R}_i|| - ||\boldsymbol{R}_i - \boldsymbol{R}_{i-1}||\right)\mathbf{e}_{\tau_i} \tag{2.57}$$

$$\nabla E(\boldsymbol{R}_i)_{\perp} = \nabla E(\boldsymbol{R}_i) - \left(\nabla E(\boldsymbol{R}_i)\cdot \mathbf{e}_{\tau_i}\right)\mathbf{e}_{\tau_i} \tag{2.58}$$

Since the images are not allowed to move along the band, a saddle point could exist between two images. To address this limitation, a modified version known as Climbing Image Nudged Elastic Band (CI-NEB) was proposed by Henkelman et al. [75].

At first, the maximum band energy is minimized for a predefined number of iterations, according to Equation (2.56). Subsequently, the force acting on the image with the highest energy $i_{\max}$ is modified according to

$$\boldsymbol{F}_{i_{\max}} = -\nabla E(\boldsymbol{R}_{i_{\max}}) + 2\nabla E(\boldsymbol{R}_{i_{\max}})_{\parallel} = -\nabla E(\boldsymbol{R}_{i_{\max}}) + 2\left(\nabla E(\boldsymbol{R}_{i_{\max}})\cdot \mathbf{e}_{\tau_{i_{\max}}}\right)\mathbf{e}_{\tau_{i_{\max}}}. \tag{2.59}$$

This allows the image to move upwards on the energy landscape due to adapted parallel component of the force. A comparison of both NEB methods is shown in Figure 2.4.

In this work, the CI-NEB algorithm was used. In particular, for the DFT calculations this was done within the CP2K framework [27], whereas the MD simulations were carried out within the Atomic Simulation Environment (ASE) framework [76].

Taken together, the methods introduced in this chapter define the multiscale workflow used throughout the remainder of the thesis. DFT provides the reference energetics, charge-state stability, and migration barriers of selected Al-related defects. These data are then used both as direct physical insight and as training and validation targets for the ML-IAPs. Once benchmarked against crystalline, vibrational, amorphous, and defect properties, the resulting potentials can be applied in large-scale MD simulations of implantation damage and annealing, while the extracted reaction energetics can ultimately serve as input for higher-level kinetic models.

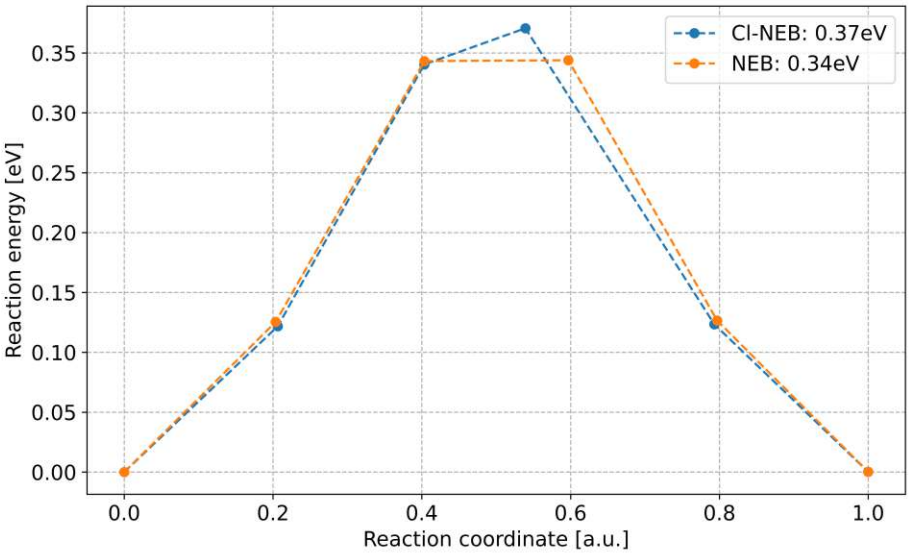

Figure 2.4: Difference in the barrier heights for NEB and CI-NEB.

CHAPTER 3

Results

Before comparing the trained ML-IAP, the stability of the various point-defect configurations is assessed for different charge states using the PBE and PBE0 exchange-correlation functionals. The different types of training structures and the corresponding training setups for the ML-IAPs are then presented. Finally, the resulting models are evaluated by comparing interstitial formation energies, strain properties of different polytypes, phonon spectra, and radial distribution functions (RDFs) of amorphous structures. The RDFs are compared against experimental data from Ishimaru et al. [77], while the remaining properties are compared with DFT reference calculations.

3.1 DFT Study of Aluminium-Related Defects

This section establishes the DFT reference for Al-related defects in 4H-SiC. First, the relative stability of the relevant point-defect configurations is analyzed for different charge states using the PBE and PBE0 exchange-correlation functionals. Subsequently, migration barriers are evaluated to identify the defect configurations and diffusion mechanisms most relevant for the later comparison with the trained ML-IAPs.

In Figure 3.1, the point-defect stability diagram for Al interstitials calculated with the PBE functional is shown. To find the lowest energy configuration for each defect and charge state, all neighboring atoms within 4 Å of the defect were randomly displaced followed by a geometry optimization. This was repeated several times, and only the most stable configuration was used for the formation diagram. The Highest Occupied Molecular Orbital (HOMO) and Lowest Unoccupied Molecular Orbital (LUMO) of the pristine supercell are used as approximations to the valence and conduction band edges, respectively. The most stable point-defect configurations are located within the hexagonal and cubic cages for all charge states. However, it was found that metastable Al-Si split interstitials exist on the silicon lattice sites. Matsushima and Yamauchi [78] reported those Al-Si metastable splits as well in 3C-SiC, which further confirms these findings.

For nearly all positions of the Fermi level within the band gap, the interstitial Al defects exist in the +3 charge state. Only in the highly n-type region do neutral charge

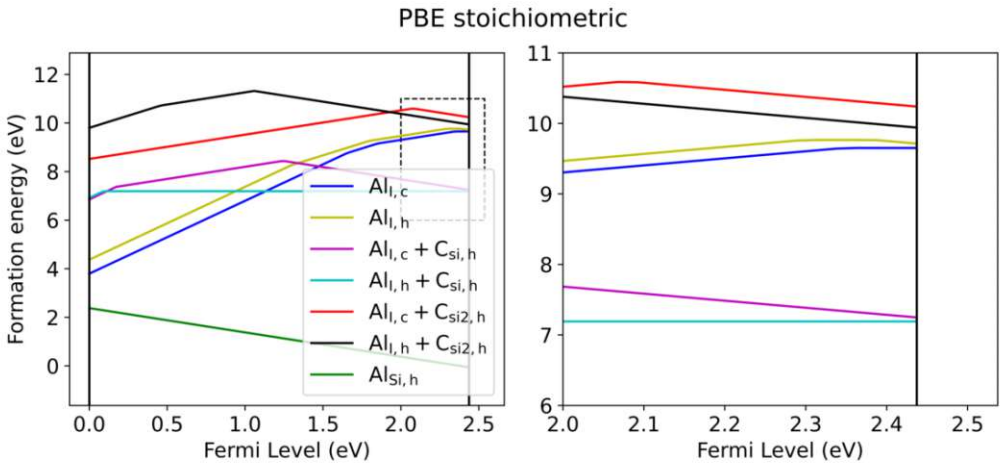

Figure 3.1: Formation energy diagrams for various point defects in 4H-SiC evaluated within DFT-PBE.

states become favorable, see Figure 3.1 (right).

Gali et al. showed that $Al_{Si}^{-}C_I$ decomposes into $Al_{Si}^{-} + C_I$, due to a binding energy of 0.8 eV for a Fermi level located in the mid-gap [6]. It was also reported that a di-carbon antisite $(C_{Si})_2$can be kicked out of the silicon lattice by an interstitial Al_I, due to its high binding energy of 5.8 eV. In Figure 3.2, the binding energy is plotted as a function of the Fermi-level position, where a positive energy indicates higher stability with respect to the products. This supports the findings of Gali et al. that not only dicarbon antisites but also classical antisites can lead to the activation of Al. Furthermore, it shows that silicon interstitials can deactivate an already activated Al via a two-step process, as described in Equation (3.1).

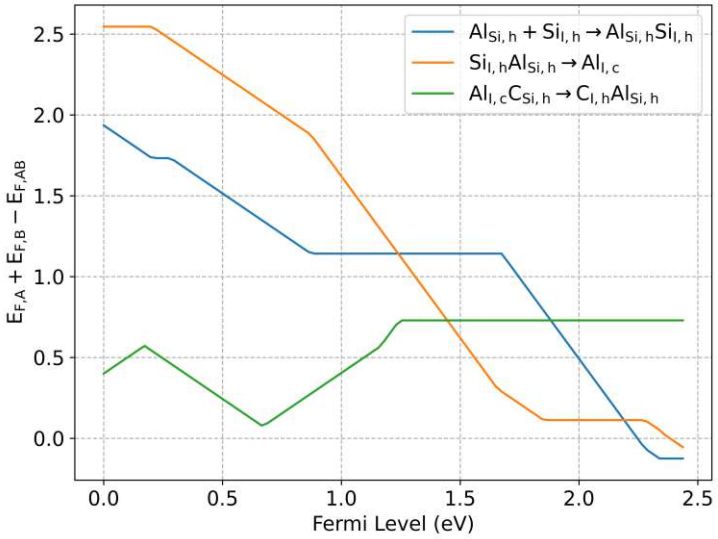

Figure 3.2: DFT-PBE point defect binding energies for an Al activation process.

$$\mathrm{Al_{Si,h}} + \mathrm{Si_{I,h}} \rightarrow \mathrm{Al_{Si,h}Si_{I,h}} \rightarrow \mathrm{Al_{I,c}} \tag{3.1}$$

All defects have in common that neutral charge states exist only for Fermi levels close to the conduction band. This results in Kohn-Sham states near the conduction band, making them difficult to model with DFT since they can hybridize with conduction-band states and may require electronic smearing, as in metals. This effect is further amplified by the underestimation of the band gap within the PBE functional. Establishing a more reliable hybrid-functional reference is therefore important, as the neutral charge state is the one most directly relevant for the later comparison with classical MD simulations.

To check whether the thermodynamic stability of charged defects changes with a corrected band gap, a hybrid functional can be used, mixing in a correct fraction of the Hartree-Fock exchange potential. In this study, a range-seperated variant of the PBE0 (PBE0_LRC_TC) functional was chosen over the HSE due to its higher computational efficiency. A fraction of 0.25 HF exchange was used within a cutoff radius of 2 Å. While this fraction corresponds to the standard value, the cutoff radius was tuned such that the band gaps obtained with PBE0 and HSE align with each other.

In Figure 3.3, the defect formation diagrams calculated with PBE0 are shown. For defects containing carbon antisites, different charge states are expected compared to PBE, whereas the influence on Al interstitials is negligible. In contrast to the results from Gali et al.[6], the binding energy for the $\mathrm{Al_{Si}^{-}C_I}$ defect is positive for all states of the Fermi level within the band gap. To assess whether the observed difference arises from self-interaction error (SIE), one can test whether Koopmans' condition is fulfilled.

$\mathrm{Al_{Si}^{-}C_I}$ decomposes into $\mathrm{Al_{Si}^{-}} + \mathrm{C_I}$

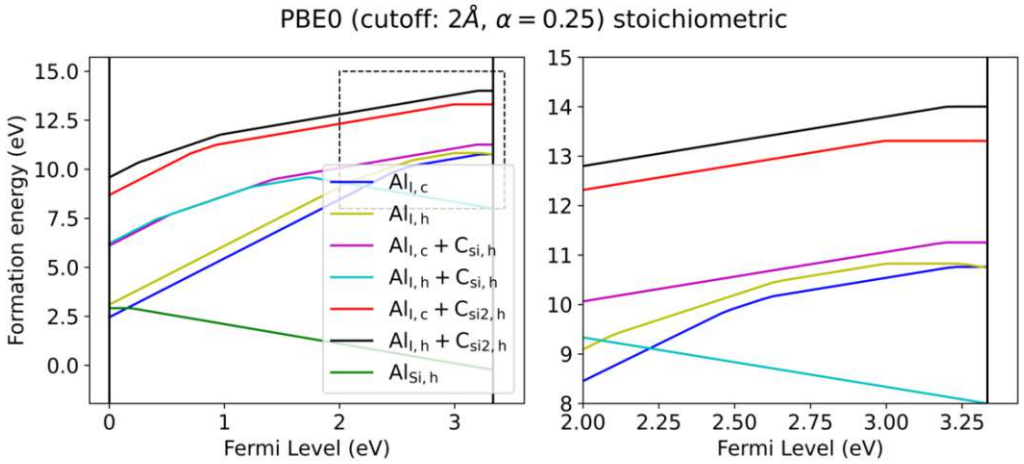

Figure 3.3: DFT-PBE point defect binding energies for an Al activation process.

Since the PBE0 setup was tuned to match the HSE band gap, it does not necessarily fulfill Koopmans' theorem, which writes for an additional electron as

$$\varepsilon_{N+1}(N) = E(N+1) - E(N) \tag{3.2}$$

and for a hole as

$$\varepsilon_N(N) = E(N) - E(N-1). \tag{3.3}$$

For the PBE functional, the energy of the ground state is a curved function on the number of electrons. This curved relation is caused by a self-interaction error (SIE), since the exchange potential is not described accurately [79]. To apply the Equation (3.2) and Equation (3.3), a point defect that introduces states within the perfect crystal is needed. E(N) and E(N+1) are the already charge-corrected total energies of the system with N and N+1 electrons, respectively. $\varepsilon_{N+1}(N)$ is the LUMO and refers to the N+1 defect state in an N electron system [80].

As a test defect, a carbon split interstitial in the hexagonal lattice site was used, and for a fixed cutoff, the Hartree-Fock exchange fraction α was varied. It was found that for a cutoff of 2 Å, no α value was able to satisfy either of the Koopmans conditions. This explains, to a certain point, the difference between the formation diagram for the PBE and PBE0 as well as the difference in the binding energies compared with Gali et al. [6].

For a cutoff of 4 Å, a Hartree-Fock exchange fraction of 0.16 was able to satisfy the conditions, which is in agreement with previous studies by Elmaslmane et al. [81], who used the same DFT code and computational setup and also required a larger cutoff. A similar value for the exchange fraction was obtained by Miceli et al. [82], who also used the PBE0 functional but with a different DFT code for SiC.

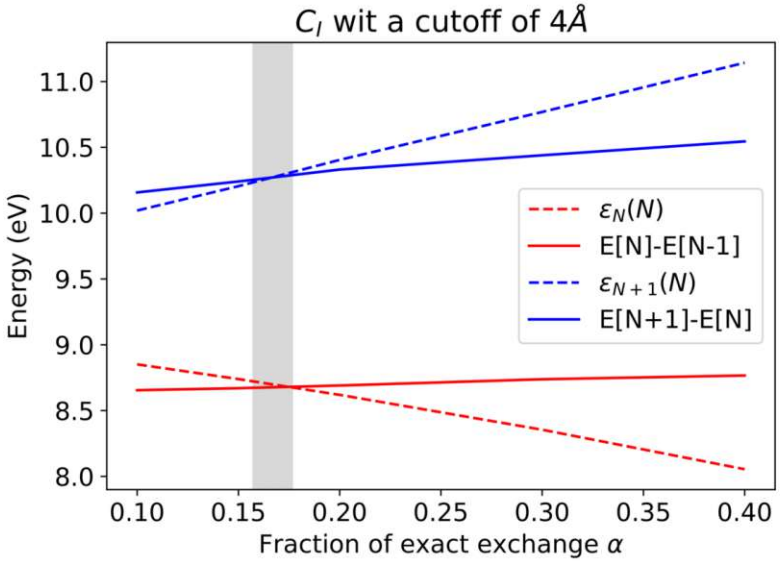

Figure 3.4: Exchange fraction sweep to fulfill the Koopmans condition.

Huang et al. investigated the diffusion of Al interstitials as well as the kick-out process involving a Si interstitial for several charge states [83]. Diffusion barriers in the range of 2.4 eV to 2.8 eV were reported. However, it is unclear how these results can be directly transferred to Al diffusion in MD simulations, as classical MD typically assumes a neutral charge state.

Figure 3.5 shows the migration barrier of an Al interstitial in the cubic cage for the neutral charge state. The two global minima are attributed to distorted defects. This

effect arises from the three valence electrons of Al, which prefer to form bonds with three surrounding carbon atoms rather than four, as would occur at the highest-symmetry position. The local minima in the middle are caused by the formation of an Al-Si split interstitial. Therefore, diffusion in the cubic plane proceeds via alternating hopping between the distorted configurations and an Al-Si split. This is similar to the diffusion path of boron in SiC [84]. In Table 3.1, it can be seen that the energy barrier of 0.71 eV is significantly lower than the values for the +3 charge state, being 2.87 eV respectively.

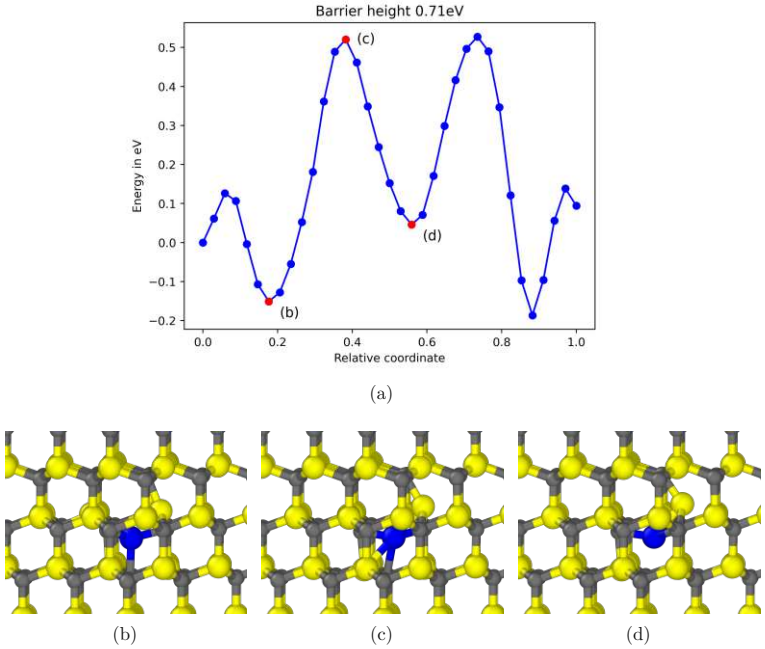

Figure 3.5: Migration barrier of Al_I in the cubic plane in the neutral charge state. (a) Migration barrier, (b) distorted $Al_{I,c}$ configuration, (c) saddle point, and (d) Al-Si split interstitial as an intermediate configuration.

For the migration of Al interstitials, the kick-in barrier in the neutral charge state is 1.57 eV, which is significantly lower than the barriers reported by Huang et al. [83] for charged states. During the kick-in process, a metastable Al-Si configuration within the basal (0001) plane is formed. A summary of the calculated barriers is provided in Table 3.1. It can be seen that the barrier heights for the +3 charge state, except for the kick-in process, are in good agreement with the values reported in the literature [83].

Some CI-NEB calculations did not converge for the neutral charge state due to changes in the electronic structure during the iteration steps. This behavior is attributed to electronic states located near the conduction band, which are occupied in the neutral charge state. During diffusion, these Kohn-Sham states shift into the conduction band, thereby altering the electronic structure and consequently the behavior of the system. The corresponding barriers and atomic configurations for the +3 charge states are provided in the Appendix B.

the DFT calculations establish three key reference results for the subsequent validation of the trained ML-IAPs. First, neutral Al interstitial diffusion in the basal plane proceeds through a metastable Al-Si split configuration and exhibits substantially lower barriers than the corresponding +3 processes. Second, silicon interstitials can provide a physically plausible deactivation route for already substitutional Al through kick-in or

Process	**+3** ([83])	**0**
basal-plane diffusion (cubic)	2.87 eV (2.4 eV)	0.71 eV
out of plane	2.98 eV (2.6 eV)	
Al kick-in	2.87 eV (6.135)	1.57 eV

Table 3.1: Migration and kick-in/-out barriers of Al in 4H-SiC in different charge states.

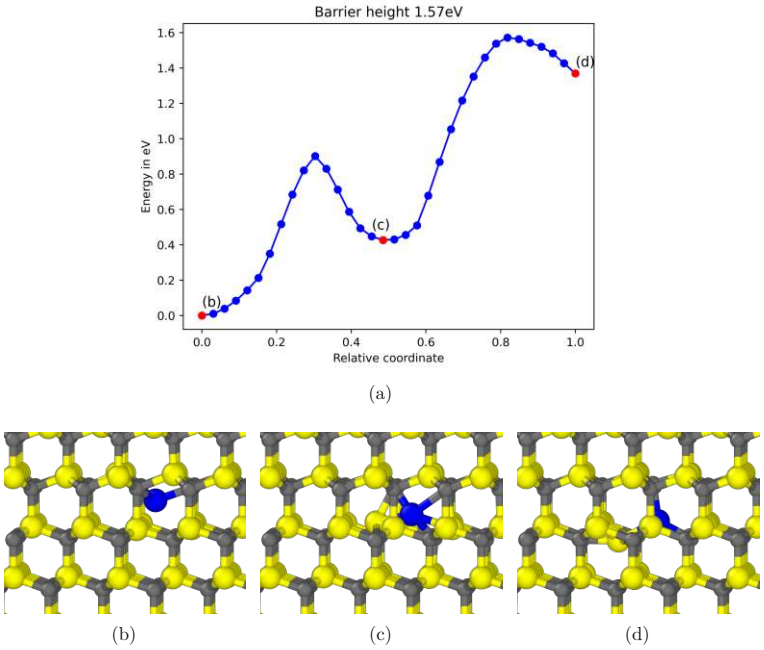

Figure 3.6: Kick-in mechanism of $Al_{I,h}$ in the neutral charge state. (a) Migration barrier, (b) $Al_{I,h}$ configuration, (c) meta-stable state being an Al-Si split in $[\bar{1}2\bar{1}0]$ direction, and (d) end position $Al_{Si,h} + Si_{I,c}$

kick-out-like reactions. Third, the sensitivity of neutral-state barriers to the electronic structure shows that these mechanisms cannot be inferred reliably from charged-state calculations alone. These features therefore define the most demanding targets for the later atomistic models.

3.2 Machine Learning Interatomic Potential Training

The training data must cover both near-equilibrium crystalline environments and the strongly distorted local environments that occur during implantation and subsequent annealing. For that reason, the dataset combines static structures that constrain defect energetics and crystalline reference states with finite-temperature and cascade-derived configurations that sample bond breaking, disorder, and highly coordinated environments. The goal is not only to minimize the test error, but also to expose the ML-IAPs to the relevant parts of configuration space for the simulations targeted in this thesis.

To train a ML-IAP, a suitable training set had to be generated, as there was no

existing dataset available for the ternary Al-Si-C system. The training dataset consists of the following types of structures:

- **Single atoms:** One atom of each type, used to define the self interaction energy E_0 for each particle.
- **Dimers:** Two atoms, with varying interatomic distances.
- **Unit cells:** Scaled unit cells for the polytypes.
- **Surfaces:** Snapshots from ab-initio AIMD simulations for the (0001) and $(\bar{1}2\bar{1}0)$ planes.
- **Silicon interstitials:** Snapshots obtained from geometry relaxations of several silicon interstitial defects.
- **Carbon interstitials:** Snapshots obtained from geometry relaxations of several carbon interstitial defects.
- **Vacancies:** Snapshots obtained from geometry relaxations of several vacancy defects.
- **Antisites:** Snapshots obtained from geometry relaxations of several substitutional defects.
- **Al-related defects:** Snapshots obtained from geometry relaxations of several Al-related defects.
- **Al cascades:** Snapshots from displacement cascades with inserted Al atoms with kinetic energies of 100 eV, 150 eV, and 200 eV, mimicking ion implantation.
- **Amorphous structures:** Snapshots from melt-quench simulations used to generate amorphous SiC.

Since the GAP requires single atoms to be placed in a unit cell, these were used to define the reference energy E_0, which was set to zero. Consequently, for each atom of the same type in a unit cell, the electronic energy of an isolated atom was subtracted.

To accurately describe different polytypes, perfect unit cells were stretched along the [0001] and $[\bar{1}2\bar{1}0]$ directions.

Due to the high energy of the implanted ions, dimer configurations were included as additional safeguards. For the single atoms and dimers, cells with dimensions of $20\,\text{Å} \times 20\,\text{Å} \times 20\,\text{Å}$ were employed to suppress interactions between periodic images.

Diverse defect types were included in the training set by placing atoms in configurations away from their equilibrium positions. These configurations were then relaxed using DFT, and snapshots from the relaxation process were collected as training data. Some of these structures are shown in Figure 3.7. Since these structures were generated from geometry relaxation rather than finite-temperature trajectories, they are referred to as static in the following.

Significant effort was dedicated to describing amorphous structures accurately, as high-dose ion implantation inevitably leads to amorphization. Previously, GAPs were used to model and understand the atomistic structure of amorphous carbon [58] and

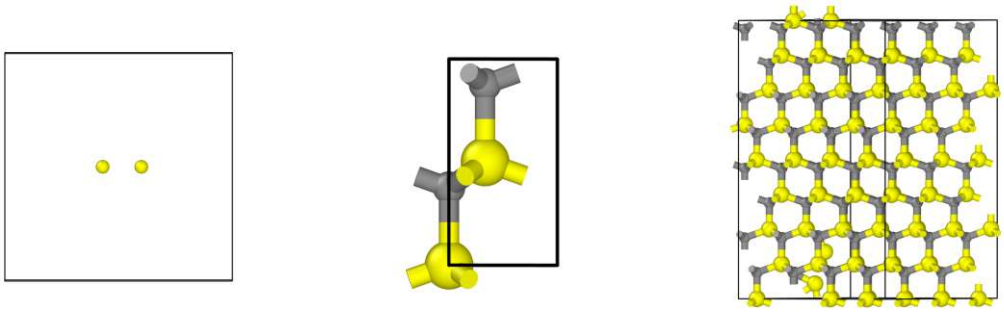

(a) (b) (c)

Figure 3.7: Quasi-static dataset consisting of (a) dimer configurations, (b) scaled perfect unit cells, and (c) point defects.

silicon [85]. The same general strategy for creating amorphous training structures was adopted here for SiC. First, a structure with 128 atoms was molten using the GW potential. Those cells were then scaled to produce densities of $2.8\,\mathrm{g\,cm^{-3}}$, $3\,\mathrm{g\,cm^{-3}}$, $3.21\,\mathrm{g\,cm^{-3}}$, and $3.4\,\mathrm{g\,cm^{-3}}$, respectively. Following those steps, an ab initio MD simulation with a timestep size of 1 fs, and a duration of 1 ps was carried out at a temperature of 6500 K to capture a wide range of configurations. Snapshots were written out every 10 fs. A k-grid of 2x2x2 was used, and the first timesteps were discarded from training and validation to make sure that only the most physical structures were included. Afterwards, the cells were quenched down to a temperature of 300 K with a rate of 10^{14} K/s. This melt-quench data was first used to train a level-20 MTP. In the next iteration, the initial molten structures were generated with the trained MTP instead of the GW potential, relabeled with DFT, and added to the dataset. This iterative melt-quench procedure was then repeated once more. In this way, the amorphous part of the training set was gradually shifted away from the bias of the GW potential toward structures that are more self-consistent with the fitted ML-IAP.

Surface structures were generated using AIMD, with a 10 Å vacuum added between the perfect surfaces, and periodic boundary conditions applied in all directions. Due to the short timescales of the simulations, no surface reconstruction was considered, and it is not expected in ML-IAP simulations either, since such configurations are not present in the training data.

Lastly, to mimic defect creation during high-energy impacts, single Al atoms with kinetic energies of 100 eV, 150 eV, and 200 eV were randomly inserted into a perfect crystal with periodic boundary conditions. Dynamic timestepping was applied such that atoms were not allowed to move more than 0.05 Å per step. After each cascade, the system was equilibrated for 6000 steps in the NVE ensemble, followed by 2000 steps in the NVT ensemble to reach a temperature of 300 K before the next Al was inserted. For each of those three energies, 20 Al atoms were inserted into the cell. As an IAP, a DPA2 model with six layers was trained on the MPTrj [64] and SemiCond [86] datasets.

Some of these dynamically generated MD structures are shown in Figure 3.8. A summary of the data contained in the dataset is provided in Table 3.2. The data were split into training, validation, and test sets using a ratio of 70/20/10. For a fair comparison of the different ML-IAP models, the 70% training fraction was also maintained for GAP and MTP, even though these models only distinguish between

training and test sets.

Structure	Atoms/cell	kpoints	Data points
Single atoms	1	Γ-point	3
Dimers	2	Γ-point	122
Unit cells	4/6/8	8x8x8	240
Surfaces	128	3x3x3	393
Silicon interstitials	385	2x2x1	319
Carbon interstitials	385	2x2x1	296
Vacancies	383	2x2x1	33
Antisites	384	2x2x1	41
Al related defects	384/385	2x2x1	244
Al cascades	385+	Γ-point	277
Amorphous structures	128	2x2x2	817

Table 3.2: Content of the DFT database used for training ML-IAP

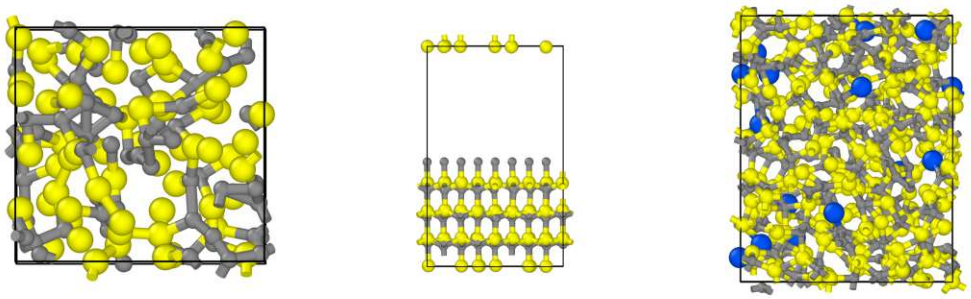

(a) (b) (c)

Figure 3.8: Trajectory snapshots consisting of (a) amorphous SiC generated via a melt-quench simulation, (b) AIMD simulations of perfect surfaces, and (c) Al cascade simulations.

The MTP was trained for levels 14, 16, 18, and 20 using eight radial basis functions. The weights for the energy and forces, the cutoff radius, and the type of loss function, as described in Equation (2.28) and Equation (2.29), were optimized using the Python library GPyOpt [87]. It implements a Bayesian optimizer that searches for a set of hyperparameters yielding a minimal loss within a given range. Since the MTP allows the use of different loss functions, which can be specified by integer variables, an optimizer capable of handling integer variables was required, which is supported by GPyOpt. To keep the optimization time relatively low, only 20% of the overall training structures were used. The best performance was obtained when Equation (2.29) was used for both the energy and force loss functions, since different cell sizes were included in the training set. An optimized cutoff radius of 4.86 Å yielded the best results. In general, higher levels resulted in lower training errors, although level 18 appeared as an outlier as seen in Figure 3.9. This is likely caused by a local minimum in the optimization process, in which the potential optimizer becomes trapped. For further comparison with other ML-IAP models, level 20 was used in the rest of this thesis.

For the GAP, the setup from Klawohn et al. was taken as a reference [59], employing a combination of a two-body descriptor and a SOAP descriptor. Two different GAP models were trained within this thesis. Both models used a two-body descriptor, while in the SOAP descriptor was used and in the other one the SOAP_turbo. The default sigma values for energies and forces, together with the SOAP parameters including radial scaling, cutoff distance, and the Gaussian smearing width of the atomic density, were optimized using the Python library GPyOpt [87]. The best results were obtained with a cutoff of 3.63 Å, a Gaussian smearing width of 0.71 Å, and a radial scaling of -1.92. No significant difference was observed for different values of $l_{\max}$ and $n_{\max}$. Therefore, $l_{\max} = 4$ and $n_{\max} = 6$ are used in the following sections for comparison. These optimized parameters were also used for the SOAP_turbo descriptor. In addition, the number of sparse points for the two-body and SOAP_turbo descriptor was decreased, and the weight assigned to point-defect data was increased. To improve the fitting time, compression was also employed, which was shown to yield similar results when the trivial compression scheme was used, which is only available for the SOAP_turbo [59]. A detailed description of the parameter translation can be found elsewhere [13].

Lastly, the DPA2 model was trained using a multi-task training procedure. For the additional tasks, the MPTrj [64], Transition1X [88] and SemiCond [86] datasets were used. For the DPA2 model, a cutoff of 4 Å, six repformer layers, and float64 precision was used. During the training process, it is possible to control how frequently specific training data, e.g., point-defect structures, are used in the fitting procedure. In this way, greater weight is assigned to structures that appear more frequently. Nevertheless, a lower overall training and test error was achieved by using automatic batch-size scaling while increasing the number of training steps to $2 \cdot 10^6$. Different DPA2 variants were trained by varying the neuron numbers inside the descriptor as well as in the fitting layer. The best results were achieved for 25x40x40 neurons in the descriptor and 180x180x180 neurons in the fitting layer.

In Figure 3.9, the accuracy of each potential is plotted as a function of the computational time. Both SOAP variants and the MTP were benchmarked on a single CPU core, whereas the DPA models were benchmarked on a single GPU. For the benchmark, a perfect 4H-SiC structure containing 1728 atoms at a temperature of 300 K was simulated using the NVE ensemble.

The best-performing MTP achieves similar accuracy to the SOAP descriptor and slightly outperforms SOAP_turbo, while being approximately one order of magnitude faster. Replacing the SOAP descriptor with SOAP_turbo resulted in a speedup of 3.5, which can be attributed to the more efficient SOAP_turbo implementation and the reduced number of sparse points. Even when both models used 4000 sparse points, a speedup of approximately three was still achieved. In this work, both SOAP variants were trained with increased weights on selected structures, which leads to increased extrapolation for the remaining data. This effect is more pronounced for SOAP_turbo and is likely caused by the inclusion of point defects in the high-weighted subset of the training data.

Both DPA variants yielded smaller test errors, with the DPA3 providing higher computational speed and lower errors compared to DPA2. The best DPA3 fit uses a cutoff of 4 Å whereas the second DPA3 uses 6 Å. However, due to their higher model complexity, both DPA3 and DPA2 require a large amount of GPU memory. For DPA3, it was necessary to reduce the system size, and even for 1152 atoms, approximately 10

GB of GPU memory was required. The DPA3 model already uses float32 precision and automated scaling of the n_{sel} parameters, which define the maximum number of neighbor atoms for each atom type. In contrast, this parameter is fixed for the DPA2, meaning that a significant amount of memory is wasted without further tuning. By reducing the numerical precision and the number of layers in DPA2, faster potentials can be obtained while significantly reducing the memory usage as shown in Appendix Figure C.1, where DPA2: $\mathrm{n_{sel}} = 120$, $\mathrm{n_{sel,3b}} = 48$, $\mathrm{n_{sel,rep}} = 48$, $\mathrm{n_{layers}}$=6, float64, is the benchmark model within this thesis. Since the subsequent validation sections require repeated calculations for larger systems and on more broadly available hardware, the detailed comparisons below focus on MTP, SOAP, SOAP_turbo, and the benchmark DPA2 model. DPA3 remains important as a proof that the deep-learning approach can achieve even lower test errors, but in its present form it is less practical for the full validation workflow carried out here.

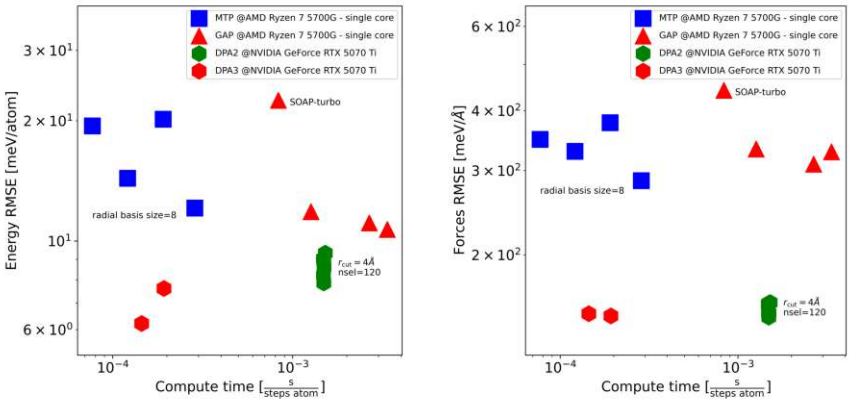

(a) (b)

Figure 3.9: Accuracy versus computational cost for different ML-IAPs: (a) energy test error and (b) force test error.

In Figure 3.10, the energy test correlation errors for the best fit of each potential type are shown. The GAP with SOAP and the MTP with level 20 yield similar results for both the RMSE and MAE. A slightly worse performance in terms of accuracy is observed for the SOAP_turbo model. The best performance was achieved with the DPA2 model, with an RMSE of 7.5 meV/atom and an MAE of 3.9 meV/atom. A similar trend is observed for the force test correlation errors shown in Figure 3.11. The difference between the SOAP and SOAP_turbo models is slightly smaller for the forces than for the energies. Further training details for all ML-IAPs are provided in Appendix C.

Overall, the fitting metrics already separate the models into different practical use cases. DPA2 provides the best agreement with the reference dataset, whereas MTP offers the most favorable compromise between accuracy and computational cost on CPU hardware. The SOAP-based models remain competitive for near-equilibrium properties but are more expensive and somewhat less robust once selected subsets of the training data are strongly upweighted. At the same time, low training and test errors alone do not guarantee accurate migration barriers, defect ordering, or amorphous coordination. For that reason, the following sections focus on property-based validation rather than on fitting errors alone.

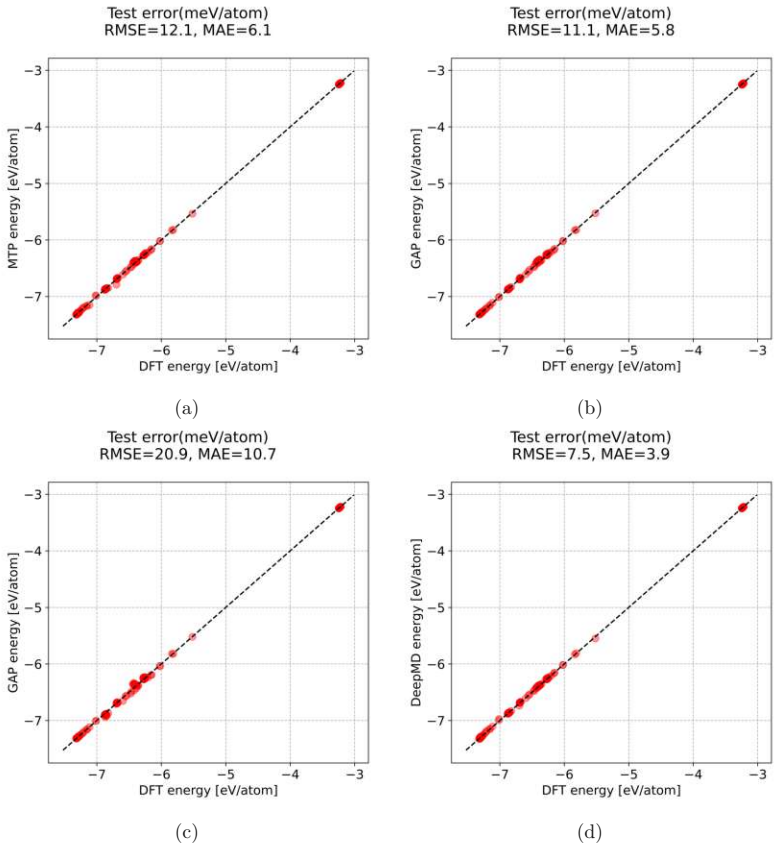

Figure 3.10: Energy test error for (a) MTP level 20, (b) GAP with SOAP, (c) GAP with SOAP_turbo, and (d) DPA2

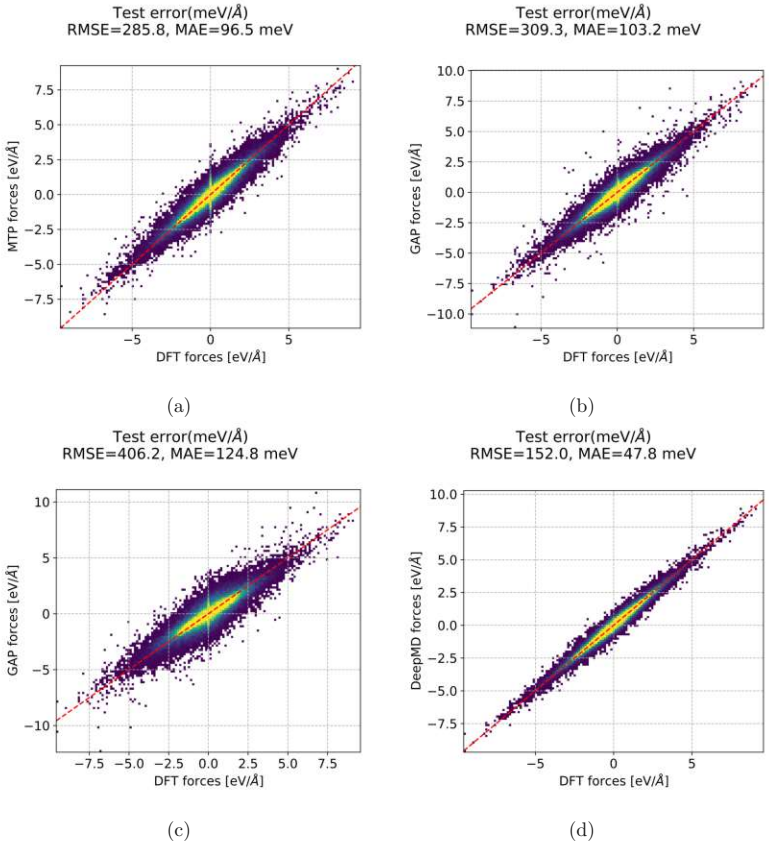

Figure 3.11: Force test error for (a) MTP level 20, (b) GAP with SOAP, (c) GAP with SOAP_turbo, and (d) DPA2

3.3 Elastic Properties

Elastic constants describe the relation between the mechanical stress σ and the strain ϵ. Furthermore, an accurate description across various thermodynamic conditions is required to predict the phase diagram, since SiC exists in many different polytypes. It has also been shown that the type of polytype formed during implantation and annealing depends on the annealing temperature as well as on the ion dose [89]. In SiC, it was further reported that the strain that builds up during ion implantation results from the accumulation of isolated point defects [90]. Therefore, it can be assumed that correctly describing point-defect diffusion under various implantation conditions requires an accurate description of the elastic properties. Recent studies have successfully investigated the applicability of ML-IAPs to reconstruct phase diagrams for SiC [17]. This study indicates that, even at medium pressures (0.01 MPa - 1 GPa), liquid Si can coexist with graphite, highlighting that strain properties play an important role. Since this exact description goes beyond the scope of the present work, only the elastic constants are compared with DFT data and values reported in the literature.

It can be shown that the energy ΔU, defined as the difference between the system energy and the minimum energy, has a quadratic dependence on strain [91]. Without considering shear strain, i.e. when only normal strain is considered, ΔU can be expressed as

$$\frac{\Delta U}{V} = \frac{1}{2} C_{ij} \epsilon_i \epsilon_j. \tag{3.4}$$

In order to estimate the elastic constants C_{11} and C_{33}, strains of $\epsilon = \pm 0.08$ were applied. This value is relatively large compared to typical DFT simulations but was chosen to demonstrate an accurate description of the PES under various conditions. In Figure 3.12, the resulting energy curves are plotted as a function of the applied strain for 4H-SiC. All potentials provide a good fit for both the elastic constants and the minimum energy.

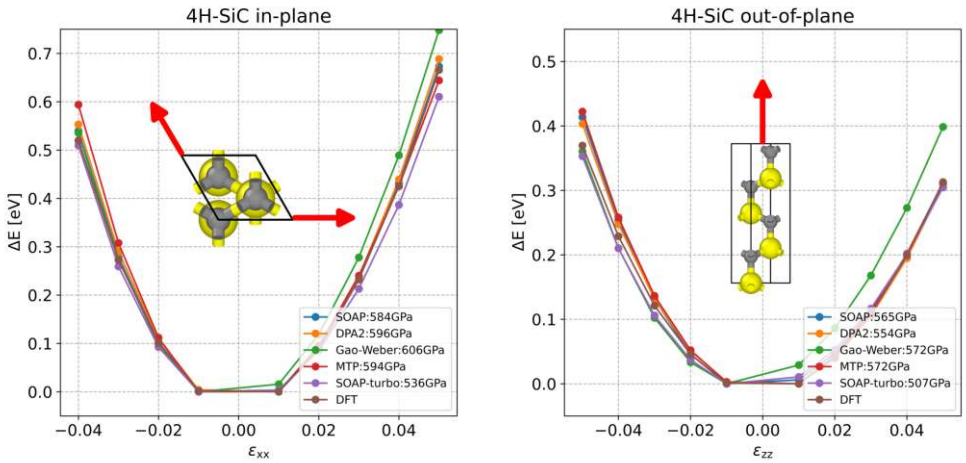

(a) (b)

Figure 3.12: PES of 4H-SiC under applied strain up to $\epsilon = \pm 0.08$ (a) biaxial along the $[\bar{1}2\bar{1}0]$ and $[\bar{1}\bar{1}20]$ directions, and (b) along the [0001] direction.

In Table 3.3, the fitted elastic constants are shown for 2H-SiC and 4H-SiC. Except

for the C_{33} value obtained with SOAP_turbo, all constants are slightly overestimated compared to the literature data [92]. This is likely caused by the relatively large strains applied in the calculations. Additional energy curves are provided in Appendix D.

2H-SiC

Structure	**MTP**	**SOAP**	**SOAP_turbo**	**DPA2**	**GW** [9]	**DFT** [92]
$\boldsymbol{C}_{11}$ (GPa)	585	595	565	609	614	494
$\boldsymbol{C}_{33}$ (GPa)	559	562	494	540	543	532

4H-SiC

Structure	**MTP**	**SOAP**	**SOAP_turbo**	**DPA2**	**GW** [9]	**DFT** [92]
$\boldsymbol{C}_{11}$ (GPa)	594	584	536	596	606	490
$\boldsymbol{C}_{33}$ (GPa)	572	565	507	554	572	533

Table 3.3: Summary of the obtained elastic constant C_{11} and C_{33} for 2H-SiC and 4H-SiC.

3.4 Vibrational Properties

Phonons are of great importance as they represent quantized lattice vibrations. Figure 3.13 shows the phonon spectrum of 4H-SiC for the different ML-IAPs. The upper branches correspond to the optical phonons, whereas the three lowest branches correspond to the acoustic phonons. Acoustic phonons are particularly important for thermal conductivity, as they are responsible for dissipating the excess energy generated during ion implantation [93]. They are also important for the heat capacity. All ML-IAPs exhibit difficulties in accurately describing the high-frequency modes, since these modes are sensitive to small force deviations. The phonon dispersion around the Γ-point is similar across the different ML-IAPs, but deviates increasingly from the DFT results further away from the Γ-point, especially for the highest acoustic mode. This suggests that the general PES is reasonably well captured, whereas small deviations are not accurately reproduced. Similar trends are observed for the 3C-SiC phonon spectrum shown in Figure 3.14. Since no data was explicitly generated for matching the phonon spectra, the agreement is still acceptable. For a detailed analysis of the capability to model phonon spectra, they have to specifically added into the training set.

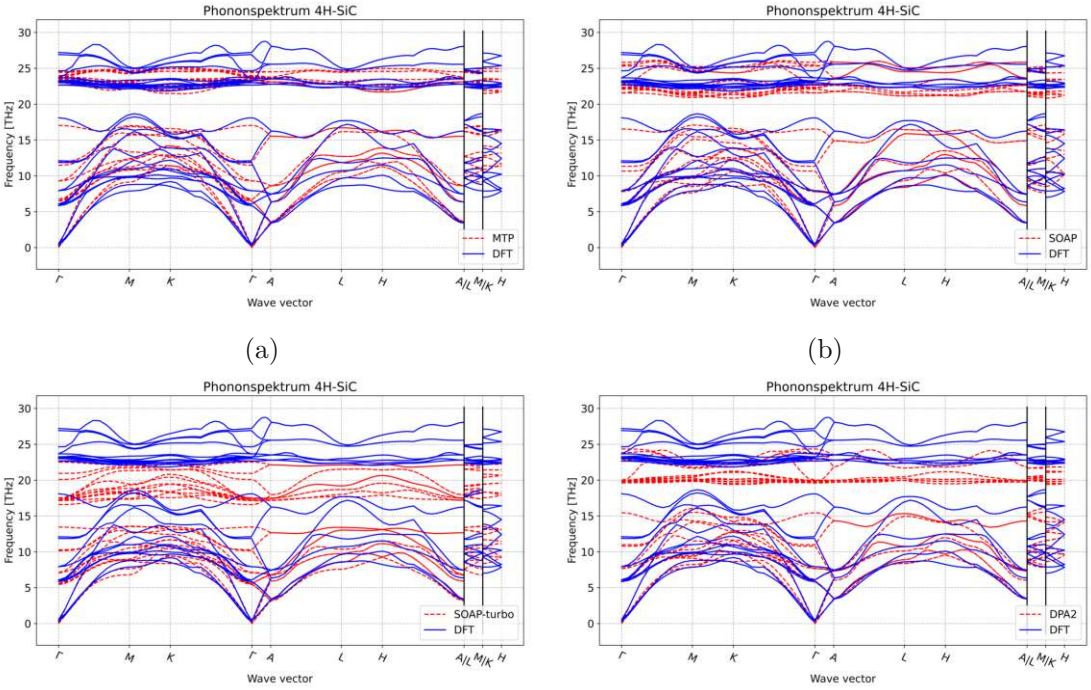

Figure 3.13: 4H-SiC phonon spectrum for (a) MTP level 20, (b) GAP with SOAP, (c) GAP with SOAP_turbo, and (d) DPA2

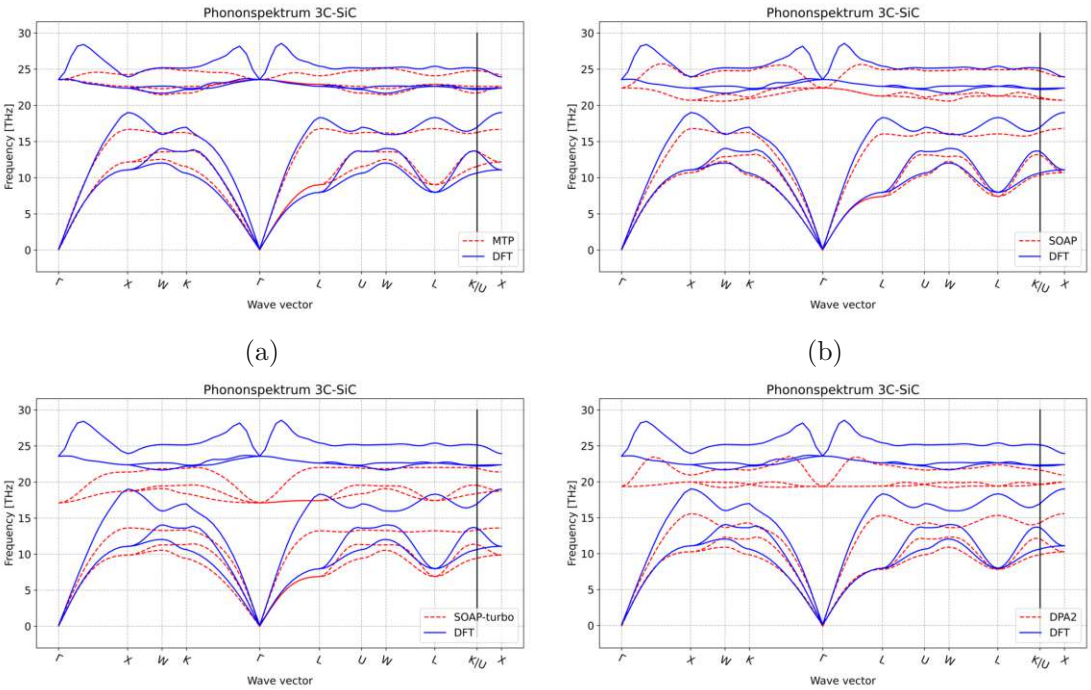

Figure 3.14: 3C-SiC phonon spectrum for (a) MTP level 20, (b) GAP with SOAP, (c) GAP with SOAP_turbo, and (d) DPA2

3.5 Amorphous Structures

During the implantation process, liquid pockets can be generated [94]. The subsequent recrystallization of these regions leads to the formation of point defects and amorphous clusters. To model this accurately, the melting temperature and the coordination of these amorphous structures must be correctly described [16] as they significantly influence the final structure after annealing. Experimental data suggest that in amorphous SiC, homonuclear C-C bonds tend to form sp^2 hybridizations. It is known that the GW fails to reproduce those bonds correctly [95].

In this work, amorphous structures were generated by heating up a cubic cell of 216 atoms to 6500 K. The system was equilibrated in the NVT ensemble at 6500 K for 20 ps followed by 20 ps in the NVE ensemble. The structure was then quenched to 300 K at a rate of $1 \cdot 10^{15}$ K/s and further equilibrated for 10 ps before evaluating the RDF in the NVE ensemble.

As shown in Figure 3.15 and Table 3.4, all ML-IAPs yield similar Si-C bond distances. However, the GW potential significantly overestimates the C-C nearest-neighbor distances. This is an important distinction, because the short-range C-C correlations are one of the key structural signatures of amorphous SiC and strongly influence whether the resulting network is physically realistic.

Bond	**MTP**	**SOAP**	**DPA2**	**GW**	**Experiment** [77]
C-C	1.5 Å	1.46 Å	1.5 Å	1.78 Å	1.51 Å
Si-C	1.9 Å	1.86 Å	1.86 Å	1.94 Å	1.88 Å
Si-Si	2.42 Å	2.42 Å	2.3 Å	2.5 Å	2.38 Å

Table 3.4: Comparison of the first peak for the bonding types C-C, Si-C, and Si-Si in amorphous SiC, obtained from melting-quench simulations

Notably, reducing the quench rate to $1 \cdot 10^{14}$ K/s resulted in phase segregation for all ML-IAPs. Those segregated structures were mainly attributed to the formation of carbon-graphite during the quench phase. Comparisons with DFT recalculations revealed that the ML-IAPs artificially predict these segregated structures to be energetically favorable. Previous MD studies have shown that these structures exist, but only within a narrow temperature range around 3000 K for pressures up to 1 GPa [17]. At lower temperatures, the 3C-SiC polytype is the most stable one. Due to a fixed cell volume in the NVT ensemble in the melting phase, pressures in the GPa range were achieved. Whether the formation of the segregated phases is due to insufficient sampling or represents a genuine physical effect due to the high pressures cannot be determined without further investigation. This discrepancy highlights the challenge of sampling the vast configurational space of different SiC phases. Consequently, a single iteration was not sufficient to generate a sufficiently diverse set of amorphous configurations. In contrast, the GW potential predicted these segregated structures to be unstable.

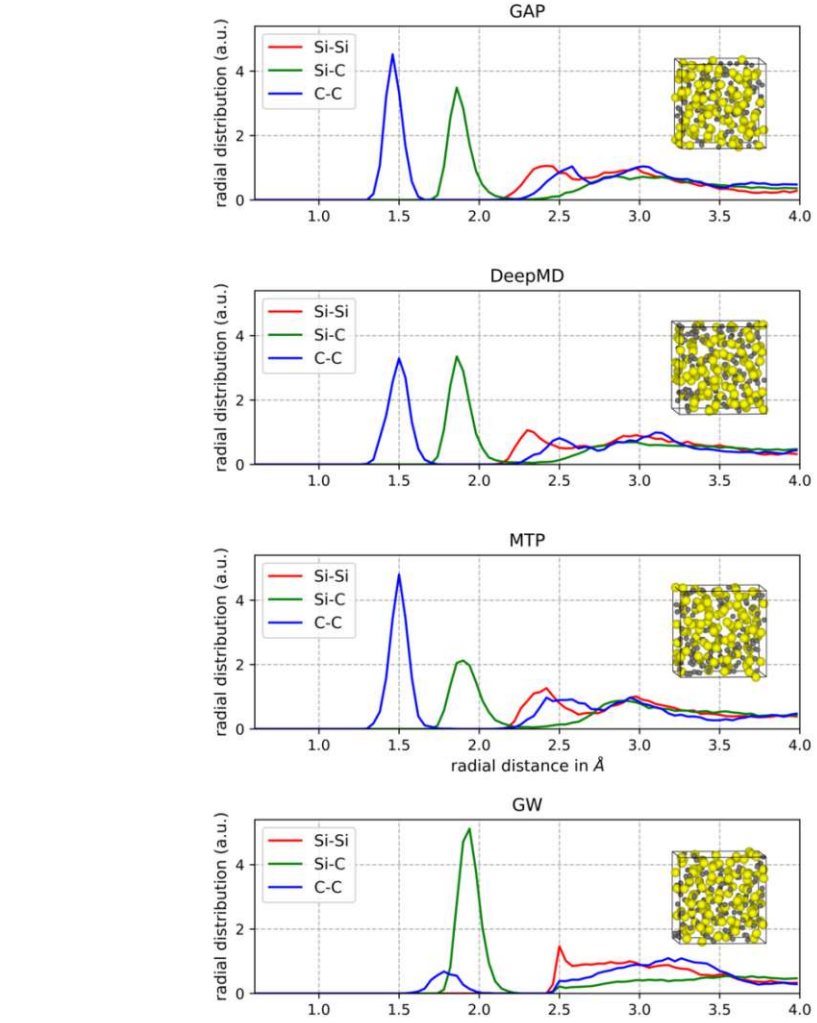

(a)

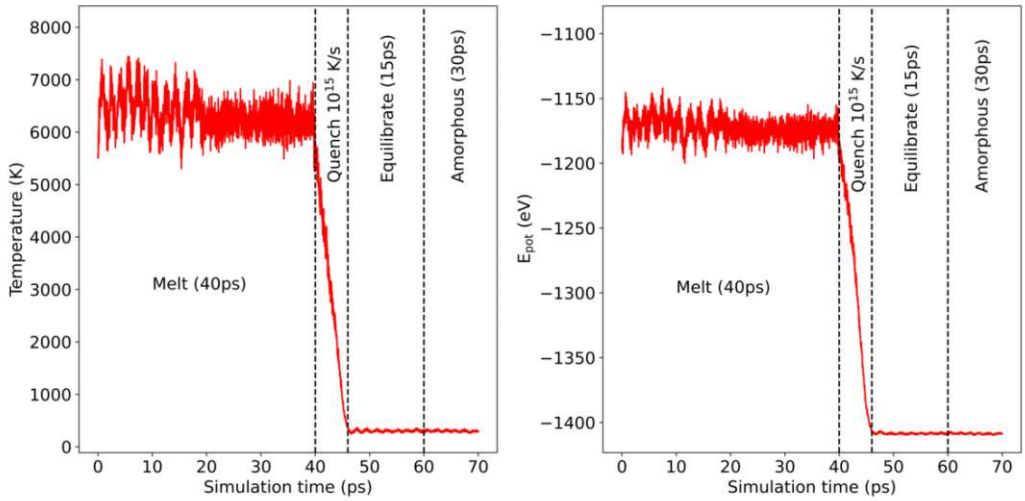

(b)

Figure 3.15: (a) Resulting RDFs for different force fields and (b) temperature and potential energy plotted over the simulation time.

3.6 Point defects

All investigated potentials exhibited qualitatively similar behavior across both static and dynamic benchmarks. However, training accurately on point defects remains a significant challenge, as typically only a single atom differs from the pristine crystal structure. Furthermore, the energy differences between distinct defect configurations are typically within the range of 1-3 eV, making it difficult to precisely predict the relative stability of each defect. For comparison with DFT references, various point-defect configurations in a 4H-SiC crystal containing 480 atoms were optimized using the BFGS optimizer in ASE, employing a force convergence criterion of 100 meV/Å. The same optimizer and convergence criteria were used to calculate the migration barriers within the ASE package. To ensure consistency, the same chemical potentials as in the DFT calculations were applied for the determination of formation energies.

3.6.1 Native point defects

In Figure 3.16, the relative formation energies for silicon interstitials are presented. As previously noted by Gao et al. [10], the most stable configuration for the GW is the Si_{TC}. MTP, SOAP, and GW all struggle to accurately represent the most stable neutral defect configuration. The superior performance of SOAP_turbo in this regard can be attributed to the higher weight assigned to defect structures during the training process. Notably, DPA2 yields the closest agreement with DFT values, implying that it is well-suited for modeling defect diffusion accurately.

In Appendix D the relative formation energy plots for carbon interstitials, antisites, and vacancies are provided. For carbon interstitials, all ML-IAPs exhibit trends comparable to DFT data. For all potentials, a carbon interstitial initially placed in either the hexagonal or cubic cage relaxed into a split-interstitial configuration or into a configuration with a formation energy approximately 2 eV higher, rendering the cage positions to be unstable.

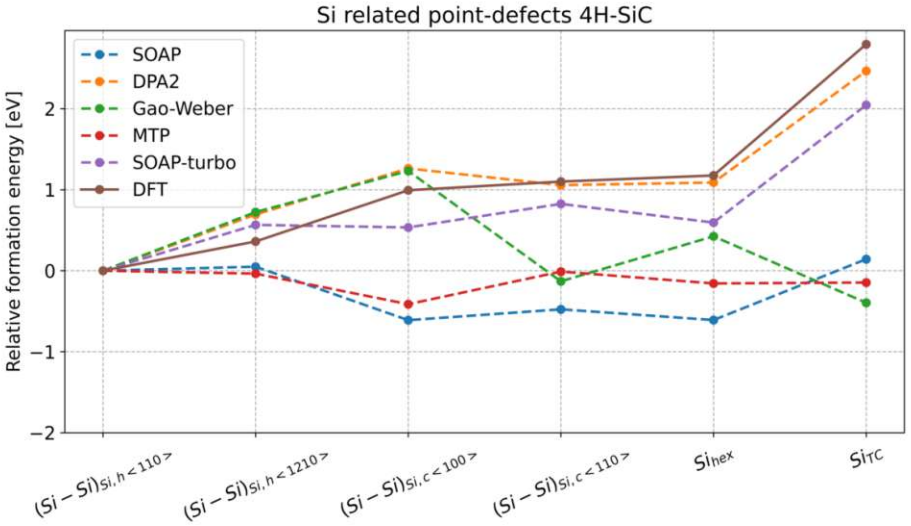

Figure 3.16: Relative formation energies of Si-related point defects for all tested ML-IAPs, compared with neutral-charge DFT simulations.

Our ML-IAPs are in good agreement with the DFT reference data. Only the MTP and SOAP models slightly overestimate the energy barrier. It is worth noting that the diffusion barrier in this work was calculated for a carbon vacancy in the basal plane at hexagonal lattice sites. In the literature, barriers of about 3.3 eV have been reported [96], which are somewhat lower than the barrier of 4.1 eV obtained in this study but still in reasonable agreement. Furthermore, the difference in energy between the initial and final positions of the barrier are caused by the convergence criterion of 100 meV/Å. Reducing this, results in configurations with the same energy.

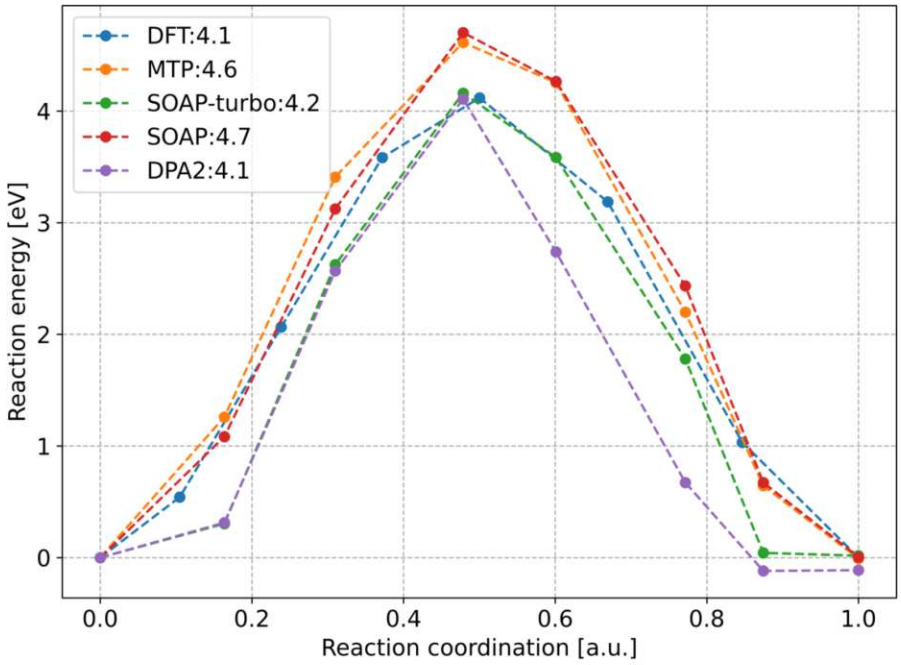

Figure 3.17: Migration barrier for next-nearest-neighbor jumps of $V_{\mathrm{C,hex}}$ within the hexagonal basal plane for different ML-IAPs, compared with DFT.

3.6.2 Al related defects

All ML-IAPs are able to reproduce the point-defect stability of Al-related defects as obtained from DFT, as shown in Figure 3.18. Overall, significantly fewer Al atoms than Si and C atoms are present in the system. Since ML-IAPs calculate the total energy as a sum of local atomic contributions, the configurational space for the local environment of Al atoms is much smaller than that of Si and C. Consequently, Al atoms naturally receive a higher effective fitting weight, simply due to the limited number of configurations available for training.

In Figure 3.19, the diffusion barrier of an Al interstitial is simulated from the distorted configuration to the meta-stable Al-Si split configuration, as shown by DFT in Figure 3.5. The MTP and SOAP models overestimate the diffusion barrier by more than 0.6 eV, which is caused by the wrong energies of the final state, whereas the SOAP_turbo model underestimates it by 0.4 eV. Only the DPA2 model reproduces the barrier with good accuracy. Due to the low absolute value of the diffusion barriers, even

these relatively small deviations lead to a significant change in the diffusion constant because of the exponential dependence in the Arrhenius relation.

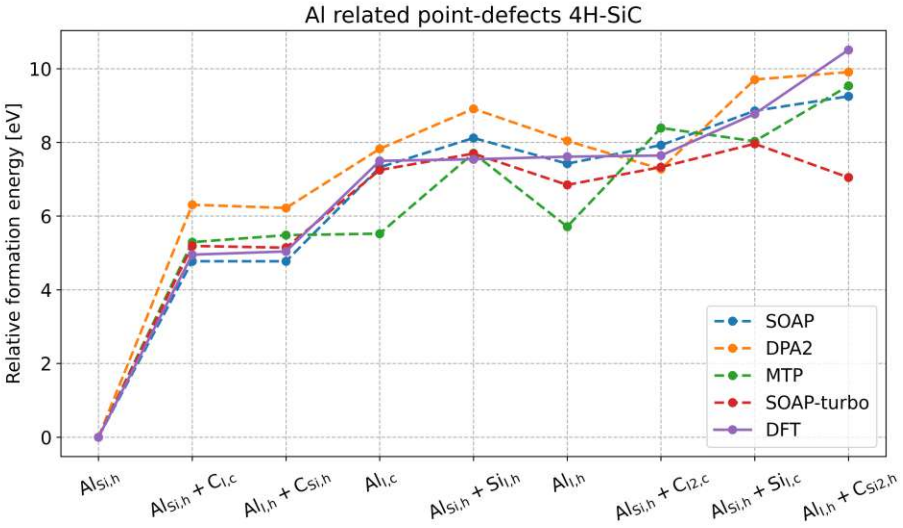

Figure 3.18: Relative formation energies of Al-related defects for all tested ML-IAPs, compared with neutral-charge DFT simulations.

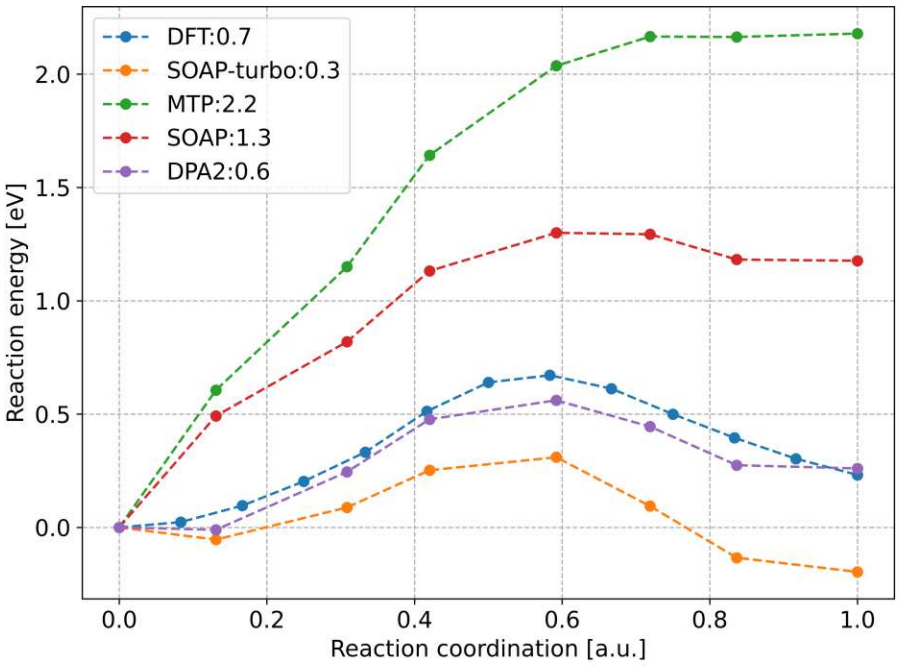

Figure 3.19: Migration barrier of Al_I in the cubic plane from the distorted configurations to the Al-Si split configuration.

3.7 Assessment of the ML-IAPs

Across the benchmarks presented in this chapter, the DPA2 model provides the most consistent overall agreement with the DFT reference data. It achieves the lowest fitting errors, reproduces the relative stability of Al-related defects well, and is the only tested ML-IAP that also captures the low neutral-state Al migration barrier with good accuracy. At the same time, it yields a realistic description of elastic properties, phonon spectra near the Γ-point, and the short-range structure of amorphous SiC. These results make DPA2 the strongest candidate for subsequent large-scale simulations of implantation damage and annealing.

The remaining models remain valuable, but for different reasons. The MTP offers the best cost-to-accuracy ratio on CPU hardware and therefore remains attractive for exploratory simulations and for large calculations where GPU memory is limited. SOAP and SOAP_turbo reproduce many qualitative trends, but their larger deviations for selected defect barriers and their higher computational cost make them less suitable as default production models in the present context. More broadly, the comparison shows that global fitting errors alone are not sufficient to judge the usefulness of an ML-IAP for implantation studies. The decisive quantities are the physically relevant observables, in particular defect stability ordering, amorphous bonding characteristics, and migration barriers of the Al-related processes that control activation and deactivation.

CHAPTER 4

Conclusions and Outlook

Within this thesis, the diffusion mechanism of Al in 4H-SiC was investigated for the neutral charge state. It was found that neutral Al interstitial diffusion has a migration barrier of 0.71 eV, which is significantly lower than the barrier reported for the +3 charge state of 2.87 eV. Due to defect states located close to the conduction band, this mechanism is expected to occur primarily in n-type SiC. Together with the calculated binding energies, these results indicate that incomplete Al activation cannot be attributed to a single trapping mechanism alone. In addition to carbon-related complexes, silicon interstitials can deactivate already substitutional Al, while antisite-related reactions may under suitable conditions contribute to activation.

Additionally, different ML-IAPs were trained for the ternary Al–Si–C system. The trained potentials were evaluated by comparing elastic constants, phonon spectra, RDFs of amorphous structures, and point-defect barriers against DFT results. Among the investigated models, DPA2 provides the most consistent overall agreement with DFT, in particular for the Al-related defect energetics and migration barriers that are most relevant for implantation and annealing studies.

The MTP appears to be a promising candidate for identifying general trends, such as the atomic structure of amorphous phases and phonon spectra, due to its fast computational performance on CPU hardware. However, it fails to accurately describe defect behavior and is therefore unsuitable for quantitative studies of diffusion mechanisms or for reliably identifying new defect types.

By employing SOAP_turbo in combination with trivial compression, faster training as well as faster MD simulations were achieved, making it a competitive alternative to the aforementioned MTP. Due to its Gaussian process foundation, it also provides a flexible framework in which physically motivated prior information can in principle be incorporated systematically.

When GPU resources are available, multi-task models such as DPA2 and DPA3 achieve computational speeds comparable to CPU-based ML-IAPs while yielding lower test errors. Due to its higher model complexity, the DPA2 model is able to reproduce all investigated properties at least qualitatively and gives the best overall agreement for the defect properties that matter most in the present work. Different DPA setups achieved very similar results, suggesting that the model still has the capacity to incorporate

additional training data and is therefore a promising candidate for further studies of Al defects in SiC. In contrast, the practical use of DPA3 is currently limited by its higher memory demand.

In this work, it was not possible to generate amorphous structures with quench rates slower than $1 \cdot 10^{15}$ K/s, because the stability of carbon phases such as graphite was overestimated. This is likely caused by an insufficiently sampled configuration space, which leads to high extrapolation errors for all ML-IAPs. Based on the present findings, several directions for future work can be identified to further improve the ML-IAPs and their application:

- Include surface reconstructions in the training data.
- Implement active-learning techniques into the training pipeline.
- Recalculate literature reference data for different phases.
- Repeat the iterative training procedure for generating amorphous structures using slower quench rates, and include segregated phases in the training data.
- Perform ion implantation simulations followed by subsequent annealing using the DPA2 potential.
- Identify new defect types from the simulations and investigate them using DFT.
- Extract binding energies and reaction rates and feed them into a kMC simulator.

By including different SiC phases, such as rocksalt structures, liquid silicon with graphite, and liquid silicon with diamond, the description of amorphous structures and their formation can be significantly improved. This is necessary to more realistically describe the state prior to the annealing after ion implantation. In this context, active learning would be particularly useful, because these different phases span a large configurational space and additional DFT calculations should ideally focus on the most extrapolative structures.

By using the developed DPA2 model in combination with an additive ZBL term, Al implantation followed by an annealing step can be simulated using MD. Even though the accessible simulation times are much shorter than those in experiments, it should still be possible to investigate whether Al is trapped in large clusters or whether it forms smaller complexes, and which deactivation pathways dominate immediately after implantation. Since previous studies have used a two-body Morse potential for the interaction of Al with the SiC crystal, the resulting complexes are likely to also occur in experiments.

Based on these complexes, a kMC model can be derived using the corresponding reaction rates and binding energies. Such a model would make it possible to simulate annealing on experimental time scales. In a full multiscale workflow, MD simulations would provide initial defect states for given implementation and annealing conditions, while the kMC model would evolve these states to predict the electrically active Al fraction after annealing. With this workflow, the process conditions could be tuned more systematically to enhance Al activation.

APPENDIX A

Tensor calculations

Tensors are generalizations of scalars, vectors, and matrices [97]. A tensor of rank is an element of $\mathbb{R}^{d_1 \times d_2 \ldots \times d_r}$. Consequently, a scalar is a tensor of rank zero, a vector of rank one, and a matrix of rank two. Two fundamental operations on tensors are the tensor product and the trace. The tensor product is defined in Equation (A.1).

$$[A \otimes B]_{i_1,i_2,\ldots,i_N,j_1,j_2,\ldots,j_M} = A_{i_1,i_2,\ldots,i_N} \cdot B_{j_1,j_2,\ldots,j_N} \tag{A.1}$$

The trace of a tensor requires that d_x and d_y have the same dimension. If this condition is satisfied, the trace of the tensor A can be calculated as defined in Equation (A.2).

$$[\mathrm{Tr}_{x,y}A]_{i_1,i_2,i_{x-1},i_{x+1},\ldots,i_N,j_1,j_2,j_{y-1},j_{y+1},\ldots,j_M} = \sum_{\alpha=1}^{d_x} A_{i_1,i_2,i_{x-1},\alpha,i_{x+1},\ldots,i_N,j_1,j_2,j_{y-1},\alpha,j_{y+1},\ldots,j_M} \tag{A.2}$$

The combination of tensor products and traces can be used to express inner products of vectors, as well as matrix–vector and matrix–matrix multiplications. These operations are performed by first applying a tensor product followed by a trace operation.

The definition of the scalar product is given in Equation (A.3), while the matrix–vector multiplication is shown in Equation (A.4). If the indices used in the trace operation for the matrix–vector product are changed, the resulting tensor of rank one also changes.

$$< \boldsymbol{a}, \boldsymbol{b} >= \sum_{\alpha} \boldsymbol{a}_\alpha \boldsymbol{b}_\alpha = \mathrm{Tr}_{11}(\boldsymbol{a} \otimes \boldsymbol{b}) \tag{A.3}$$

$$\boldsymbol{y}_i = [\boldsymbol{M}\boldsymbol{x}]_i = \sum_{\alpha} M_{i\alpha} x_\alpha = \mathrm{Tr}_{21}(\boldsymbol{M} \otimes \boldsymbol{x}) \tag{A.4}$$

The Frobenius inner product shown in Equation (A.5) is defined as the trace of the matrix product. The matrix multiplication itself can be expressed using a tensor product followed by a contraction, as shown in Equation (A.6).

$$\boldsymbol{A} : \boldsymbol{B} =< \boldsymbol{A}, \boldsymbol{B} >_{\mathrm{F}} = \sum_{i,j} A_{ij} B_{ij} = \sum_{j} \sum_{i} A_{ji} B_{ij} = \mathrm{Tr}_{11}(\boldsymbol{A}^{\mathrm{T}} \boldsymbol{B}) \tag{A.5}$$

$$\boldsymbol{C}_{ij} = [\boldsymbol{AB}]_{ij} = \sum_{\alpha} A_{i\alpha} B_{\alpha j} = \mathrm{Tr}_{21}(\boldsymbol{A} \otimes \boldsymbol{B}) \tag{A.6}$$

APPENDIX B

Aluminium diffusion

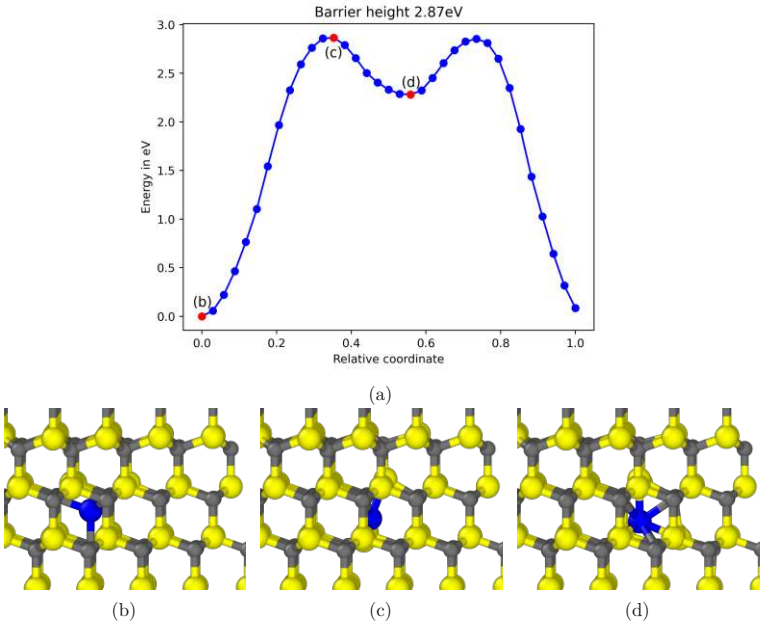

Figure B.1: Migration barrier of Al_I in the cubic plane in the +3 charge state. (a) Migration barrier, (b) $Al_{I,c}$ configuration, (c) saddle point, and (d) an meta stable configuration.

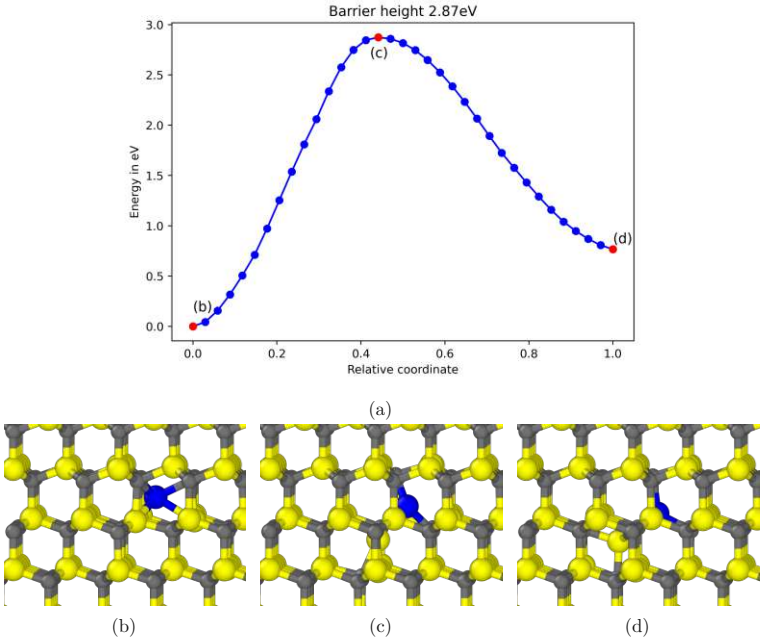

Figure B.2: Kick-in mechanism of $Al_{I,h}$ in the +3 charge state. (a) Migration barrier, (b) $Al_{I,h}$ configuration, (c) saddle point, and (d) end position $Al_{Si,h} + Si_{I,c}$

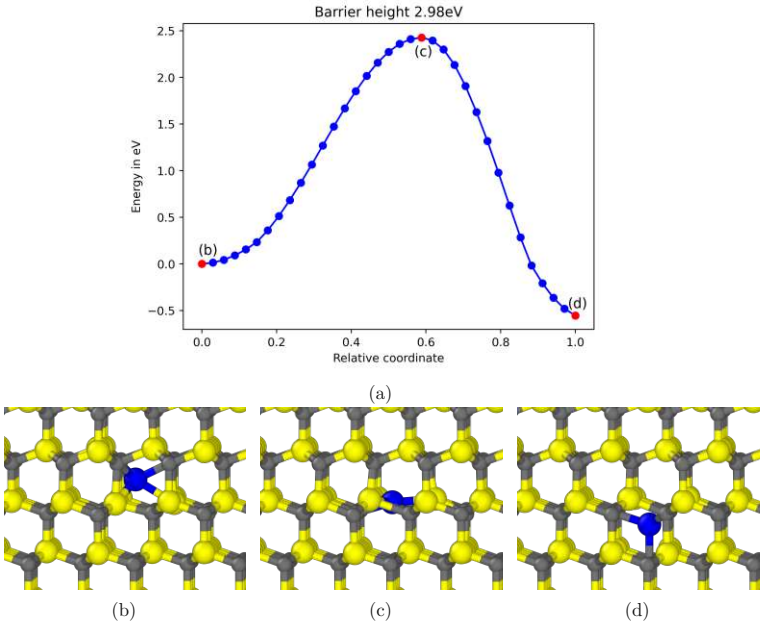

Figure B.3: Out of plane diffusion of Al_I in the +3 charge state. (a) Migration barrier, (b) $Al_{I,h}$ configuration, (c) saddle point, and (d) $Al_{I,c}$.

APPENDIX C

ML-IAP training

C.1 MTP training

```
mpirun -n 64 path_to_mlip_3/mlp train 20.almtp train_full.cfg  \
--energy_weight=4.772 --force_weight=0.1600   --weight_scaling=1 \
--weight_scaling_forces=1 --stress_weight=0.001   \
--iteration_limit=10000 --save_to=curr_$level.almtp
```

C.2 GAP training

```
export OMP_NUM_THREADS=40
path_to_gap/gap_fit \
energy_parameter_name=energy force_parameter_name=force \
at_file=train.xyz default_sigma={0.0168 0.514 0.0 0.0} \
gap={
distance_2b \
cutoff=5.0 \
n_sparse=40 \
cutoff_transition_width=1.0 \
covariance_type=ard_se \
delta=10.0 theta_uniform=1.0  \
sparse_method=uniform \
: \
soap atom_sigma=0.71 \
l_max=4 \
n_max=6 \
cutoff=3.63 \
cutoff_transition_width=1.0 \
delta=1.0 \
radial_scaling=-1.92 \
covariance_type=dot_product \
n_sparse=4000 \
zeta=4 \
sparse_method=cur_points \
} \
```

```
config_type_sigma={\
dimer:0.0008:0.04:0.0:0.0:\
single:0.0001:0.04:0.0:0.0:\
perfect_crystall:0.0008:0.04:0.0:0.0\
} \
gp_file=gap.xml \
sparse_jitter=1e-8
```

Listing C.1: SOAP training

```
export OMP_NUM_THREADS=40
path_to_gap/gap_fit energy_parameter_name=energy \
force_parameter_name=force  at_file=train.xyz \
default_sigma={0.0168 0.514 0.0 0.0} \
gap="{ \
distance_2b \
cutoff=4.5 \
n_sparse=100 \
cutoff_transition_width=1.0 \
covariance_type=ard_se \
delta=10.0 \
theta_uniform=1.0  \
sparse_method=uniform \
: \
soap_turbo \
l_max=4 \
alpha_max={{6 6 6}} \
atom_sigma_r={{0.71 0.71 0.71}} \
atom_sigma_t={{0.71 0.71 0.71}} \
atom_sigma_r_scaling={{0.0 0.0 0.0}} \
atom_sigma_t_scaling={{0.0 0.0 0.0}} \
zeta=4 \
rcut_hard=3.63 \
rcut_soft=2.5 \
basis=poly3gauss \
scaling_mode=polynomial \
amplitude_scaling={{1.0 1.0 1.0}} \
n_species=3 species_Z={{14 6 13}} \
central_index=1 \
radial_enhancement=1 \
central_weight={{1.0 1.0 1.0}} \
n_sparse=1000 \
delta=0.1 \
f0=0.0 \
covariance_type=dot_product \
sparse_method=cur_points \
add_species=F \
compress_mode=trivial  \
:
soap_turbo \
l_max=4 \
alpha_max={{6 6 6}} \
atom_sigma_r={{0.71 0.71 0.71}} \
atom_sigma_t={{0.71 0.71 0.71}} \
atom_sigma_r_scaling={{0.0 0.0 0.0}} \
atom_sigma_t_scaling={{0.0 0.0 0.0}} \
zeta=4 \
rcut_hard=3.63 \
```

```
rcut_soft=2.5 \
basis=poly3gauss \
scaling_mode=polynomial \
amplitude_scaling={{1.0 1.0 1.0}} \
n_species=3 species_Z={{14 6 13}} \
central_index=2 \
radial_enhancement=1 \
central_weight={{1.0 1.0 1.0}} \
n_sparse=1000 \
delta=0.1 \
f0=0.0 \
covariance_type=dot_product \
sparse_method=cur_points \
add_species=F \
compress_mode=trivial \
: \
soap_turbo \
l_max=4 alpha_max={{6 6 6}} \
atom_sigma_r={{0.71 0.71 0.71}} \
atom_sigma_t={{0.71 0.71 0.71}} \
atom_sigma_r_scaling={{0.0 0.0 0.0}} \
atom_sigma_t_scaling={{0.0 0.0 0.0}} \
zeta=4 \
rcut_hard=3.63 \
rcut_soft=2.5 \
basis=poly3gauss \
scaling_mode=polynomial \
amplitude_scaling={{1.0 1.0 1.0}} \
n_species=3 species_Z={{14 6 13}} \
central_index=3 \
radial_enhancement=1 \
central_weight={{1.0 1.0 1.0}} \
n_sparse=1000 \
delta=0.1 \
f0=0.0 \
covariance_type=dot_product \
sparse_method=cur_points \
add_species=F \
compress_mode=trivial }" \

config_type_sigma={\
single:0.0001:0.005:0.0:0.0:\
perfect_crystall:0.0004:0.01:0.0:0.0:\
Al_defects:0.0004:0.01:0.0:0.0:\
Si_interstitials:0.0004:0.01:0.0:0.0:\
vacancies:0.0004:0.01:0.0:0.0:\
C_interstitials:0.0004:0.01:0.0:0.0} \
sparse_jitter=1e-8 \
gp_file=gap.xml
```

Listing C.2: SOAP-turbo training

C.3 DeepMD training

```
export CUDA_VISIBLE_DEVICES=0,1
torchrun --nproc_per_node=2 --no-python dp --pt train input.json
```

Listing C.3: DeepMD training with two GPUs

```
#descriptor definition
"dpa2_descriptor": {
     "type": "dpa2",
     "repinit": {
       "tebd_dim": 8,
       "rcut": 4.01,
       "rcut_smth": 0.5,
       "nsel": 120,
       "neuron": [
         25,
         40,
         40
       ],
       "axis_neuron": 12,
       "activation_function": "tanh",
       "three_body_sel": 48,
       "three_body_rcut": 4.0,
       "three_body_rcut_smth": 3.5,
       "use_three_body": true
     },
     "repformer": {
       "rcut": 4.0,
       "rcut_smth": 3.5,
       "nsel": 48,
       "nlayers": 6,
       "g1_dim": 128,
       "g2_dim": 32,
       "attn2_hidden": 32,
       "attn2_nhead": 4,
       "attn1_hidden": 128,
       "attn1_nhead": 4,
       "axis_neuron": 4,
       "update_h2": false,
       "update_g1_has_conv": true,
       "update_g1_has_grrg": true,
       "update_g1_has_drrd": true,
       "update_g1_has_attn": false,
       "update_g2_has_g1g1": false,
       "update_g2_has_attn": true,
       "update_style": "res_residual",
       "update_residual": 0.01,
       "update_residual_init": "norm",
       "attn2_has_gate": true,
       "use_sqrt_nnei": true,
       "g1_out_conv": true,
       "g1_out_mlp": true
     },
     "precision": "float64",
     "add_tebd_to_repinit_out": false
   },
```

```
51
52      #fitting net
53       "Domains_AlSiC": {
54                  "type_map": "type_map_all",
55                  "descriptor": "dpa2_descriptor",
56                  "fitting_net": {
57                      "neuron": [
58                          180,
59                          180,
60                          180
61                      ],
62                            "precision": "float64",
63                      "resnet_dt": true,
64                      "seed": 1,
65                      "_comment": " that's all"
66                  }
67        }
68
69        #learning rate
70        "learning_rate": {
71          "type": "exp",
72          "decay_steps": 5000,
73          "start_lr": 0.001,
74          "stop_lr": 3.51e-08,
75          "_comment": "that's all"
76        },
77
78
79        #loss function
80         "Domains_AlSiC": {
81              "type": "ener",
82             "start_pref_e": 0.2,
83              "limit_pref_e": 1,
84              "start_pref_f": 50,
85              "limit_pref_f": 1,
86              "start_pref_v": 1,
87              "limit_pref_v": 0.04
88           }
89
90         #multi-task probablities
91         "model_prob": {
92            "Domains_Semic": 1.0,
93            "Domains_MPTrj": 1.0,
94            "Transition1x": 1.0,
95           "Domains_AlSiC":6.0
96          }
97
98
99          #training and validation data
100          "Domains_AlSiC": {
101             "training_data": {
102                 "systems":          [....],
103                 "batch_size": "auto",
104                 "_comment": "that's all"
105             },
106             "validation_data": {
107                 "systems":          [....],
```

```
                "batch_size": "auto",
                "_comment": "that's all"
            }
        }


    #training length
    "numb_steps": 2000000,
    "warmup_steps": 0,
    "gradient_max_norm": 5.0,
    "seed": 10,
    "disp_file": "lcurve.out",
    "disp_freq": 100,
    "save_freq": 2000,
    "_comment": "that's all"
```

Listing C.4: Configuration file snapshots (input.json) for DPA2 multi-task training

For all potentials shown, only the descriptor hyperparameters and the type of the fitting network are changed.

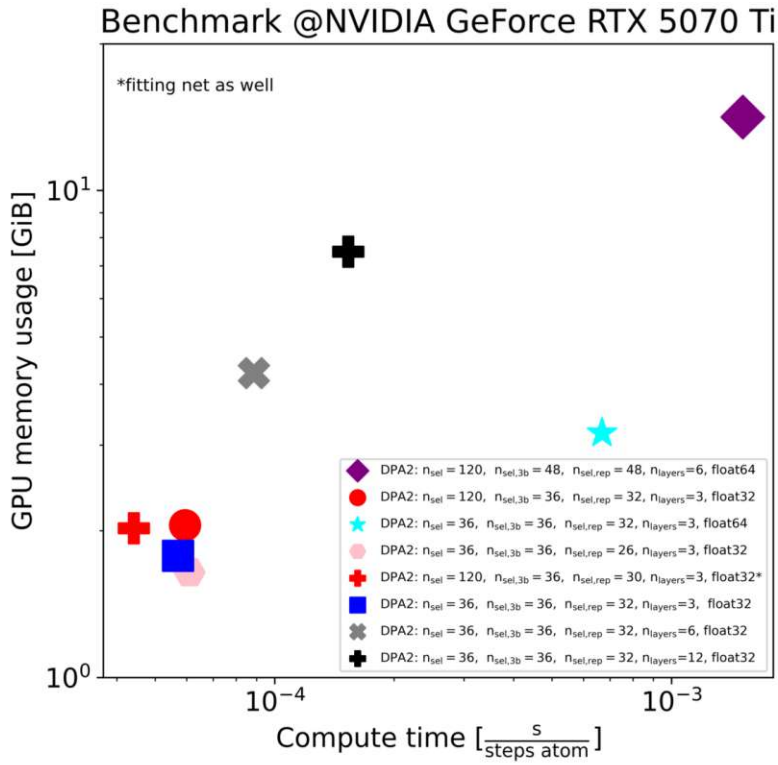

Figure C.1: Benchmarking of the DPA2 setup containing 1728 atoms. Float32 denotes single precision used only for the descriptor, while float32* indicates single precision used for both the descriptor and the fitting network.

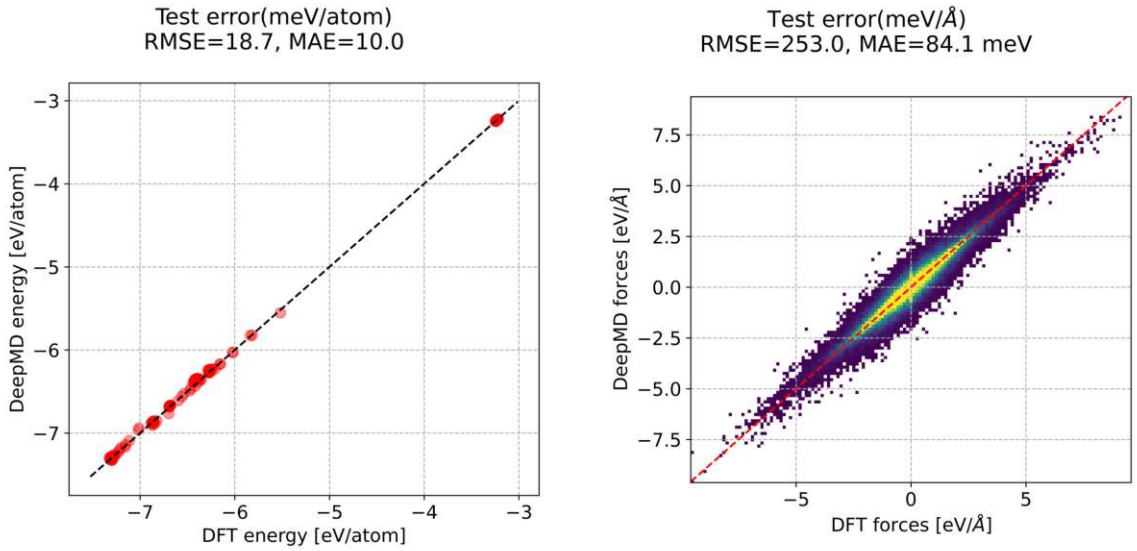

(a) (b)

Figure C.2: (a) Energy test error and (b) force test error for DPA2: $n_{sel} = 120$, $n_{sel,3b} = 36$, $n_{sel,rep} = 32$, n_{layers}=3, float32

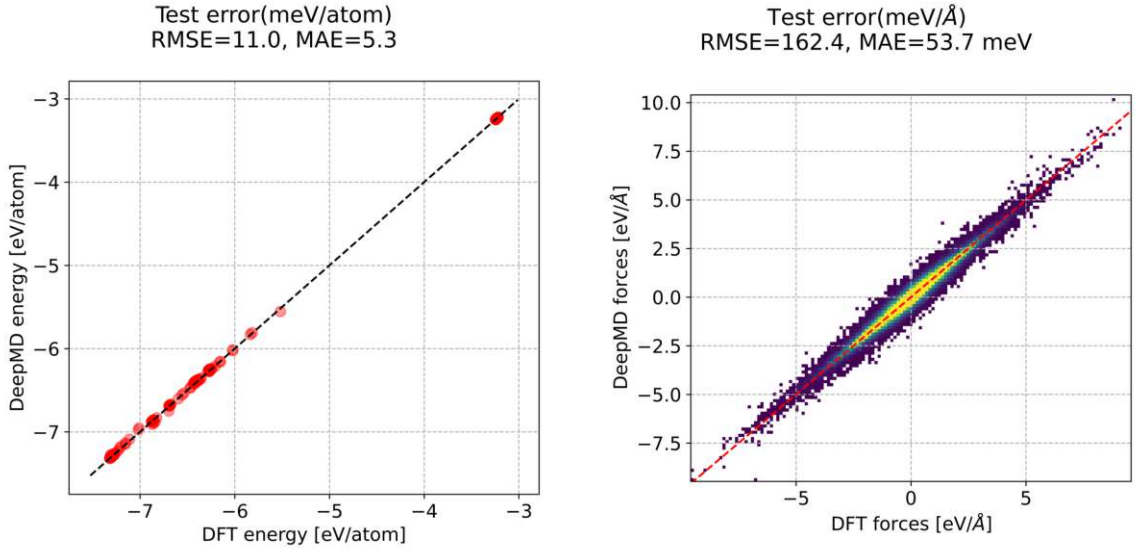

(a) (b)

Figure C.3: (a) Energy test error and (b) force test error for DPA2: $n_{sel} = 36$, $n_{sel,3b} = 36$, $n_{sel,rep} = 32$, n_{layers}=6, float32

APPENDIX D

Additional ML-IAP results

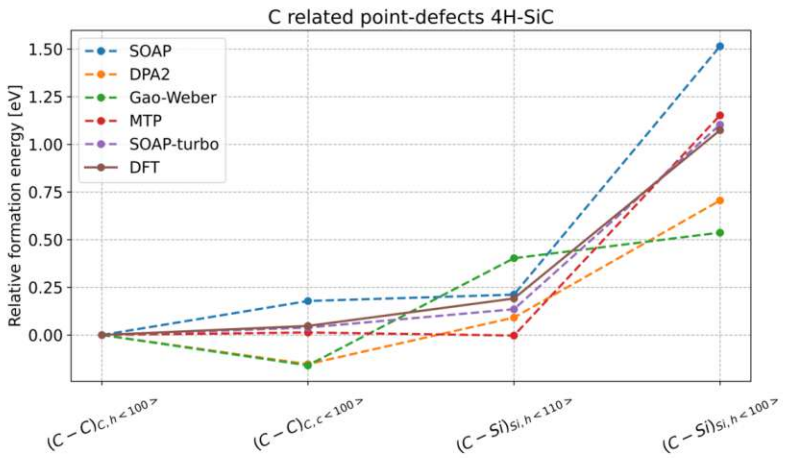

Figure D.1: Relative formation energies of C-related point defects for all tested ML-IAPs, compared with neutral-charge DFT simulations. Carbon cage configurations that relaxed into split configurations or resulted in formation energies approximately 2 eV higher were excluded.

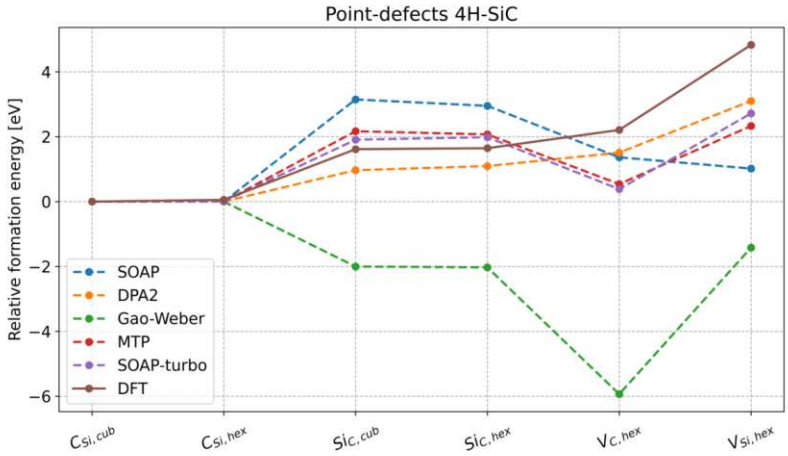

Figure D.2: Relative formation energies of vacancies and antisites defects for all tested ML-IAPs, compared with neutral-charge DFT simulations.

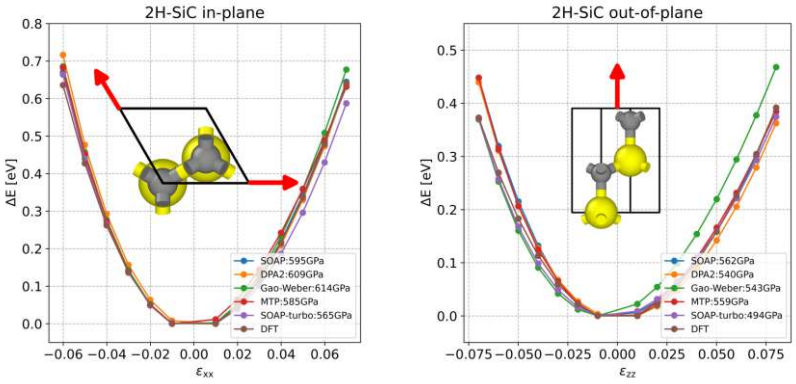

(a) (b)

Figure D.3: PES of 2H-SiC under applied strain up to $\epsilon = \pm 0.08$ (a) biaxial along the $[\bar{1}2\bar{1}0]$ and $[\bar{1}\bar{1}20]$ directions, and (b) along the [0001] direction.

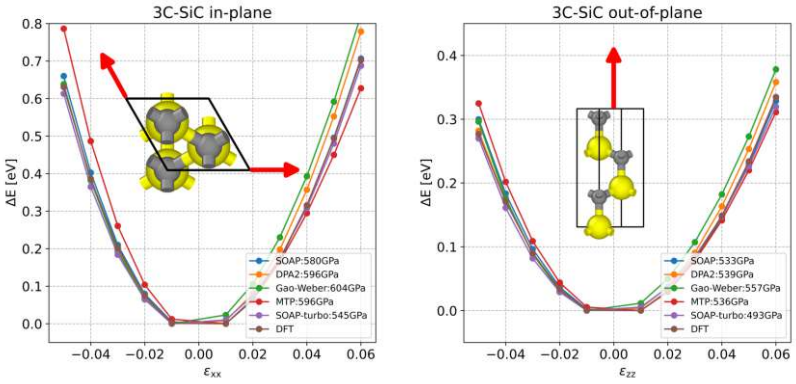

(a) (b)

Figure D.4: PES of 3C-SiC under applied strain up to $\epsilon = \pm 0.08$ (a) biaxial along the $[\bar{1}2\bar{1}0]$ and $[\bar{1}\bar{1}20]$ directions, and (b) along the [0001] direction.

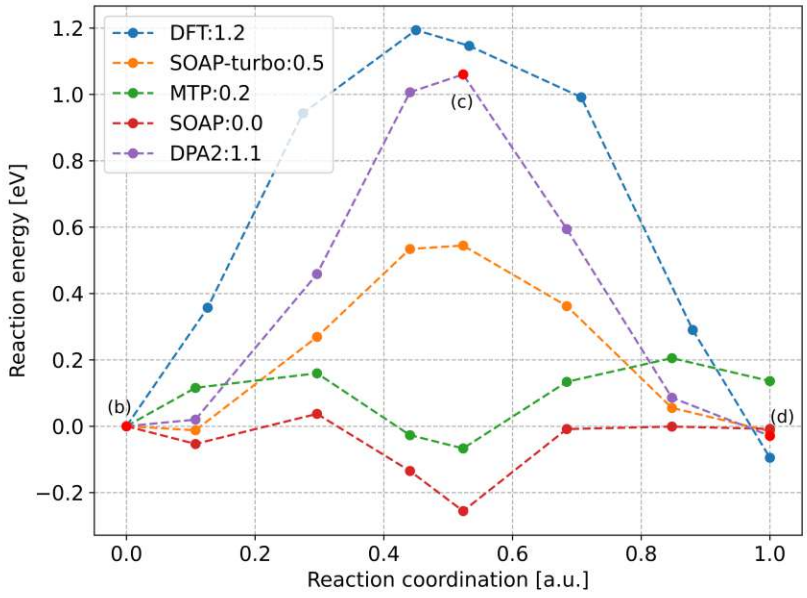

(a)

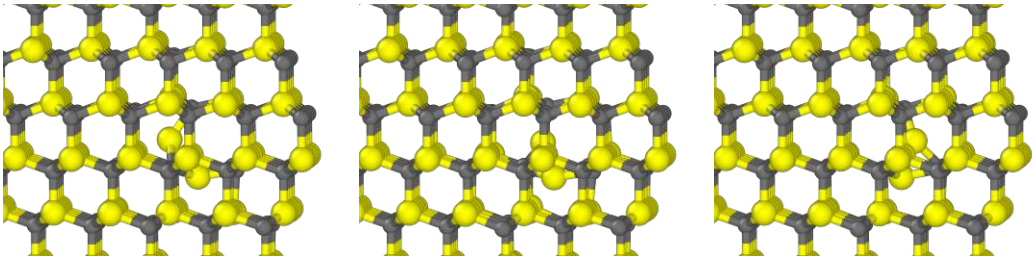

(b) (c) (d)

Figure D.5: Rotation of a Si-$Si_{Si,h<100>}$ configuration in the hexagonal plane of 4H-SiC with (a) the migration barrier, (b) initial Si-$Si_{Si,h<100>}$ configuration, (c) the saddle point, and (d) being the rotated Si-$Si_{Si,h<100>}$. For the SOAP and MTP the local minima correspond to the Si_{hex} and Si_{TC} respectively, being the global Si interstitial minima configurations.

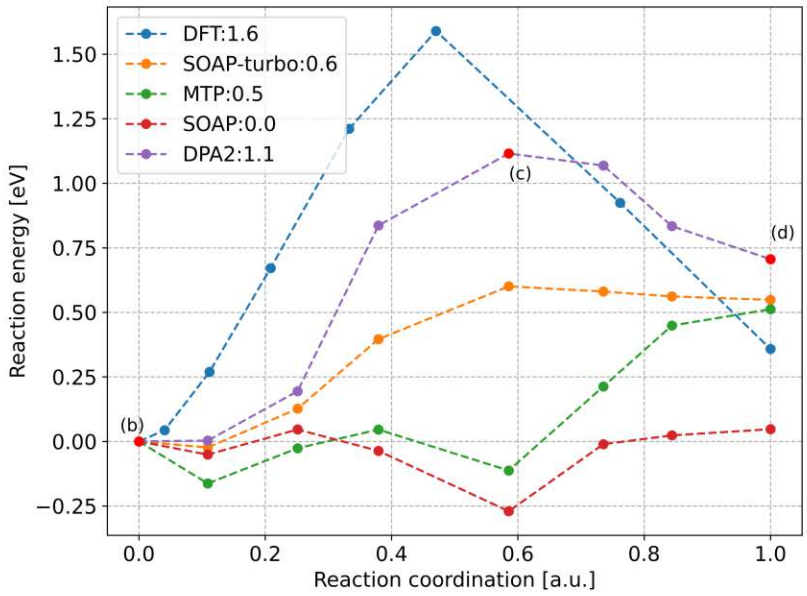

(a)

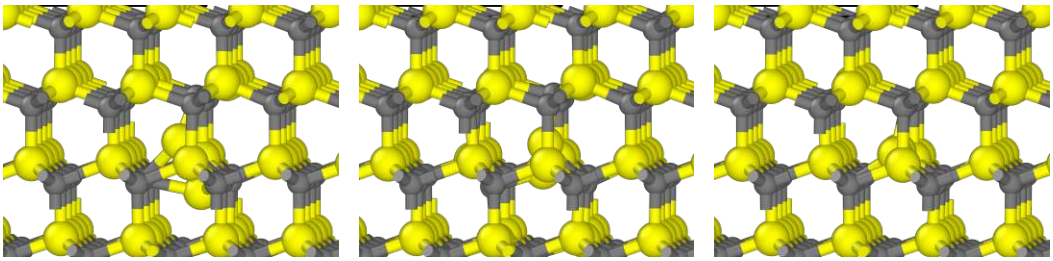

(b) (c) (d)

Figure D.6: Transition from the Si-Si$_{\text{Si,h<100>}}$ to the Si-Si$_{\text{Si,h<}\bar{1}2\bar{1}0>}$ in the hexagonal plane in a 4H-SiC with (a) the migration barrier, (b) the Si-Si$_{\text{Si,h<100>}}$, (c) the saddle point, and (d) being the transformed Si-Si$_{\text{Si,h<}\bar{1}2\bar{1}0>}$.

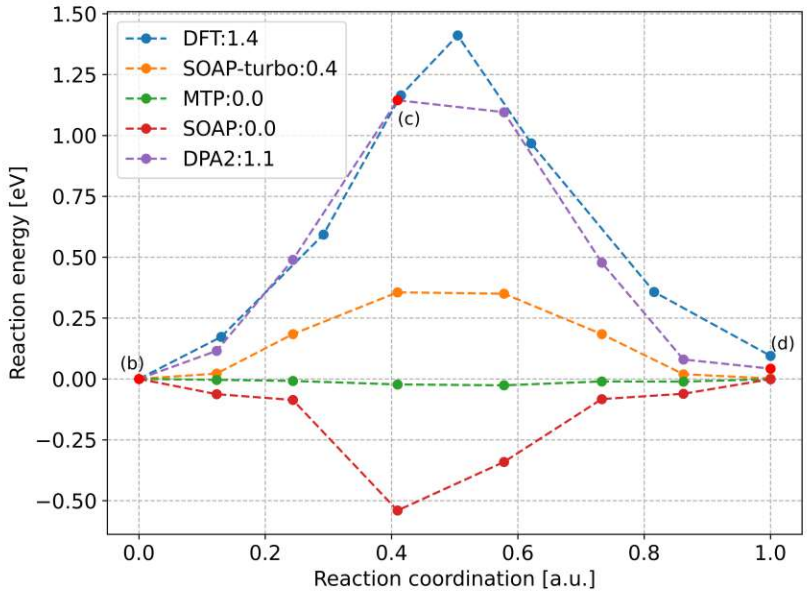

(a)

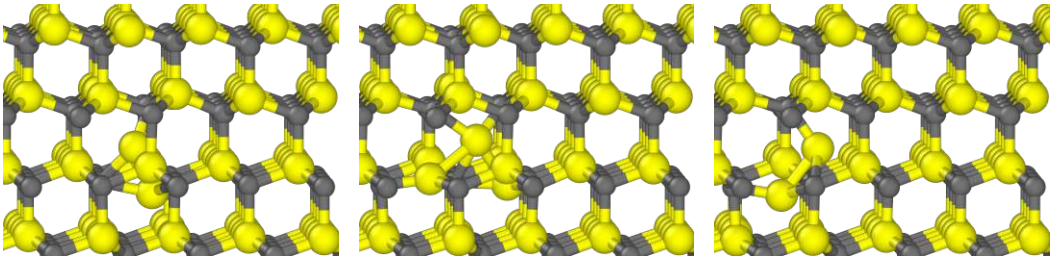

(b) (c) (d)

Figure D.7: Cage hopping of Si-$Si_{Si,h<100>}$ in the hexagonal plane in a 4H-SiC with (a) the migration barrier, (b) the Si-$Si_{Si,h<100>}$, (c) the saddle point, and (d) being the translated Si-$Si_{Si,h<100>}$. The DFT barrier is in close agreement with the literature value of 1.54 eV [12].

Bibliography

[1] J. Baliga, "Semiconductors for High-Voltage, Vertical Channel Field-Effect Transistors", *Journal of applied Physics*, vol. 53, no. 3, pp. 1759–1764, 1982. DOI: 10.1063/1.331646.

[2] J. Millan, P. Godignon, X. Perpiñà, A. Pérez-Tomás, and J. Rebollo, "A Survey of Wide Bandgap Power Semiconductor Devices", *IEEE transactions on Power Electronics*, vol. 29, no. 5, pp. 2155–2163, 2013. DOI: 10.1109/TPEL.2013.2268900.

[3] T. Ayalew, "SiC Semiconductor Devices Technology, Modeling and Simulation", Ph.D. dissertation, Technische Universität Wien, 2004. DOI: 10.34726/hss.2004.04281063.

[4] V. Šimonka, "Thermal Oxidation and Dopant Activation of Silicon Carbide", Ph.D. dissertation, Technische Universität Wien, 2018. DOI: 10.34726/hss.2018.60302.

[5] K. Woo et al., "From Wide to Ultrawide-Bandgap Semiconductors for High Power and High Frequency Electronic Devices", *Journal of Physics: Materials*, vol. 7, no. 2, p. 022 003, 2024. DOI: 10.1088/2515-7639/ad218b.

[6] Á. Gali, T. Hornos, N. T. Son, E. Janzén, and W. J. Choyke, "Ab Initio Supercell Calculations on Aluminum-Related Defects in SiC", *Physical Review B—Condensed Matter and Materials Physics*, vol. 75, no. 4, p. 045 211, 2007. DOI: 10.1103/PhysRevB.75.045211.

[7] P. Kumar, M. I. M. Martins, M. E. Bathen, T. Prokscha, and U. Grossner, "Al-Implantation Induced Damage in 4H-SiC", *Materials Science in Semiconductor Processing*, vol. 174, p. 108 241, 2024. DOI: 10.1016/j.mssp.2024.108241.

[8] S.-I. Satake, N. Inoue, T. Kunugi, M. Shibahara, and H. Kasahara, "Large-Scale Molecular Dynamics Simulation for Two Ar Clusters Impact on 4H–SiC", *Nuclear Instruments and Methods in Physics Research Section B: Beam Interactions with Materials and Atoms*, vol. 257, no. 1-2, pp. 639–644, 2007. DOI: 10.1016/j.nimb.2007.01.055.

[9] F. Gao and W. J. Weber, "Empirical Potential Approach for Defect Properties in 3C-SiC", *Nuclear Instruments and Methods in Physics Research Section B: Beam Interactions with Materials and Atoms*, vol. 191, no. 1-4, pp. 504–508, 2002. DOI: 10.1016/S0168-583X(02)00600-6.

[10] F. Gao, W. J. Weber, M. Posselt, and V. Belko, "Atomistic Study of Intrinsic Defect Migration in 3C-SiC", *Physical Review B—Condensed Matter and Materials Physics*, vol. 69, no. 24, p. 245 205, 2004. DOI: 10.1103/PhysRevB.69.245205.

[11] M. Bockstedte, A. Mattausch, and O. Pankratov, "Ab Initio Study of the Migration of Intrinsic Defects in 3C-SiC", *Physical Review B*, vol. 68, no. 20, p. 205 201, 2003. DOI: 10.1103/PhysRevB.68.205201.

[12] J. Coutinho, "Theory of the Thermal Stability of Silicon Vacancies and Interstitials in 4H-SiC", *Crystals*, vol. 11, no. 2, p. 167, 2021. DOI: 10.3390/cryst11020167.

[13] M. A. Caro and contributors, *Soap_Turbo: Turbo SOAP Descriptor Library*, https://github.com/libAtoms/soap_turbo, Accessed: 2026-03-08, 2021.

[14] T. Liao, G. Roma, and J. Wang, "Neutral Silicon Interstitials in Silicon Carbide: A First Principles Study", *Philosophical Magazine*, vol. 89, no. 26, pp. 2271–2284, 2009. DOI: 10.1080/14786430903055184.

[15] C. R. Dandekar and Y. C. Shin, "Molecular Dynamics Based Cohesive Zone Law for Describing Al–SiC Interface Mechanics", *Composites Part A: Applied Science and Manufacturing*, vol. 42, no. 4, pp. 355–363, 2011. DOI: 10.1016/j.compositesa.2010.12.005.

[16] A. Hamedani and A. E. Sand, "SiC-TGAP: A Machine Learning Interatomic Potential for Radiation Damage Simulations in 3C-SiC", *arXiv*, 2025. DOI: 10.48550/arXiv.2510.06966.

[17] J. Wu et al., "An Accurate and Efficient Machine-Learned Potential for SiC from Ambient to Extreme Environments", *arXiv*, 2025. DOI: 10.48550/arXiv.2510.01827.

[18] Y. Du et al., "Construction of a Neural Network Potential for SiC and Its Application in Uniaxial Tension Simulations", *Computational Materials Science*, vol. 242, p. 113 078, 2024. DOI: 10.1016/j.commatsci.2024.113078.

[19] B. Fu et al., "Determining the Thermal Conductivity and Phonon Behavior of SiC Materials with Quantum Accuracy via Deep Learning Interatomic Potential Model", *Journal of Nuclear Materials*, vol. 591, p. 154 897, 2024. DOI: 10.1016/j.jnucmat.2024.154897.

[20] S. Leroch, R. Stella, A. Hössinger, and L. Filipovic, "Molecular Dynamics Study of Al Implantation in 4H-SiC", in Proc. of the 2023 International Conference on Simulation of Semiconductor Processes and Devices (SISPAD), IEEE, 2023, pp. 185–188. DOI: 10.23919/SISPAD57422.2023.10319554.

[21] S. Leroch, R. Stella, A. Hössinger, and L. Filipovic, "MD Simulation of Epitaxial Recrystallization and Defect Structure of Al-Implanted 4H-SiC", in Proc. of the 2024 International Conference on Simulation of Semiconductor Processes and Devices (SISPAD), IEEE, 2024, pp. 1–4. DOI: 10.1109/SISPAD62626.2024.10733052.

[22] P. Hohenberg and W. Kohn, "Inhomogeneous Electron Gas", *Physical review*, vol. 136, no. 3B, B864, 1964. DOI: 10.1103/PhysRev.136.B864.

[23] W. Kohn and L. J. Sham, "Self-Consistent Equations Including Exchange and Correlation Effects", *Physical review*, vol. 140, no. 4A, A1133, 1965. DOI: 10.1103/PhysRev.140.A1133.

[24] D. R. Hartree, "The Wave Mechanics of an Atom with a Non-Coulomb Central Field. Part I. Theory and Methods", *Mathematical Proceedings of the Cambridge Philosophical Society*, vol. 24, no. 1, pp. 89–110, 1928. DOI: 10.1017/S0305004100011919.

[25] J. P. Perdew, K. Burke, and M. Ernzerhof, "Generalized Gradient Approximation Made Simple", *Physical review letters*, vol. 77, no. 18, p. 3865, 1996. DOI: 10.1103/PhysRevLett.77.3865.

[26] J. Heyd, G. E. Scuseria, and M. Ernzerhof, "Hybrid Functionals Based on a Screened Coulomb Potential", *The Journal of chemical physics*, vol. 118, no. 18, pp. 8207–8215, 2003. DOI: 10.1063/1.1564060.

[27] T. D. Kühne et al., "CP2K: An Electronic Structure and Molecular Dynamics Software Package-Quickstep: Efficient and Accurate Electronic Structure Calculations", *The Journal of Chemical Physics*, vol. 152, no. 19, 2020. DOI: 10.1063/5.0007045.

[28] J. VandeVondele and J. Hutter, "Gaussian Basis Sets for Accurate Calculations on Molecular Systems in Gas and Condensed Phases", *The Journal of chemical physics*, vol. 127, no. 11, p. 114105, 2007. DOI: 10.1063/1.2770708.

[29] S. Goedecker, M. Teter, and J. Hutter, "Separable Dual-Space Gaussian Pseudopotentials", *Physical Review B*, vol. 54, no. 3, p. 1703, 1996. DOI: 10.1103/PhysRevB.54.1703.

[30] T. P. Senftle et al., "The ReaxFF Reactive Force-Field: Development, Applications and Future Directions", *npj Computational Materials*, vol. 2, no. 1, p. 15011, 2016. DOI: 10.1038/npjcompumats.2015.11.

[31] J. Tersoff, "New Empirical Approach for the Structure and Energy of Covalent Systems", *Physical review B*, vol. 37, no. 12, p. 6991, 1988. DOI: 10.1103/PhysRevB.37.6991.

[32] M. I. Baskes, "Modified Embedded-Atom Potentials for Cubic Materials and Impurities", *Physical review B*, vol. 46, no. 5, p. 2727, 1992. DOI: 10.1103/PhysRevB.46.2727.

[33] F. H. Stillinger and T. A. Weber, "Computer Simulation of Local Order in Condensed Phases of Silicon", *Physical review B*, vol. 31, no. 8, p. 5262, 1985. DOI: 10.1103/PhysRevB.31.5262.

[34] L. Verlet, "Computer" experiments" on classical fluids. i. thermodynamical properties of lennard-jones molecules", *Physical review*, vol. 159, no. 1, p. 98, 1967. DOI: 10.1103/PhysRev.159.98.

[35] W. G. Hoover, *Computational Statistical Mechanics*. Elsevier, 2012.

[36] S. Nosé, "A Unified Formulation of the Constant Temperature Molecular Dynamics Methods", *The Journal of chemical physics*, vol. 81, no. 1, pp. 511–519, 1984. DOI: 10.1063/1.447334.

[37] W. G. Hoover, "Canonical Dynamics: Equilibrium Phase-Space Distributions", *Physical review A*, vol. 31, no. 3, p. 1695, 1985. DOI: 10.1103/PhysRevA.31.1695.

[38] Q. Ke, X. Gong, S. Liao, C. Duan, and L. Li, "Effects of Thermostats/Barostats on Physical Properties of Liquids by Molecular Dynamics Simulations", *Journal of Molecular Liquids*, vol. 365, p. 120 116, 2022. DOI: 10.1016/j.molliq.2022.120116.

[39] G. J. Martyna, D. J. Tobias, and M. L. Klein, "Constant Pressure Molecular Dynamics Algorithms", *The Journal of Chemical Physics*, vol. 101, no. 4177, pp. 10–1063, 1994. DOI: 10.1063/1.467468.

[40] W. Shinoda, M. Shiga, and M. Mikami, "Rapid Estimation of Elastic Constants by Molecular Dynamics Simulation Under Constant Stress", *Physical Review B*, vol. 69, no. 13, p. 134 103, 2004. DOI: 10.1103/PhysRevB.69.134103.

[41] A. P. Thompson et al., "LAMMPS-A Flexible Simulation Tool for Particle-Based Materials Modeling at the Atomic, Meso, and Continuum Scales", *Computer physics communications*, vol. 271, p. 108 171, 2022. DOI: 10.1016/j.cpc.2021.108171.

[42] A. V. Shapeev, "Moment Tensor Potentials: A Class of Systematically Improvable Interatomic Potentials", *Multiscale Modeling & Simulation*, vol. 14, no. 3, pp. 1153–1173, 2016. DOI: 10.1137/15M1054183.

[43] A. P. Bartók, M. C. Payne, R. Kondor, and G. Csányi, "Gaussian Approximation Potentials: The Accuracy of Quantum Mechanics, Without the Electrons", *Physical review letters*, vol. 104, no. 13, p. 136 403, 2010. DOI: 10.1103/PhysRevLett.104.136403.

[44] H. Wang, L. Zhang, J. Han, et al., "DeePMD-kit: A Deep Learning Package for Many-Body Potential Energy Representation and Molecular Dynamics", *Computer Physics Communications*, vol. 228, pp. 178–184, 2018. DOI: 10.1016/j.cpc.2018.03.016.

[45] J. Zeng et al., "https://doi.org/10.1063/5.0155600", *The Journal of Chemical Physics*, vol. 159, no. 5, 2023. DOI: 10.1063/5.0155600.

[46] J. Zeng et al., "DeePMD-kit v3: A Multiple-Backend Framework for Machine Learning Potentials", *Journal of chemical theory and computation*, vol. 21, no. 9, pp. 4375–4385, 2025. DOI: 10.1021/acs.jctc.5c00340.

[47] I. Batatia et al., "A Foundation Model for Atomistic Materials Chemistry", *The Journal of chemical physics*, vol. 163, no. 18, 2025. DOI: 10.1063/5.0297006.

[48] J. Behler and M. Parrinello, "Generalized Neural-Network Representation of High-Dimensional Potential-Energy Surfaces", *Physical review letters*, vol. 98, no. 14, p. 146 401, 2007. DOI: 10.1103/PhysRevLett.98.146401.

[49] G. Wang, C. Wang, X. Zhang, Z. Li, J. Zhou, and Z. Sun, "Machine Learning Interatomic Potential: Bridge the Gap Between Small-Scale Models and Realistic Device-Scale Simulations", *Iscience*, vol. 27, no. 5, 2024. DOI: 10.1016/j.isci.2024.109673.

[50] Y. Zuo et al., "Performance and Cost Assessment of Machine Learning Interatomic Potentials", *The Journal of Physical Chemistry A*, vol. 124, no. 4, pp. 731–745, 2020. DOI: 10.1021/acs.jpca.9b08723.

[51] D. Zhang et al., "DPA-2: A Large Atomic Model as a Multi-Task Learner", *npj computational materials*, vol. 10, no. 1, p. 293, 2024. DOI: 10.1038/s41524-024-01493-2.

[52] Y. Zhang, H. Wang, W. Chen, J. Zeng, L. Zhang, H. Wang, et al., "DP-GEN: A Concurrent Learning Platform for the Generation of Reliable Deep Learning Based Potential Energy Models", *Computer Physics Communications*, vol. 253, p. 107 206, 2020. DOI: 10.1016/j.cpc.2020.107206.

[53] H. Beck, P. Simko, L. L. Schaaf, O. Marsalek, and C. Schran, "Multi-Head Committees Enable Direct Uncertainty Prediction for Atomistic Foundation Models", *The Journal of Chemical Physics*, vol. 163, no. 23, 2025. DOI: 10.1063/5.0302097.

[54] M. A. Khan, A. D'Souza, and V. Choyal, "Active Learning Strategies for Efficient Machine-Learned Interatomic Potentials Across Diverse Material Systems", *arXiv*, 2026. DOI: 10.48550/arXiv.2601.06916.

[55] M. Holzenkamp, D. Lyu, U. Kleinekathöfer, and P. Zaspel, "Evaluation of Uncertainty Estimations for Gaussian Process Regression Based Machine Learning Interatomic Potentials", *Machine Learning: Science and Technology*, vol. 6, no. 4, p. 045 019, 2025. DOI: 10.1088/2632-2153/ae09ef.

[56] I. S. Novikov, K. Gubaev, E. V. Podryabinkin, and A. V. Shapeev, "The MLIP Package: Moment Tensor Potentials with MPI and Active Learning", *Machine Learning: Science and Technology*, vol. 2, no. 2, p. 025 002, 2021. DOI: 10.1088/2632-2153/abc9fe.

[57] A. P. Bartók, R. Kondor, and G. Csányi, "On Representing Chemical Environments", *Physical Review B—Condensed Matter and Materials Physics*, vol. 87, no. 18, p. 184 115, 2013. DOI: 10.1103/PhysRevB.87.184115.

[58] V. L. Deringer and G. Csányi, "Machine Learning Based Interatomic Potential for Amorphous Carbon", *Physical Review B*, vol. 95, no. 9, p. 094 203, 2017. DOI: 10.1103/PhysRevB.95.094203.

[59] S. Klawohn, J. P. Darby, J. R. Kermode, G. Csányi, M. A. Caro, and A. P. Bartók, "Gaussian Approximation Potentials: Theory, Software Implementation and Application Examples", *The Journal of Chemical Physics*, vol. 159, no. 17, 2023. DOI: 10.1063/5.0160898.

[60] S. Klawohn, J. R. Kermode, and A. P. Bartók, "Massively Parallel Fitting of Gaussian Approximation Potentials", *Machine Learning: Science and Technology*, vol. 4, no. 1, p. 015 020, 2023. DOI: 10.1088/2632-2153/aca743.

[61] M. A. Caro, "Optimizing Many-Body Atomic Descriptors for Enhanced Computational Performance of Machine Learning Based Interatomic Potentials", *Physical Review B*, vol. 100, no. 2, p. 024 112, 2019. DOI: 10.1103/PhysRevB.100.024112.

[62] G. Csányi et al., "Expressive Programming for Computational Physics in Fortran 95+", *IoP Comput. Phys. Newsletter*, Spring 2007, 2007, https://www.southampton.ac.uk/~fangohr/randomnotes/iop_cpg_newsletter/2007_1.pdf, accessed 2026-03-27.

[63] D. Zhang et al., "A Graph Neural Network for the Era of Large Atomistic Models", *arXiv*, 2025. DOI: 10.48550/arXiv.2506.01686.

[64] B. Deng et al., "CHGNet as a Pretrained Universal Neural Network Potential for Charge-Informed Atomistic Modelling", *Nature Machine Intelligence*, vol. 5, no. 9, pp. 1031–1041, 2023. DOI: 10.1038/s42256-023-00716-3.

[65] A. Peng et al., "LAMBench: A Benchmark for Large Atomistic Models", *npj Computational Materials*, 2026. DOI: 10.1038/s41524-025-01929-3.

[66] VASP Wiki, *Phonons: Theory*, https://www.vasp.at/wiki/Phonons:_Theory, Accessed: 2026-03-24.

[67] A. Togo, L. Chaput, T. Tadano, and I. Tanaka, "Implementation strategies in phonopy and phono3py", *Journal of Physics: Condensed Matter*, vol. 35, no. 35, p. 353 001, 2023. DOI: 10.1088/1361-648X/acd831.

[68] A. Togo, "First-principles phonon calculations with phonopy and phono3py", *Journal of the Physical Society of Japan*, vol. 92, no. 1, p. 012 001, 2023. DOI: 10.7566/JPSJ.92.012001.

[69] A. Togo, K. Shinohara, and I. Tanaka, "Spglib: A Software Library for Crystal Symmetry Search", *Science and Technology of Advanced Materials: Methods*, vol. 4, no. 1, p. 2 384 822, 2024. DOI: 10.1080/27660400.2024.2384822.

[70] G. Makov and M. C. Payne, "Periodic Boundary Conditions in Ab Initio Calculations", *Physical Review B*, vol. 51, no. 7, p. 4014, 1995. DOI: 10.1103/PhysRevB.51.4014.

[71] C. Freysoldt, J. Neugebauer, and C. G. Van de Walle, "Fully Ab Initio Finite-Size Corrections for Charged-Defect Supercell Calculations", *Physical review letters*, vol. 102, no. 1, p. 016 402, 2009. DOI: 10.1103/PhysRevLett.102.016402.

[72] A. A. Gray-Weale, R. H. Henchman, R. G. Gilbert, M. L. Greenfield, and D. N. Theodorou, "Transition-state theory model for the diffusion coefficients of small penetrants in glassy polymers", *Macromolecules*, vol. 30, no. 23, pp. 7296–7306, 1997. DOI: 10.1021/ma970349f.

[73] G. Henkelman and H. Jónsson, "A Dimer Method for Finding Saddle Points on High Dimensional Potential Surfaces Using Only First Derivatives", *The Journal of chemical physics*, vol. 111, no. 15, pp. 7010–7022, 1999. DOI: 10.1063/1.480097.

[74] H. Jónsson, G. Mills, and K. W. Jacobsen, "Nudged Elastic Band Method for Finding Minimum Energy Paths of Transitions", in *Classical and quantum dynamics in condensed phase simulations*, World Scientific, 1998, pp. 385–404. DOI: 10.1142/9789812839664_0016.

[75] G. Henkelman, B. P. Uberuaga, and H. Jónsson, "A Climbing Image Nudged Elastic Band Method for Finding Saddle Points and Minimum Energy Paths", *The Journal of chemical physics*, vol. 113, no. 22, pp. 9901–9904, 2000. DOI: 10.1063/1.1329672.

[76] A. Hjorth Larsen et al., "The Atomic Simulation Environment—A Python Library for Working with Atoms", *Journal of Physics: Condensed Matter*, vol. 29, no. 27, p. 273 002, 2017. DOI: 10.1088/1361-648X/aa680e.

[77] M. Ishimaru, I.-T. Bae, Y. Hirotsu, S. Matsumura, and K. E. Sickafus, "10.1103/PhysRevLett.89.055502", *Physical review letters*, vol. 89, no. 5, p. 055 502, 2002. DOI: 10.1103/PhysRevLett.89.055502.

[78] N. Matsushima and J. Yamauchi, "First-Principles X-Ray Photoelectron Spectroscopy Binding Energy Shift Calculation for Boron and Aluminum Defects in 3C-Silicon Carbide", *Japanese journal of applied physics*, vol. 58, no. 3, p. 031 001, 2019. DOI: 10.7567/1347-4065/aafc52.

[79] I. Dabo, A. Ferretti, N. Poilvert, Y. Li, N. Marzari, and M. Cococcioni, "Koopmans' condition for density-functional theory", *Physical Review B—Condensed Matter and Materials Physics*, vol. 82, no. 11, p. 115 121, 2010. DOI: 10.1103/PhysRevB.82.115121.

[80] D. O. Demchenko and M. A. Reshchikov, "Koopmans' Tuning of HSE Hybrid Density Functional for Calculations of Defects in Semiconductors: A Case Study of Carbon Acceptor in GaN", *Journal of Applied Physics*, vol. 127, no. 15, 2020. DOI: 10.1063/1.5140661.

[81] A. R. Elmaslmane, M. B. Watkins, and K. P. McKenna, "First-Principles Modeling of Polaron Formation in TiO2 Polymorphs", *Journal of chemical theory and computation*, vol. 14, no. 7, pp. 3740–3751, 2018. DOI: 10.1021/acs.jctc.8b00199.

[82] G. Miceli, W. Chen, I. Reshetnyak, and A. Pasquarello, "Nonempirical Hybrid Functionals for Band Gaps and Polaronic Distortions in Solids", *Physical Review B*, vol. 97, no. 12, p. 121 112, 2018. DOI: 10.1103/PhysRevB.97.121112.

[83] Y. Huang, Y. Qian, Y. Zhang, D. Yang, and X. Pi, "Kick-Out Diffusion of Al in 4H-SiC: An Ab Initio Study", *Journal of Applied Physics*, vol. 132, no. 1, 2022. DOI: 10.1063/5.0096577.

[84] R. Rurali, "Theoretical Studies of Defects in Silicon Carbide", http://www.tdx.cat/TDX-0621104-193123, Accessed: 2026-03-27, Ph.D. dissertation, Universitat Autònoma de Barcelona, 2004.

[85] V. L. Deringer et al., "Realistic Atomistic Structure of Amorphous Silicon from Machine-Learning-Driven Molecular Dynamics", *The journal of physical chemistry letters*, vol. 9, no. 11, pp. 2879–2885, 2018. DOI: 10.1021/acs.jpclett.8b00902.

[86] J. Liu et al., "Machine-Learning-Based Interatomic Potentials for Group IIB to VIA Semiconductors: Toward a Universal Model", *Journal of Chemical Theory and Computation*, vol. 20, no. 13, pp. 5717–5731, 2024. DOI: 10.1021/acs.jctc.3c01320.

[87] The GPyOpt Authors, *GPyOpt: A bayesian optimization framework in python*, http://github.com/SheffieldML/GPyOpt, Accessed: 2026-03-27, 2016.

[88] M. Schreiner, A. Bhowmik, T. Vegge, J. Busk, and O. Winther, "Transition1x-A Dataset for Building Generalizable Reactive Machine Learning Potentials", *Scientific Data*, vol. 9, no. 1, p. 779, 2022. DOI: 10.1038/s41597-022-01870-w.

[89] J. Pezoldt and V. Cimalla, "Imprinting the Polytype Structure of Silicon Carbide by Rapid Thermal Processing", *Crystals*, vol. 10, no. 6, p. 523, 2020. DOI: 10.3390/cryst10060523.

[90] S. Leclerc, M. F. Beaufort, J. F. Barbot, and A. Declémy, "Strain and Amorphization Under Light-Ion Implantation in SiC", *Europhysics Letters*, vol. 98, no. 4, p. 46 001, 2012. DOI: 10.1209/0295-5075/98/46001.

[91] F. Giustino, *Materials Modelling Using Density Functional Theory: Properties and Predictions*. Oxford University Press, 2014.

[92] A. Jain et al., "Commentary: The Materials Project: A Materials Genome Approach to Accelerating Materials Innovation", *APL materials*, vol. 1, no. 1, 2013. DOI: 10.1063/1.4812323.

[93] A. Zaccone, "Https://doi.org/10.1063/5.0304896", *Journal of Applied Physics*, vol. 138, no. 22, 2025. DOI: 10.1063/5.0304896.

[94] Nordlund, Kai and Ghaly, Mai and Averback, RS and Caturla, María and de La Rubia, T Diaz and Tarus, Jura, "10.1103/physrevb.57.7556", *Physical Review B*, vol. 57, no. 13, p. 7556, 1998. DOI: 10.1103/PhysRevB.57.7556.

[95] R. Devanathan, F. Gao, and W. J. Weber, "Atomistic Modeling of Amorphous Silicon Carbide Using a Bond-Order Potential", *Nuclear Instruments and Methods in Physics Research Section B: Beam Interactions with Materials and Atoms*, vol. 255, no. 1, pp. 130–135, 2007. DOI: 10.1016/j.nimb.2006.11.045.

[96] X. Yan, P. Li, L. Kang, S.-H. Wei, and B. Huang, "First-Principles Study of Electronic and Diffusion Properties of Intrinsic Defects in 4H-SiC", *Journal of Applied Physics*, vol. 127, no. 8, 2020. DOI: 10.1063/1.5140692.

[97] J. C. Bridgeman and C. T. Chubb, "Hand-Waving and Interpretive Dance: An Introductory Course on Tensor Networks", *Journal of physics A: Mathematical and theoretical*, vol. 50, no. 22, p. 223 001, 2017. DOI: 10.1088/1751-8121/aa6dc3.